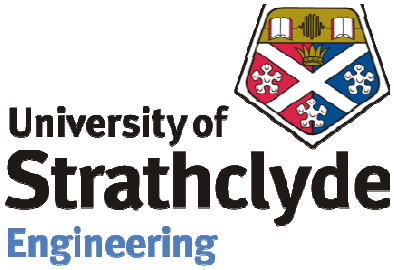

Department of Mechanical Engineering

Evaluating the Performance of Commercially Available Computational codes for Determining the Aerodynamic Characteristics of Wind Turbine Airfoils

Author: Andrew William Kay

Supervisor: Dr Andrew Grant

A thesis submitted in partial fulfilment for the requirement of degree in Master of Science in Renewable Energy Systems and the Environment

2010

Copyright Declaration

Signed: Andrew Kay Date: 09/09/10

Acknowledgements

A special thank you must go to Tom McCombes, who took the time out of his busy schedule as a research assistant at the University of Strathclyde to guide me through this project and offer his vast expertise on the field wind turbine aerodynamics. Special thanks must also go to my supervisor, Dr Andrew Grant who provided me with insightful advice on how to approach the project as a whole.

Abstract

Due to a growing awareness of the environmental impact of burning fossil fuels, combined with an increasing concern over the finiteness of the world's reserves of coal, oil and gas, governments around the world have been hard pressed to take measures to adopt more green technologies for power generation. The most significant advancements have been made in the field of wind energy, with the wind turbine now the fastest growing technology for renewable power generation in the world. Despite this rapid development, the wind industry must still strive to ensure that any device designed for commercial use is reliable and able to perform to a level capable of satisfying its economic projections. In the design of a commercially viable wind turbine, it is imperative that an accurate assessment is made of the aerodynamic characteristics of the airfoils employed on the blades. Errors made may result in wrong estimates of the turbines performance and economic projections. If these characteristics cannot be determined by experimental tests, a designer will have to rely on computational methods.

This thesis evaluates the performance of three commercially available computational codes for determining the aerodynamic coefficients of airfoils. Two airfoil analysis and design codes and a CFD solver are applied to evaluate their accuracy and ease of use at reproducing the coefficients of two wind turbine airfoils, previously determined by experiment. The use of CFD was found to be more labour intensive than both the airfoil analysis and design codes; however, it was shown to be more accurate and flexible for determining the behaviour of complex turbulent flows. Three turbulence models were used in the CFD solver to analyse their accuracy for modelling the flow over airfoils. It was shown that a turbulence model must be equipped to model the behaviour of adverse pressure gradient flows in order to accurately model the forces experienced by a wind turbine airfoil. The SST k-ω and Spalart-Allmaras models proved to satisfy this criterion the best out of three analysed models. The accuracy of CFD was also shown to be largely dependent on the standard of the mesh used. The mesh must be able to map the orientation of the wake region, which is often modified for wind turbine airfoils in comparison to those used for other

aerospace applications. A methodology on how to improve the standard of a mesh used to model the flow around a wind turbine airfoil is also proposed.

List of contents

List of Figures

List of Tables

Chapter 1

Introduction to Wind Power

1.1 - History and Growth

The conversion of wind energy into useful energy has laid the foundations for one of the most significant technological developments of the late 20th century. Wind turbines - developed to harness wind power and use it for generating electricity – are the technology behind one of the fastest growing industries for power generation, and are now a common sight within the rural and urban areas of countries all over the world.

Early use of wind turbines for electricity generation dates back to the end of the 19th century. For a number of decades, the development of these devices went through a conceptual stage, producing a number of designs which have had a large influence on the machine's we more commonly see operating today. However, due to the invention of the steam engine and a period of large industrial expansion, industrialised countries around the world chose to generate their electricity via the burning of cheap and widely available fossil fuels [1]. The emergence of modern wind turbines and the wind power industry as we know it today can be attributed to a number of distinct factors. A growing awareness of the environmental impact of burning fossil fuels for conventional power generation, combined with an increasing concern over the finiteness of the worlds reserves of coal, oil and gas started a global campaign to seek alternative methods for extracting energy [1]. Burning fossil fuels increases the concentration of greenhouse gasses in the earth's atmosphere which can over-heat the earth's surface and cause global warming. Wind as an energy source is infinite and occurs in some places with a high enough density and regularity for power generation [1]. Moreover, the conversion of wind power into electricity has an almost net zero effect on the earth's concentration of greenhouse gasses. The clean image of wind power and its vast potential for energy extraction has been a driving factor behind the recent boom in the development of wind turbines.

One other vital influence in the emergence of wind power as a source of energy has come from government support and investment; without which the cost of energy from wind turbines would not be competitive with conventional sources [1]. Investment has come in the form of research, development and testing to advance turbine technology and improve its energy yield capabilities. Support has been provided by incentive schemes to quicken the deployment of the new technology and regulatory reform to ease the development process for erecting wind turbines and connecting them to the grid [1].

Another closely related factor has been the recent political drive by governments to reduce the reliance on conventional forms of power generation and adopt more green technologies, like wind and other renewable sources of energy. This has largely been in response to a number of international agreements between countries to limit emissions of greenhouse gasses. One such agreement is the Kyoto Protocol, which is an addition to the treaty drawn up by the United Nations Framework Convention on Climate Change (UNFCCC). This agreement sets binding targets for 37 industrialised countries and the European community for reducing greenhouse gas emissions [2]. In total, these targets amount to an average of 5% against 1990 levels over the five year period between 2008 and 2012 [2]. One way governments are addressing this agreement is by investing in renewable technologies for electricity generation. In 2007 the European Council set a target to meet 20% of the EU's energy demand with renewable sources by 2020 [2]. In terms of renewable sources, wind energy is the most mature. Wind turbine technology is relatively well understood and well developed and as a result is thought to be a reliable substitute or addition to a countries conventional power supply. In addition to the issue of environmental impact, governments are also turning to green energy systems as a sense of urgency for securing their energy supply. For example, the UK has recently become a net importer of gas, where it is estimated that by 2020, the UK will be 80% dependant on imported gas [3]. In order to become more self sufficient and ensure a secure supply of energy, the UK has placed a large emphasis on adopting alternative sources of energy for generating electricity. With Europe's largest wind resource, it is unsurprising that wind power has made such a significant contribution to current efforts within the UK to enhance its sustainability.

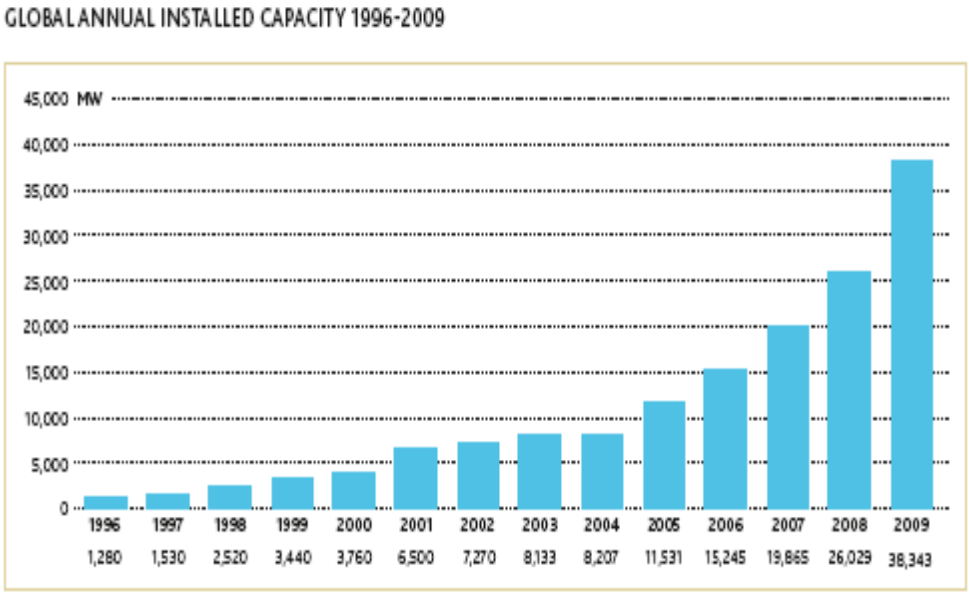

Figure 1 – Global annual installed capacity of wind power (MW) -1996-2009 [43]

Wind power has had many positive influencing factors that have turned it into the fastest growing technology for renewable power generation in the world. Figure [1] illustrates the growth of the industry in installed capacity since 1996. It can be seen that even during a period of global economic crisis between 2008 and 2009; the industry experienced its most rapid expansion over the past 13 year period. This is a testament to the strength of the industry and the advancements that have been made in wind turbine technology over recent years.

1.2 - Power in the Wind

In detail, the operation of a wind turbine is complicated and to understand it, requires a deep appreciation of the underlying flow physics behind the function of such a device. However, the basic principals are fairly easy to understand and require little explanation. In short, when wind blows through the rotor area of a turbine it causes the blades to rotate, converting the kinetic energy of the wind into rotational energy of the turbine [4]. As kinetic energy is being extracted from the wind, the air flowing through the disk area experiences a decrease in velocity [4]. The resulting change in momentum that occurs within the air exerts an axial thrust on the rotor which turns the blades and hence, adds a rotational component to the

winds velocity [5]. The rotational energy can be exploited to produce “useful work” [4] which commonly comes in the form of electric power from a generator connected to the shaft of the turbine [4]. Immediately this tells us that the extent of electrical power produced will be largely dependent on the magnitude of the power and hence, kinetic energy stored in the wind. If we consider the kinetic energy of wind blowing at a velocity, $V\infty$ flowing through a rotational disk area, A with the disk area normal to the oncoming flow then, the kinetic energy per unit time stored in the wind flowing through the disk area can be approximated by Equation (1) [4]:

$$\frac{KE}{dt} = \frac{1}{2}\dot{m}|V\infty|^2 \text{ – Equation (1)}$$

With $\dot{m} = \rho AV\infty$ equal to the mass flow rate through the disk area, the power in the wind can be approximated by Equation (2) [4]:

$$P = \frac{1}{2}\rho A|V\infty|^3 - \text{Equation (2)}$$

Therefore, it is clear to see that the power available in the wind is a function of air density, disk area and wind velocity cubed. One way to maximise the extraction of this power would be to increase the diameter of the turbine rotor, hence increasing the disk area. This has been a large characteristic of wind turbine development over the last 20 years. Another method would be to position the turbine in an area where the wind speeds are well known and of a magnitude sufficient enough for large scale power generation. This inherently requires a good understanding of the wind resource available at the desired location.

The ability of a wind turbine to capture kinetic energy in the wind and produce useful work and hence, its efficiency, is limited by what is known as the Betz limit. According to Betz law, no turbine can capture more than 59.3 percent of the kinetic stored energy in the wind [1]. In reality, the efficiency of the conversion process is significantly lower than this. The actual power produced by a wind turbine must also take into account several other factors including the fluid mechanics of the flow passing through the rotor and the aerodynamics and efficiency of the rotor/generator combination [1]. To understand this requires a deeper understanding of the underlying flow physics behind the three dimensional flow field associated with a modern wind turbine.

1.3 - Device Types

Wind turbines are distinguished by the orientation of the rotor shaft axis with respect to the ground, where two common types exist; Horizontal-Axis Wind Turbines (HAWT) and Vertical-Axis Wind Turbines (VAWT). An example of a HAWT, with its shaft parallel to the ground is shown in Figure [2].

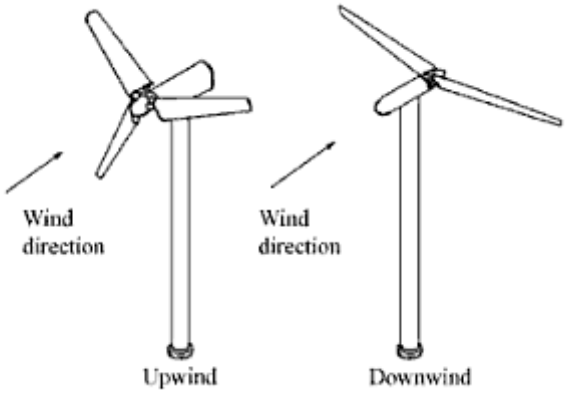

Figure 2 – Upwind and Downwind rotor definition [1]

This is the most common type of wind turbine which typically has three blades and is mounted on a tower which can either be downwind or upwind of the rotor. With a downwind tower the turbine will naturally try to align its axis with the direction of the wind, although these induce the effects of tower shadow which can generate unsteady blade air loads on the turbine and can impact its structural integrity and lifetime. Modern three bladed HAWT have a generating capacity of between 1.5 and 5 MW and are currently being employed in both onshore and offshore wind farms at various locations around the world [1]. Taking into account all factors and assuming the best device currently available, the efficiency of a HAWT is not likely to exceed 45% [1].

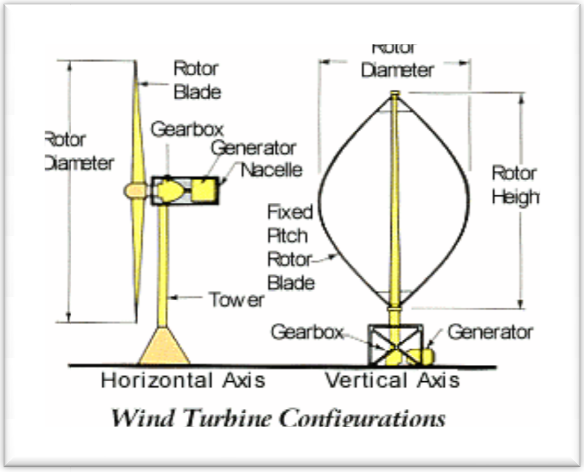

Figure 3 – HAWT and VAWT definition [20]

Figure [3] shows the differences between this type of turbine and a VAWT. VAWT are less common and less efficient than HAWT; their main advantage is that they can generate power independent of the wind direction and do not require a form of yaw correction [4]. The cyclic variations in angle of attack, caused when a turbine is yawed to oncoming flow, can have an adverse impact on a turbines structural integrity and overall lifetime. Additionally, these devices do not require as much wind to generate power and hence, they can be positioned closer to the ground; this makes them more desirable for urban applications, such as deployment on tall structures within cities. VAWT's are typically up to 30% efficient [6].

1.4 - Design, Development and Implementation

The design, development and implementation of a wind turbine, or wind farm, built to exploit the power contained in the wind and generate electricity, integrates many disciplines of engineering, including: aerodynamics, mechanical, materials, control, electrical and manufacturing engineering [5]. Each of these divisions plays an important role in comprising the various operational elements of a wind turbine, its foundations and its connection to the main grid, which collectively is termed a Wind Energy Conversion System (WECS) [5]. Each must work together as efficiently as possible in a very complex environment. The core objective of each design being: to maximise the energy yield and lifetime of the turbine whilst keeping the overall costs as low as possible. The design of a wind turbine must also be tailored in order to adapt to the specific meteorological and topographical characteristics of

the chosen site of installation [5]. These considerations are fundamental to the wind power industry in order to make it competitive with conventional forms of electricity, such as coal and gas, in terms of generation, reliability and cost.

Key considerations that must be made during the lifetime of a wind turbines development and operation fall under the three distinct categories of: technical, economic and environmental. However, these three categories are often highly interchangeable, especially technical and economic, where decisions made regarding one category are usually made to reflect the best interest of another.

1.5 - Modelling

Perhaps the most important figure concerning wind energy companies is the Cost of Energy (COE) [5]. This gives an indication of how much it is costing a company to generate electricity by comparing the money invested into developing and maintaining a WECS with the revenue gained from its annual energy yield [5]. The more efficient and structurally sound the device is, the better and longer it will operate and the greater the return will be. In order to keep the COE as low as possible, it is necessary to maximise the performance and lifetime of a device, whilst minimising the cost of maintenance. A correct prediction of the COE is also important when drawing up economic predictions for an individual device or farm. Energy companies will be wagering a level risk on the economic return of a WECS, and may invest some of that expected profit in other projects. An underestimated COE may result in a loss of expected finances and may delay the completion of other projects due to a lack of company funds.

To help maximise performance, determine expected loads and maintenance schedules, and estimate correct economic projections, a design team will incorporate the use of predictive modelling tools [5]. These will usually take the form of an aerodynamic, structural and cost model, working interchangeably to determine the lowest possible COE. Figure [4] displays a flow chart of how these models interchange to achieve this goal.

From looking at the chart it is clear how important the aerodynamics model is in determining the correct COE [5]. The model acts to predict the aerodynamic forces on the blades for a

specific rotor geometry and hence, determine the aerodynamic performance and annual energy yield (AEP) at a given site. The aerodynamic loads also provide the inputs for the structural model. The structural model must determine the loads and stresses that the system will bear as a result of the aerodynamic loadings and hence, the requirements for the materials. These will provide the inputs for the cost model which will factor in the necessary cost of materials to withstand the structural loads and the manufacturing costs of assembling the WECS. The cost model will also consider the annual maintenance costs –

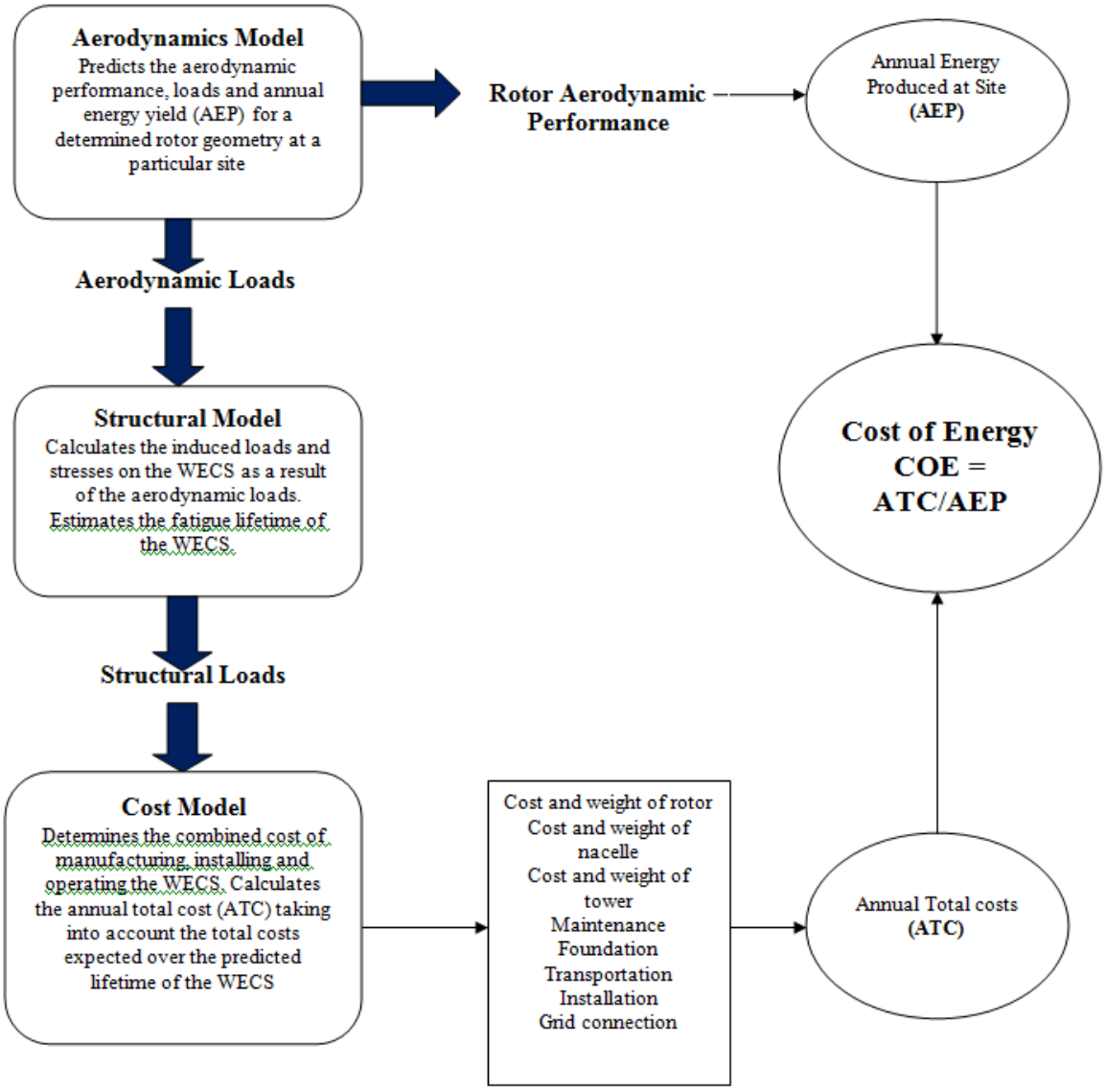

Figure 4 – Flow chart displaying the interaction of the three prediction models to determine the COE [5]

based on the schedules drawn up from the outputs of the structural model - and the cost of installation. Finally, after consideration of some other costs incurred over the lifetime of the turbine, the annual total cost (ATC) can be determined. Therefore, as illustrated in the chart, the aerodynamics model has provided both the inputs to the ATC and the AEP predictions, to determine the overall COE.

Chapter 2

Overview of Theses

This thesis concentrates on some of the issues associated with modelling the aerodynamics of airfoils employed on Horizontal Axis Wind Turbines. The main body of the report examines the performance of three computational tools used for reproducing the aerodynamic characteristics of two airfoils that have been previously defined by experiment.

The remainder of the thesis is organised as follows:

- In Chapter [3] some fundamental principles of aerodynamics are discussed including the different types of aerodynamic flows and how to solve an aerodynamics problem. This is followed by a description of airfoils, their aerodynamic properties and the various types of flow phenomena associated with them. A discussion of airfoils used for HAWT is also included. The chapter ends with a description of the methods used to predicted wind turbine performance and a discussion of the impact of unsteady effects on those predictions.

- In Chapter [4] some of the current issues associated with predicting the aerodynamics of HAWT are discussed. These include: the impact of unsteady effects, and the growing requirement for a means other than experiment for generating reliable airfoil characteristics.

- Chapter [5] sets out the aims of the thesis.

- In Chapter [6] the two airfoils chosen for this analysis are discussed followed by a description and analysis of the data gathered on them from experiment.

- Chapter [7] describes the computational methods adopted for this thesis.

- Chapter [8] details the approach adopted to satisfy the aims of this thesis. This is broken down into sections describing the methodology employed for each computational tool.

- Chapter [9] provides a full description and discussion of the results produced from this analysis.

- In chapter [10] the thesis is brought to a close by outlining the conclusion drawn from the experiences gained over the course of this project.

Chapter 3

Aerodynamics of Horizontal Axis Wind Turbines

Before discussing some of the current issues associated with modelling HAWT, it is essential to have some understanding behind the aerodynamics associated with such a device. The mean power and mean loads generated by a wind turbine are largely dependent on the aerodynamic performance of the rotor [1] and hence, an appreciation of the aerodynamic forces generated by the mean wind is of vital importance. The following section will first introduce some essential background behind aerodynamic flows and the mathematical equations used to describe them. It will then provide some insight into airfoils and their application to wind turbines, before ending with a review of the techniques used to predict wind turbine performance.

3.1 - Fundamental Concepts of Aerodynamics

To analyse any practical situation regarding aerodynamic flows, such as the flow through a wind turbine, requires an understanding of the basic concepts that characterise aerodynamic flows and the mathematical equations that govern them. In aerodynamics we usually refer to the study of airflow over a surface, which is a sub category of the field, fluid dynamics. Therefore, in the study of aerodynamics it is common to refer to the flow of air as the flow of a moving fluid with the properties of air at a given atmospheric state [8].

3.1.1 - Properties of Fluids and Types of Flow

A fluid particle of air, acting on a surface can be categorized as having four distinct variable properties: pressure, density, temperature and flow velocity [8]. These are all point properties which can vary from point to point in the flow [8]. When solving an aerodynamic problem mathematically, these properties are usually expressed in terms of a three-dimensional coordinate system. For example, in a Cartesian coordinate system, the velocity vector is expressed as: $V = u\boldsymbol{i} + v\boldsymbol{j} + w\boldsymbol{k}$. Another factor which can largely govern aerodynamic flows is friction [8]. Friction - often referred to as viscosity - can give rise to shear stresses which retard the flow near a surface, affecting the distribution of forces around a body; this will be discussed later in this section. The variation in and presence of these properties throughout a flow field gives rise to six distinct types of flow, which are summarised below in Table [1] [8]:

Flow Description	**Characteristics**
Steady	Flow field properties at any given point are invariant with time
Unsteady	Flow field properties at any given point change with time
Incompressible	Flow in which the density is constant
Compressible	Flow in which the density is varying
Inviscid	Flow in which the density is varying
Viscous	Flow which invokes friction

Table 1 – Various flow types and a description of their characteristics

Low speed flows over the blades of a wind turbine are almost entirely incompressible [1]. Depending on the region and regime, the flow can both be inviscid or viscous. For the majority of its operation, the flow through a wind turbine is steady; however, as a result of certain atmospheric and operational conditions, the flow can become unsteady [1].

3.1.2 - Solving an Aerodynamics Problem

Any aerodynamics problem can be solved by applying the following procedure [8]:

1) Determine a suitable model for the fluid
2) Apply the three fundamental physical principals of nature
    a. Mass is always conserved (continuity)
    b. Newton's second law: force = mass * acceleration
    c. Energy is always conserved
3) Obtain mathematical equations which describe the behaviour in terms of the flow properties and apply them to the problem

For step 1 there exist three models that are commonly used when solving aerodynamic problems: (1) The Finite Control Volume Approach, (2) The Infinitesimal Fluid Element Approach, and (3) The Molecular Approach [8]. Within the following equations model (1) is applied. The diagram below in Figure [5] illustrates this model.

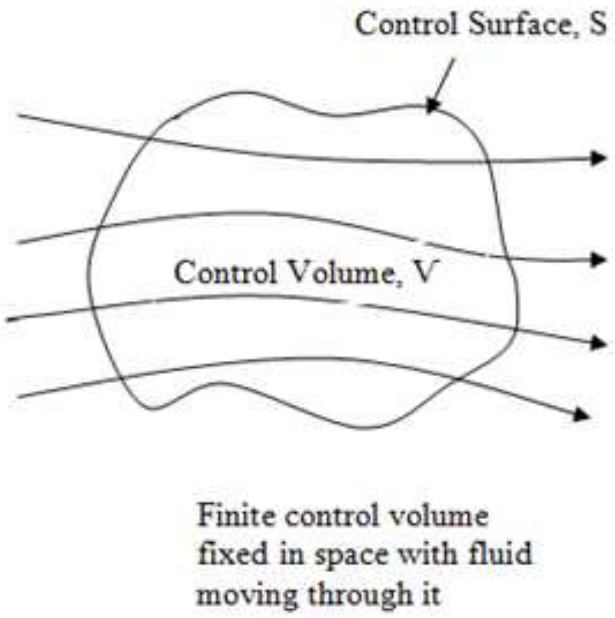

Figure 5 – Finite control volume Approach [8]

Considering the first physical principal of nature - that mass can neither be created nor destroyed – we can define the first equation that governs the motion of a fluid by applying this principal to a control volume fixed in space to give Equation (3):

$$\frac{\partial}{\partial t}\iiint_{\mathcal{V}} \rho d\mathcal{V} + \oiint_{S} \rho V.\mathrm{dS} = 0 - \text{Equations (3)}$$

This is known as the continuity equation and states that: the net mass flow out of the control volume through the surface, S is equal to the time rate of decrease of mass inside control volume, $\mathcal{V}$ [8]. This relates the flow field properties over a finite region of space [8]. By applying divergence theorem to this equation we can also define a form of the continuity equation for a given point in the flow to give Equation (4) [8]:

$$\frac{\partial \rho}{\partial t} + \nabla.(\rho V) = 0 - \text{Equation (4)}$$

Expressing Newton's second law as: force equals the time rate of change of angular momentum [8], we can now define the second integral equation that governs the motion of a fluid by applying this principal to a fixed control volume over a region of space to give Equation (5) [8]:

$$\frac{\partial}{\partial t}\iiint_{\mathcal{V}} \rho V d\mathcal{V} + \oiint_{S} (\rho V.\mathrm{dS})\, V = -\oiint_{S} p dS + \iiint_{\mathcal{V}} \rho \mathbf{f} d\mathcal{V} + \mathbf{F}_{\text{viscous}} - \text{Equation (5)}$$

This is known as the momentum equation and states that: The forces exerted on a fluid as it flows through a control volume (body forces, e.g. gravity + surface forces, e.g. pressure, viscous stresses) are equal to the net flow of momentum out of the control volume, across the surface S, plus the time rate of change of momentum due to unsteady fluctuations of flow properties inside $\mathcal{V}$ [8]. In a similar fashion to the continuity equation, by applying the

gradient and divergence theorem, the momentum equation can be expressed as a partial differential equation, relating the flow field properties at a point in space [8]. Below in Equation (6) is the momentum equation for the x component of the velocity vector field:

$$\frac{\partial(\rho u)}{\partial t} + \nabla.(\rho u V) = -\frac{\partial p}{\partial x} + \rho f_x + (F_X)_{viscous} \quad \text{– Equation (6)}$$

In their integral form, these equations relate the flow field properties over a finite region of space for any unsteady, three dimensional, incompressible, viscous or inviscid flow [8]. Depending on the type of flow, simplifications to these equations can be made, e.g. for steady inviscid flow the time dependant and viscous terms would be removed. If a compressible flow was being analysed then the energy equation would need to be included. However, since wind turbine flows are largely incompressible, the continuity and momentum equations are sufficient enough.

In order to complete these equations for any type of flow, we need to express the viscous forces in terms of the appropriate flow-field properties; this requires a modification to the fluid-flow momentum equation. Claude-Louis Navier and George Gabriel Stokes provided the solution in 1822, by developing the full set of governing equations for fluid flow, including viscous terms, entitled the Navier-Stokes equations. A full description of the derivation of these equations is provided in reference [8].

These equations provided the basis for theoretically solving many aerodynamics problems. For example the momentum equation can be used to determine the lift and drag forces over a two-dimensional body, such as an airfoil employed on the blades of a wind turbine. Another method for determining these forces is through experiment, commonly done in wind tunnels. The final method for solving the governing equations is by numerical analysis. One numerical technique which has revolutionised the solution of aerodynamic problems is computational fluid dynamics (CFD). Until the advent of high-speed digital computers and CFD, many complex aerodynamic flow fields had not been solved theoretically [8]. This powerful tool has given rise to a whole new discipline within the broad study of

aerodynamics. The application of CFD to the 2D study of airfoils for wind turbines comprises a large majority of this report.

3.2 Airfoils and Associated Flow Characteristics

Wind Turbines use airfoils to extract energy from the wind and generate mechanical power [1]. If a cross section of a wind turbine blade was taken and viewed, the resulting shape would be that of an airfoil, as illustrated in Figure [6]. Different airfoil shapes are usually employed along the span of a blade to achieve a desired aerodynamic or structural purpose. When the wind blows over an airfoil it will generate a force system; this results in a mechanical torque at the rotor shaft causing the rotor to rotate. The main driving force behind this process is known as the lift force. The shaft then transfers the torque from the blades to the generator, producing electrical energy.

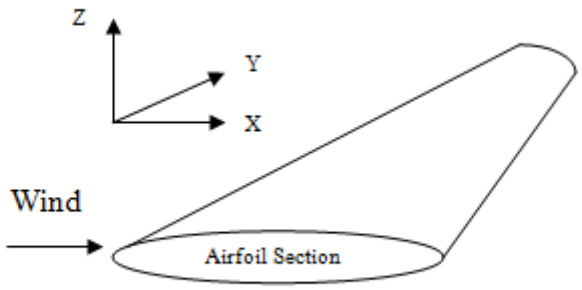

Figure 6 – Wind turbine blade displaying airfoil cross section

The origins of airfoils dates back to the early advent of successful power flight when during the period of 1912 – 1918, a research team spear headed by Ludwig Prandtl at Gottingen, Germany, illustrated that the aerodynamic consideration of wings requires an initial assessment of the cross section of a wing, termed an airfoil [8]. Airfoils were later adapted for use in other aerodynamic applications including helicopters and later, modern wind turbines. An introduction to some airfoil concepts and their associated aerodynamic characteristics will now follow.

3.2.1 Airfoil Nomenclature

Before looking at the force system on an airfoil, it is essential to introduce some basic terms describing the geometric properties of airfoils; these are clearly illustrated in Figure [7]. Of particular importance is the chord length, c, which is the precise distance between airfoils leading (LE) and trailing (TE) edge [8], and the thickness, t, which is the distance between the upper and lower surfaces, measured perpendicular to the chord line [8]. The most influential parameter on the airfoils force system is the angle of attack, α, defined as the angle between the relative wind vector and the chord line. Other parameters that can influence the forces on the airfoil are: the leading edge radius, the mean camber line, maximum thickness, the thickness distribution of the airfoil and the trailing edge angle [1].

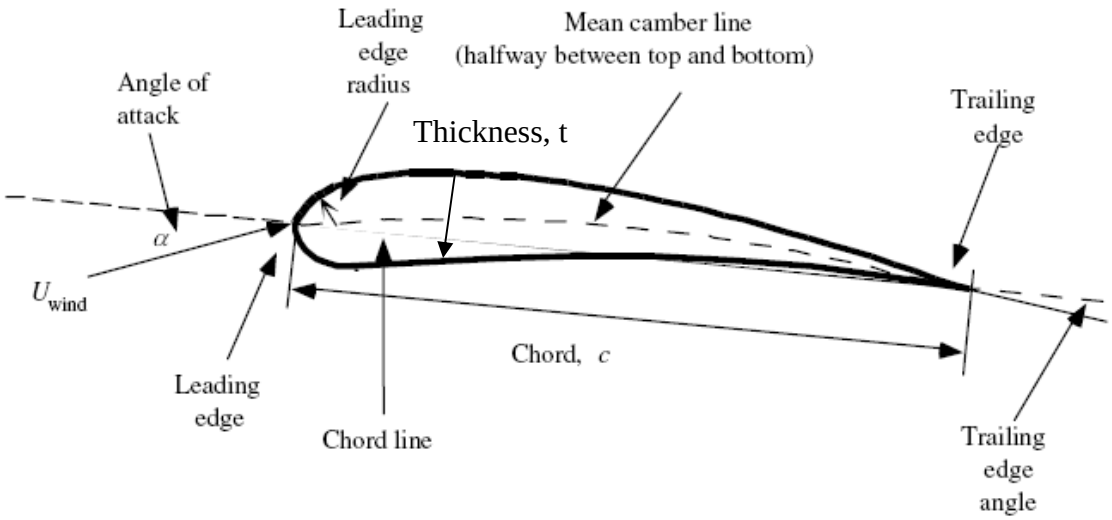

Figure 7 – Geometric properties of airfoils [1]

3.2.2 Aerodynamic Forces and Moments

As the oncoming wind flows over the airfoil surface, the airfoil will generate its own distribution of forces and moments, known as a force system. These aerodynamic forces and moments are due to only two primary sources (1) the pressure distribution over the body surface, and (2) the shear stress distribution over the body surface [8]. This is a fundamental

theory of fluid dynamics and states that “The only mechanism nature has for communicating a force to a body moving through a fluid are pressure and shear stress distributions on the body surface” [8]. By integrating these distributions over the surface of an airfoil the resulting aerodynamic force R and moment M is produced, as shown below in Figure [8].

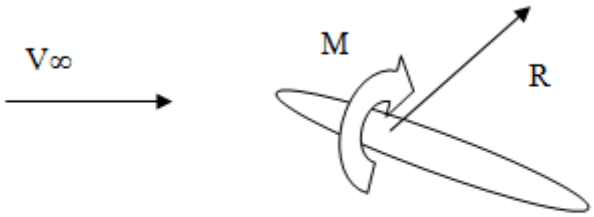

Figure 8 – Resultant aerodynamic force and moment on an airfoil

M is defined as the pitching moment which is taken about an axis perpendicular to the airfoil cross section [1]; this is usually placed at the quarter chord location where moments that tend to increase α (nose up) are positive, and moments that decrease α (nose down) are negative [8]. The pitching moment can be calculated by integrating the net moments acting on the airfoil from the leading to the trailing edge, taking the quarter chord as the reference axis [8]. An expression for M can therefore be determined in Equation (7) as [8]:

$$M = \int_{LE}^{TE} dM_{upper} + \int_{LE}^{TE} dM_{lower} \quad \text{– Equation (7)}$$

Resolving the resultant force into components gives the force system for an airfoil, shown below in Figure [9]. V_∞ is defined as the flow velocity far away from the airfoil and is known as the freestream velocity. L is defined as the lift force and is the component of R perpendicular to V_∞. D is defined as the drag force and is the component of R parallel to V_∞.

N is the normal force and is the component of R perpendicular to the chord, c, and finally, A is the axial force and is the component of R parallel to c.

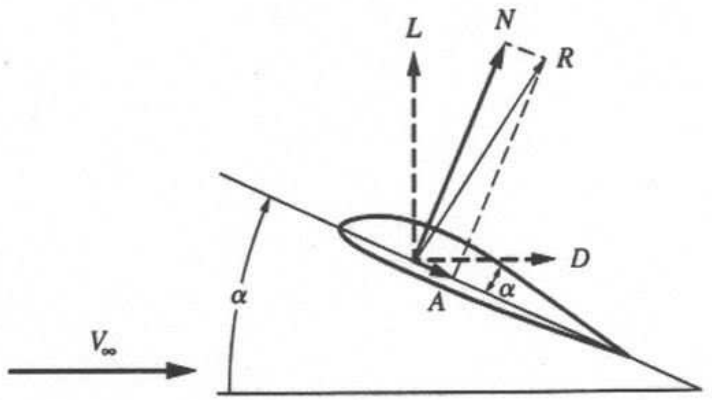

Figure 9 – Airfoil force system [1]

With the angle of attack previously defined as the angle between the chord line and V_∞, the following geometric relationships in Equations (8) and (9) can be drawn up for the force components of an airfoil [8]. The angle of attack (α) therefore determines how much of the normal and axial forces transfer into lift and how much into drag.

$$L = N\cos\alpha - A\sin\alpha \quad \text{– Equation (8)}$$

$$D = N\sin\alpha + A\cos\alpha \quad \text{– Equation (9)}$$

Flow over airfoils is usually designed so that the velocity increases over the upper "suction" side and decreases over the lower "pressure" side of the airfoil [1]. Pressure is inversely proportional to velocity therefore, when air flows over an airfoil a pressure differential is created where the pressure on the lower surface exceeds that of the upper surface, creating the lift force. This relationship was derived from Bernoulli's equation and forms the driving force for the mechanical power generated by wind turbines. The pressure distribution is the main contributor to the generation of lift where the shear stress distribution has a negligible effect [8]. The drag force is a consequence of both the viscous friction forces at the surface of the

airfoil (skin friction drag) and the unequal pressures of the airfoil surfaces facing towards and away from the oncoming flow (form drag) [1].

3.2.3 Aerodynamic Coefficients and Non-Dimensional Parameters

When analysing the aerodynamic forces and moments on a body, it is more common and convenient to express them as their dimensionless coefficients. These are determined by dividing the forces and moments by a dimensionless quantity called the freestream dynamic pressure, expressed in Equation (10) as [8]:

$$q = \frac{1}{2}\rho_\infty {V_\infty}^2 - \text{Equation 10}$$

The dimensionless force and moment coefficients are defined as follows in Equations (11-15), taking S as some reference area and l as a reference length [8].

$$CL = \frac{L}{q_\infty S}, \quad CD = \frac{D}{q_\infty S}, \quad CN = \frac{N}{q_\infty S}, \quad CA = \frac{A}{q_\infty S}, \quad CM = \frac{M}{q_\infty S l} - \text{Equations (11-15)}$$

When determining these coefficients for a complete three dimensional body capital letters are employed, e.g. CL, CD as in above [8]. However, when defining a two dimensional body such as an airfoil, lower case letters are used e.g. cl, cd and cm. In this instance, the reference area is taken as the airfoil chord, c = 1, and the forces measured are forces per unit span [1].

As it is important to know the pressure distribution around an airfoil for the purpose of determining the aerodynamic forces, a pressure coefficient can also be defined, expressed in Equation (16) as [8]:

$$C_p = \frac{P - P_\infty}{q_\infty} - \text{Equation (16)}$$

Where P is the static pressure at a location on the airfoil surface and P_∞ is the freestream pressure.

Another dimensionless parameter which is extremely useful in describing the flow conditions over an airfoil is the freestream Reynolds number expressed below in Equation (17):

$$Re = \frac{\rho_\infty V_\infty c}{\mu_\infty} \quad \text{–Equation (17)}$$

Where, ρ_∞ is the freestream density and μ_∞ is the dynamic viscosity of the fluid. The force and moment coefficients of an airfoil are a function of this important parameter, describing the ratio of the inertial forces to the viscous forces within the flow.

3.2.4 Airfoil Characteristics

The variation of the force and moment coefficients with angle of attack for an airfoil is commonly termed a polar. Typical polars for lift, drag and moment coefficients are displayed in Figure [10].

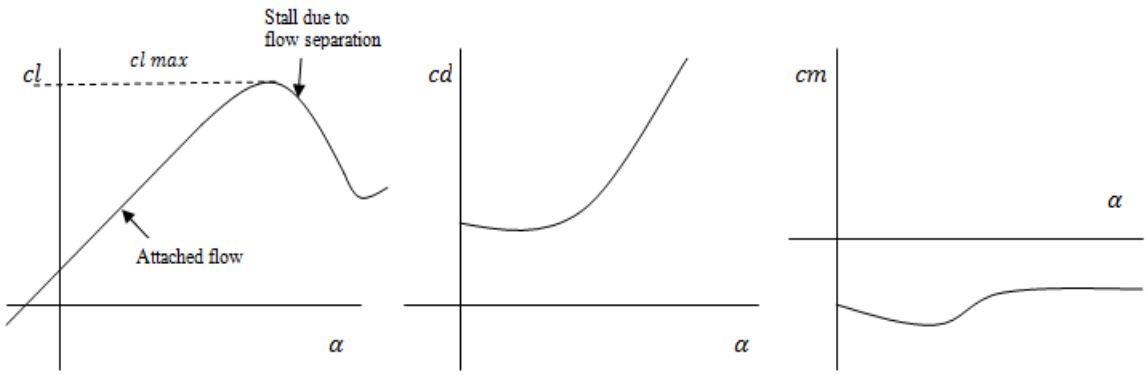

Figure 10 – Typical Lift, Drag and Moment polars

At low to moderate angles of attack, the variation in cl with α – denoted as the lift curve slope - is linear. Over this range of α, the drag remains low as the flow moves smoothly over the airfoil and remains attached over the majority of the surface [8]. At this point the flow can be described as inviscid which implies that viscous forces are small in comparison to inertial forces. As α increases to higher angles of attack, the flow begins to separate over the upper surface, creating a region of turbulent air above and behind the airfoil known as the wake. Within this region, flow reversal occurs where some of the flow begins to move in the opposite direction to the freestream. Now viscous forces in the flow are starting to have more of an impact on the force and moment coefficients, with the drag force beginning to rise, yet the lift continues to increase and the airfoil experiences a strong nose up pitching moment. The influence of viscous forces on flow separation will be described later in this section. Eventually, at some angle of attack, the increasing presence of flow separation causes a sudden decrease in lift and rapid increase in drag causing the airfoil to stall, after which the flow can be described as fully stalled [8]. The value of cl prior to stall is termed $cl\ max$. This value will be dependent on the Reynolds number of the flow, because it is heavily influenced by viscous forces [8]; remembering that the Reynolds number is a ratio between the strength of the inertia forces relative to the viscous forces in the flow [8]. Conversely, the lift curve slope will be less influenced Re as it is almost entirely inviscid. The moment coefficient will only become influenced by Re at high angles of attack; whilst the drag polar will be more sensitive to Re as it is influenced by both skin friction effects and flow separation [8]. Therefore, in order to fully recognise the aerodynamic response of an airfoil, it is essential to consider both a range of angles of attack (AoA) and Reynolds numbers.

3.2.5 Viscous Flow

The previous section illustrates how the drag on an airfoil and the lift at high angles of attack are largely influenced by the presence of viscous flows. Forces within viscous flows, namely frictional shear stresses, occur at any point within a flow field where there are velocity gradients across the streamlines [8]. These stresses are most influential on the flow where the velocity gradients are the most pronounced. For the case of an airfoil, the velocity gradients

are the highest within the thin region of the flow adjacent to the surface; here friction plays a commanding role. In contrast, the velocity gradients are low in the flow field away from the surface and frictional effects are less dominant. The thin region, close to the airfoil surface, governed by the presence of viscous flow is known as the boundary layer. This region is very small in comparison to the rest of the flow, yet its presence is the prime reason behind flow separation and the subsequent rapid changes in lift and drag witnessed during stall [8].

Viscous flow within a boundary layer can either be laminar or turbulent. When laminar, the fluid elements move smoothly along the streamlines over the upper and lower surface of an airfoil. However when turbulent, the fluid behaviour becomes more irregular as the streamlines break up and become more random in their nature [8]. The velocity distribution within a laminar boundary layer produces smaller shear stresses than those experienced within a turbulent one. As a result, laminar flow yields smaller skin friction drag than turbulent flow.

Flow over an airfoil, beginning at the leading edge, will always start out as laminar; then, at some point downstream, instability within the laminar boundary layer will excite some turbulence within the flow before the boundary layer becomes fully turbulent [8]. The point at which this occurs is called the transition point, defined by $x_{cr.}$ This is displayed in Figure [11].

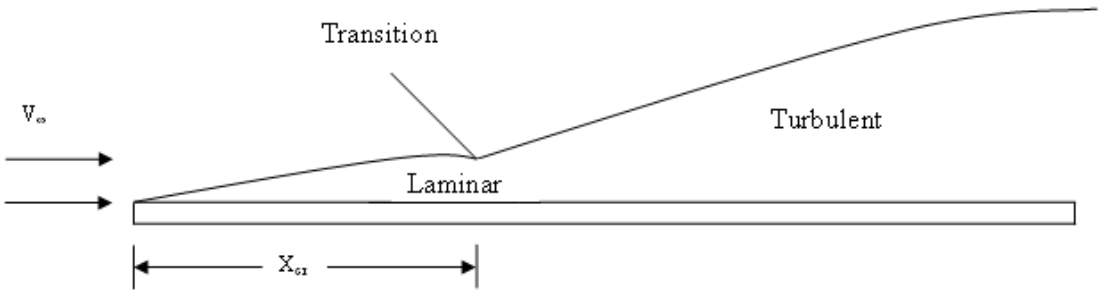

Figure 11 – Normal transition form laminar to turbulent flow on a flat plate [8]

Determining the location of the transition point is very important when attempting to calculate the skin friction drag. Its location is dependent on many factors, one being the presence of adverse pressure gradients. An adverse pressure gradient is defined as a region where the pressure increases in the flow direction [8]. This condition is largely responsible for flow separation from an airfoil surface. Severe adverse pressure gradients reduce the kinetic energy of the flow and thus, slow the velocity of the fluid down to zero at the boundary layer where the flow can become reversed and hence, separated, modifying the lift and drag distribution [9]. The separated flow creates a large wake of turbulent, recirculating flow, downstream from the point of separation, which increases drag, due to an increase in pressure drag and significantly reduces lift, leading to stall [8].

3.2.6 Flow Separation

The causes of flow separation can be illustrated by examining the typical pressure distributions over the upper surface of a hypothetical airfoil at two varying angles of attack, shown in Figure [11]. Flow separation is barely noticeable on the lower surface, with the exception of the aft movement of the stagnation point from the leading edge [9]; therefore any evidence of flow separation will be most visible in the pressure distribution over the upper surface, where the distribution is notably altered

In the first regime, the airfoil is at zero degrees; here the flow moves smoothly around the airfoil, remaining fully attached to the upper surface with no presence of flow separation taking place [8]. There are a number of indicators within the pressure distribution that can help us draw this conclusion. At the leading edge (x/c = 0) Cp =1; indicating a stagnation point where the flow slows down to zero velocity and the static pressure is at its maximum value (stagnation pressure). Proceeding this event, the flow expands rapidly around the upper surface and the pressure decreases dramatically, reaching a minimum value at around 10 percent of the chord length downstream from the leading edge [8]. Moving further downstream, the pressure gradually starts to increase inducing a mild adverse pressure gradient. This fairly benign gradient is small enough to keep the flow fully attached to the upper surface, which recovers to a value slightly above the freestream pressure (Cp = 0) at the trailing edge (x/c = 1.0).

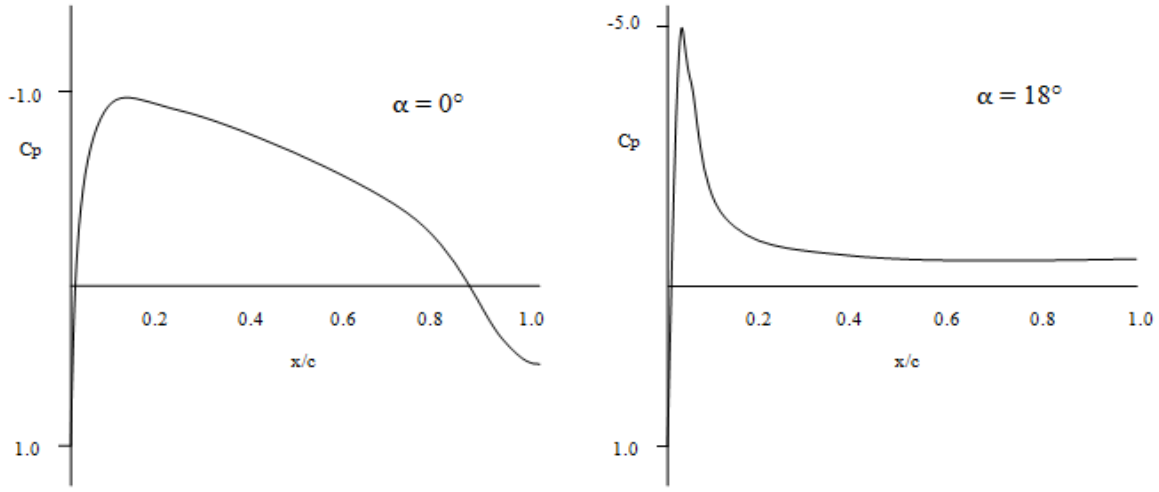

Figure 12 – Typical pressure distributions over the upper surface of an airfoil [8]

In the second regime, the angle of attack has increased to eighteen degrees. At this angle, the viscous forces within the flow are strong enough to cause flow separation. Here the initial decrease in pressure is much greater, reaching a minimum value within the first 5% of the chord downstream from the leading edge. The flow is then subjected to severe adverse pressure gradients where the pressure increases rapidly as the flow moves downstream from the leading edge. This is illustrated by the strong negative gradient shown in the pressure distribution just downstream from 5% of the leading edge. As a result, the flow begins to separate from the upper surface. Proceeding this event, the pressure distribution becomes flat where Cp values close to -1 are witnessed across the majority of the upper surface and the flow fails to recover above the freestream pressure at the trailing edge. This indicates that the flow is stalled and has become separated from the upper surface [10]. When an airfoil becomes fully stalled, Cp values close to -1 will be witnessed across the entire upper surface. The location where the pressure distribution suddenly becomes flat over the upper surface is known as the separation point. For thick airfoils, like the ones employed on the blades of a wind turbine, the flow tends to separate from the trailing to the leading edge [10]. This location will tend to move upstream in the chordwise direction towards the leading edge as the angle of attack is increased [10].

3.2.7 Airfoils for Horizontal Axis Wind Turbines

Airfoils for horizontal axis wind turbines are usually cambered, in order to increase the lift coefficient and decrease the drag coefficient at low angles of attack, where they are generally designed to operate [1]. A schematics of a NACA 64-418 airfoil, which is commonly used in wind turbine applications, is shown in Figure [13]. In the NACA series the last two integers indicate the maximum section thickness as a percentage of the chord [1]. Note the thickness of the airfoil; airfoils for horizontal axis wind turbines are generally thicker than those used for other aerodynamic applications. This is because thicker airfoils exhibit much gentler stall characteristics in comparison to thin ones. Stall regulated wind turbines often operate in the stalled region of operation [1]. The change in magnitude of the aerodynamic loads during stall can be reduced using thicker airfoils, minimising the structural impact of any induced vibrations as the blade enters stall.

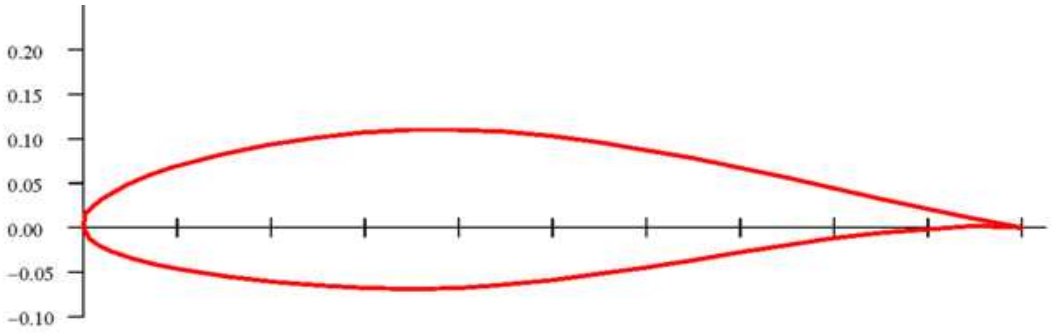

Figure 13 – NACA 64-418 airfoil [20]

Figure [14] summarises some of the design considerations for HAWT airfoils and is adapted from work performed at TU Delft in the Netherlands. The root of a blade will generally incorporate a thick airfoil to provide added structural support and to reduce the impact of stall, which is more pronounced towards the inner section of the blade [11]. Towards the tip, thinner airfoils are employed to minimise drag and maximise the lift/drag ratio as the majority of the useful lift is produced in this region [11]. A higher or more favourable lift/drag ratio is one of the main design goals of an airfoil. It is also an important

consideration when determining the operating conditions of the blades. By plotting the lift/ drag ratio against the lift coefficient over a range of AoA, an optimum design lift coefficient can be determined, e.g. the lift coefficient at which the maximum lift to drag ratio occurs. Modern airfoils for HAWT have also been designed to reduce the impact on performance of blade surface degradation which is more pronounced towards the outer sections of the blades [12].

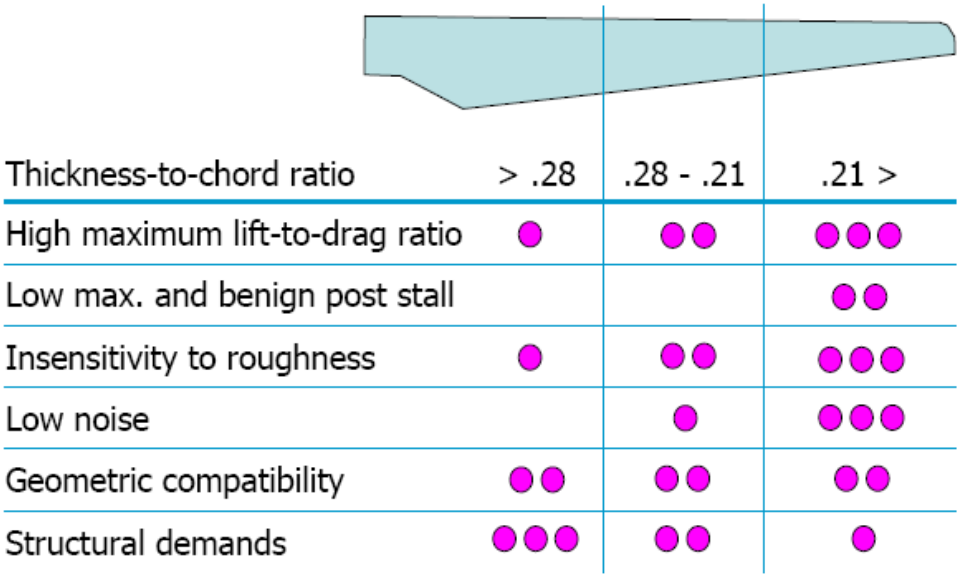

Figure 14 – Design considerations for HAWT airfoils [20]

3.3 - Predicting Performance, BEM

The performance of a HAWT can be predicted using the Blade Element Moment (BEM) method; this is used in the majority of all wind turbine design codes to predict the power and blade airloads for a given turbine geometry and set of operational conditions [13]. Other methods which are in the development stages and hence, less widely employed include: Lifting line, panel and vortex wake methods, Actuator disk method, Navier-Stokes solvers and methods based on cascade theory, commonly used in turbomachinery design [1]. The BEM theory equates two methods for determining the operation of HAWT. The first method

examines the forces on a fluid element within the flow field by applying a momentum balance to a rotating annular stream tube passing through a turbine [14]. The second method involves splitting the blade into a number of discrete elements in the spanwise direction; usually around 21, and examining the forces generated by the airfoil lift and drag coefficients [14]. The two methods provide a series of equations which can be solved iteratively to determine the blade forces and overall power output. Inputs for BEM include the turbine geometry (e.g. radius, n_o of blades), the operational conditions (e.g. wind speed, rpm) and the lift and drag polars for the turbines employed on the blades. Figure [15] displays the complete blade geometry for the analysis of a horizontal axis wind turbine using BEM.

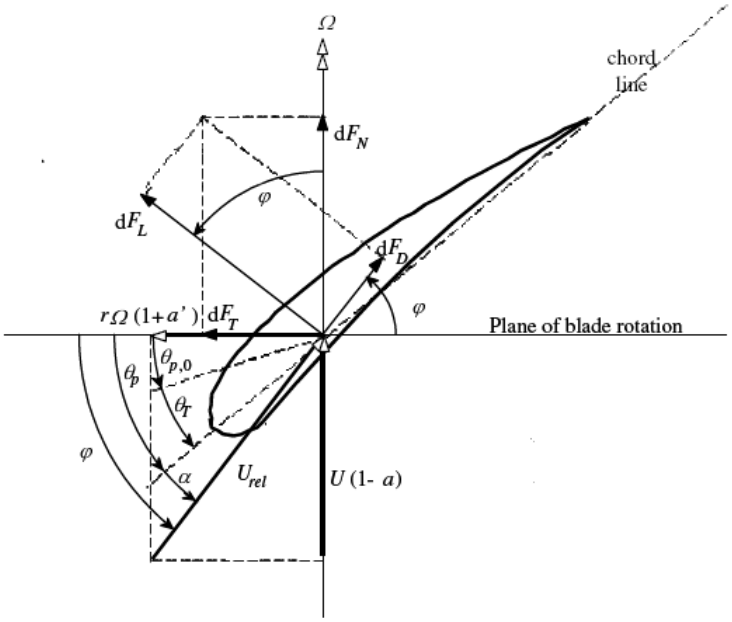

Figure 15 – HAWT blade geometry and force system [1]

Of particular note are the relative wind velocity, U_{rel} and its components $U(1-a)$ expressing the wind velocity at the blades, and $r\Omega(1+a')$ expressing the tangential velocity that the blades experience due to their rotation; a represents the axial induction factor, which corrects the wind velocity to account for the slowing of the air as it passes through rotor plane; a' represents the angular induction factor, which corrects the tangential velocity to account for the speeding up of the air in the rotational plane. This highlights a fundamental aspect of a wind turbines operation, in that the local velocity experienced by the blades and hence, blade forces will vary as a function of radius [1]. Other symbols of note are

d$F_{N,}$ which is the incremental force normal to the plane of rotation and contributes to the thrust [1], and dF_{T}, which is the incremental force tangential to the circle swept by the rotor and is largely responsible for generating useful torque and hence, power [1].

Typical outputs of a BEM code include the power coefficient (C_p), which effectively indicates how efficiently a turbine extracts energy from the wind, and the thrust coefficient, which is the non-dimensional value of the force normal to the rotor disk plane and is commonly used in the structural modelling of a wind turbine.

3.4 - Steady and Unsteady HAWT Aerodynamics

The analysis of a wind turbines aerodynamic performance using BEM assumes that the flow is uniform and steady through the swept rotor area, e.g. there are no temporal changes in wind speed. The main factor affecting the aerodynamic loads during steady state operation is the change in the effective wind speed with the spanwise position along the blades [15], which is appropriately modelled in BEM.

Effect	Flow Structure	Major Consequence
Yaw misalignment	Dynamic (Periodic)	Reduced turbine lifetime
Wind turbulence and gusts	Dynamic (Aperiodic)	Transient spikes in power output
Three dimensional flow (stall delay)	Steady	Underestimated power and loads
Turbine wakes	Dynamic (Aperiodic)	Reduced turbine lifetime

Table 2 – Unsteady aerodynamic phenomena and corresponding impact on turbine lifetime and performance

However, in reality the flow field around a wind turbine is much more complex and time variant; meaning, the idealisation that the flow is always uniform and steady is not a good representation of the true flow field [15]. Certain steady and unsteady aerodynamic phenomena can induce dynamic loads on the rotor which may not be modelled in some BEM codes. A number of these effects and their impact on load and power prediction are summarised above in Table [2].

Chapter 4

Current Issues in HAWT Aerodynamics

In the previous section we have identified some of the fundamental concepts associated with HAWT aerodynamics, in particular the behaviour of viscous flow and the causes of non-ideal steady and unsteady flow. We have also been introduced to BEM theory - a method used for predicting the performance of HAWT - and the background behind its empirical inputs. Knowing some background behind these concepts is important in order to appreciate some of the issues currently facing the field of HAWT aerodynamics. Major challenges within this field tend to fall under the same category: developing improved modelling techniques to improve the load and power predictions of BEM. As shown in *Section 1.5*, an improved prediction of the aerodynamic loads and energy yield can increase the turbine lifetime and improve economic projections, increasing the cost effectiveness and reliability of the technology.

One large area of research has focused on developing a better understanding of the underlying flow physics associated with certain aerodynamic phenomena, in order to accurately model the flow behaviour associated with non-ideal steady-state and unsteady aerodynamics. For example, understanding the development and catastrophic impact of the cyclic airloads associated with dynamic stall, occurring when the rotor is yawed to the oncoming flow remains one of the focal points of current research within this field. Over the years, a number of dynamic stall models have been developed and used in performance analysis codes, most notably the Gormont (1973) and the Beddoes and Leishman dynamic stall model (1993) [16]. Here semi empirical correction factors have been introduced in BEM in an attempt to account for the rapid changes in angle of attack experienced during dynamic stall.

In order to accurately predict the rotor performance using BEM, it is also imperative to have an accurate assessment of the characteristics of the airfoils being employed on the device, e.g. the lift and drag polars. Inaccurate estimations of the aerodynamic coefficients can lead to

miscalculated load and power estimations, and misjudged economic projections [17]. The optimum outcome would be to use high quality experimental data, gathered for the chosen airfoils during a range of comprehensive wind tunnel tests [17]. However, this information is often not available and can be very expensive to gather or gain a license for. The other option is to use computational methods. This situation has presented another major challenge within the field of HAWT aerodynamics: the need for reliable, low cost methods for predicting aerodynamic characteristics of airfoils. Examples of computational methods for calculating airfoil characteristics include: airfoil design and analysis codes (e.g. XFOIL, RFOIL, and Eppler), computational fluid dynamics (CFD) solvers, based on full evaluations of the Navier-Stokes equations (e.g. Fluent) and coupled potential-flow/boundary layer methods (e.g. VSAERO). The main challenge in using these software packages is to provide a fast, accurate set of reliable airfoil characteristics at a justifiable cost. This can be an issue when using a CFD solver. For an accurate CFD solution, a large amount of computational power and time is required, which can be very costly [18]. Moreover, powerful CFD codes are often not commercially available as a routine design tool. Other issues arise when using CFD for predicting the aerodynamic coefficients of airfoils. For one, it cannot accurately predict transition over the surface of an airfoil from laminar, two dimensional flow to unsteady turbulent, three dimensional flow [18]. It also has difficulty in predicting some of the effects of flow separation, and skin friction drag in turbulent flows [18]. Airfoil design codes like XFOIL and RFOIL are open source and provide a cheap and fast solution, yet issues can arise when trying to achieve a converged solution at high Reynolds numbers [19]. Despite these issues, the use of commercially available computational methods can still produce relatively accurate results if used correctly and a good knowledge of wind turbine airfoil aerodynamics is known.

Chapter 5

Project Aim

This project aims to highlight and address some of the issues currently facing the modelling of 2D wind turbine airfoil characteristics using commercially available computational methods. The majority of the published results of using computational methods (such as CFD) to calculate wind turbine airfoil characteristics used in-house research codes that are not yet readily available to the public. In industry, a typical wind turbine designer would not have access to these codes and would have to rely on commercially available codes to determine airfoil characteristics. It is therefore an aim of this project to simulate this type of situation and determine the limitations and difficulties involved.

For this study, two airfoils were selected, which were both employed on the recent experimental model used for the Mexico (Model Experiments in Controlled Conditions) project. This tested a model wind turbine in the largest wind tunnel in the EU, producing a database of detailed aerodynamic data. 2D static experimental data for the two airfoils are available and used to validate the results from three computational tools. The tools used in the analysis are the airfoil design and analysis codes, XFOIL and RFOIL and the CFD package, Fluent. The criteria for selecting these tools were: they were representative of most commercially available codes with the ability to run on a desktop workstation. Each code is applied to examine its ease of use and accuracy when attempting to reconstruct the experimental coefficients of the two airfoils over a range of AoA. Having no previous experience in the use of the computational tools employed in this project, a secondary aim is to develop a methodology for other first time users, attempting a similar goal.

A secondary aim is to examine how the deviations in the aerodynamic coefficients between the experimental and computed data may affect the prediction of the rotor performance of a turbine when using computational methods to determine airfoil characteristics. This is performed using a simple BEM code.

Chapter 6

The Experimental Data

6.1 - The Airfoils

The two airfoils examined in this project are the NACA 64-418 and Du91-W2-250 airfoil sections. The Du91-W2-250 airfoil was designed and manufactured at TU Delft in the Netherlands, where a large majority of the airfoils employed on today's currently operating wind turbines are produced. Both were included in the model recently tested during the Mexico project, carried out by a consortium of members including TU Delft. The project, which was completed in December 2006, tested a large model wind turbine in the wind tunnel of the Large Scale Low Speed (LLF) Facility of the German Dutch Wind Tunnel Facilities (DNW). The core objective of the project was to reduce the uncertainties in the computer codes used to predict the structural loads and performance output of a HAWT. The product was a database of high quality experimental data, recorded on model three bladed, stall-regulated wind turbine in a large wind tunnel under a number of controlled and known conditions [9]. This data has been determined as the only set detailed and accurate enough for validating Navier Stokes based calculation techniques (e.g. CFD) as well as turbulence and transition modelling [9].

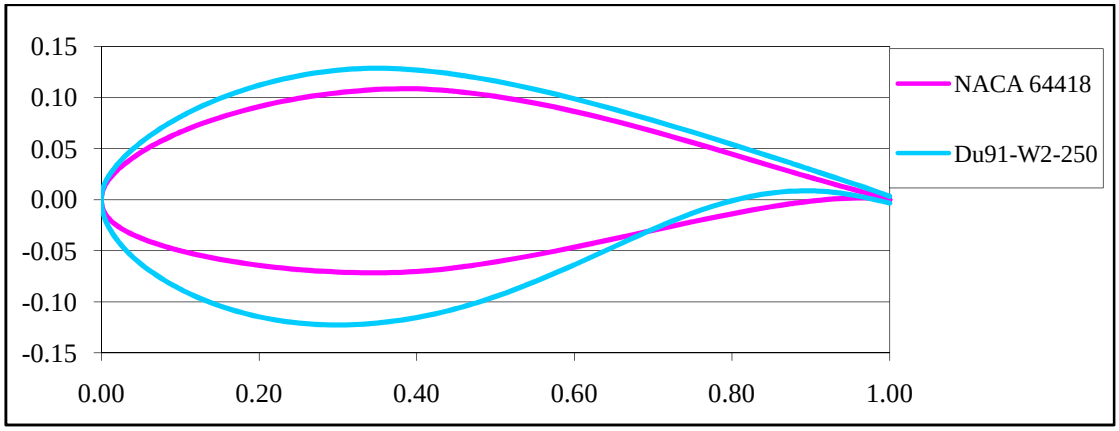

Figure 16 – Du91-W2-250 inboard and NACA 64-418 outboard airfoil sections [20]

To supplement to the tests carried out on the 3D model, a numberof 2D static tests were also performed on the chosen airfoil sections within the Low Speed Wind Tunnel at TU Delft. The airfoils employed on the model which are analysed in this report are displayed above in Figure [16]. A schematic of the wind tunnel is also illustrated below in Figure [17].

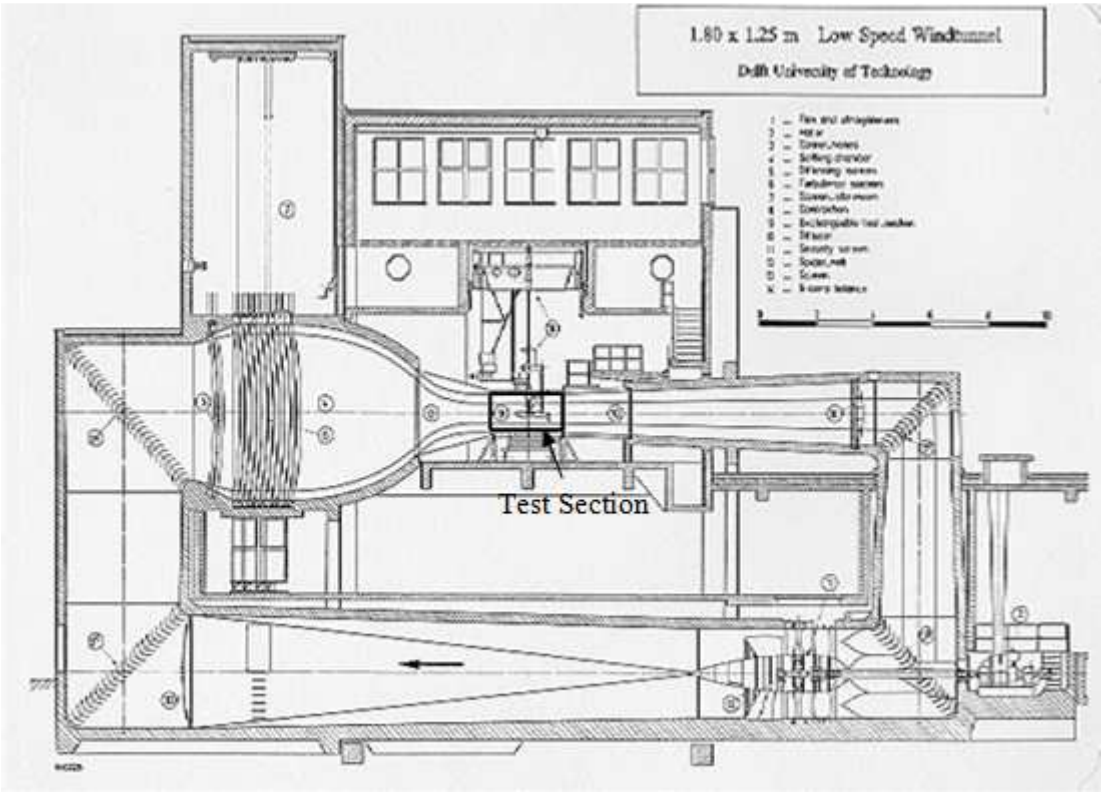

Figure 17 – Schematic of the low speed wind tunnel – Delft University of Technology [20]

The two airfoils analysed in this report represent the airfoils employed at the root (Du91-W2-250, 25% thick) and outer (NACA 64-418, 18% thick) sections of the blades. These were chosen to highlight the differences in the airfoil characteristics between the inner and outer regions of the blades.

6.2 - 2D Static Airfoil Data

After carrying out a previous Masters project at TU Delft, analysing the unsteady aerodynamics of HAWT with reference to the Mexico data, access to the experimental 2D airfoil characteristics was granted by the University. The data set includes for both the Du91-W2-250 and NACA 64-418: the airfoil co-ordinates, their aerodynamic coefficients over a range of AoA for varying Reynolds numbers and some pressure distributions at a few chosen AoA. The force coefficients were derived directly from the surface pressure measurements at three varying Reynolds number per airfoil. Polars of this data were developed and used as a reference set for the computational tests. Pressure distributions were only provided for one Reynolds number per airfoil. Comparisons between computed pressure distributions and experimental tests were therefore made at those values. The full set of polars and pressure distributions from the 2D static tests of each airfoil is displayed in *Appendix 1* and *Appendix 2*.

6.3 - 2D Static Wind Tunnel Performance

Appendix 1 displays the characteristics for the Du91-W2-250 airfoil. Considering $Re = 500{,}000$, at $\alpha = 0°$ the positive camber effects, induced by the shape of the airfoil near the leading edge results in the generation of a predominant normal force, producing a positive lift force with $cl = 0.4$ [21]. The pressure distribution ($Re = 500{,}000$) indicates that the flow is fully attached over the entire upper surface: favourable pressure gradients occupy the region of the LE and the flow recovers to above the freestream pressure at the TE. However, in the absence of any strong LE suction pressure, the lift coefficient remains fairly low. From $\alpha = -12\ to\ 10\ °$ the lift increases linearly with a steady, yet moderate increase in drag. This region defines the lift curve slope of the airfoil. At $\alpha = 7°$ we can see increased LE suction pressure and the presence of a mild adverse pressure gradient; this causes transition at around $0.35c$. However, the following adverse pressure gradient is not strong enough to cause flow separation and the flow recovers to above the freestream pressure at the TE. Towards the upper region of the lift curve slope, where strong normal forces are observed, a positive gradient can be observed in the pitching moment. At $\alpha = 11\ °$, just prior to stall the maximum lift coefficient is achieved with $cl_{max} = 1.49$. The pressure distribution is

characterised by a large LE suction pressure ≈ -4.0. The transition point has moved towards the LE at $\approx 0.05c$. Downstream from the transition point, the adverse pressure gradients are strong enough to retard the flow in the boundary layer causing it to separate from the upper surface at $\approx 0.7c$. This separation can be observed as flat bar of pressure from $0.7c$ to the TE where the flow fails to recover above the freestream pressure. Following the achievement of cl_{max} the airfoil stalls where a sharp decrease in the normal force accompanied by a rapid increase in the axial force, causes the lift to suddenly drop and the drag to rapidly increase. At this instance, the moment coefficient experiences a sudden negative gradient. As α increases the airfoil moves further towards a fully stalled state, yet the magnitude of the changes in the forces becomes more benign. If more pressure distributions were available we could expect to see Cp values of ≈ -1 consistent over the entire upper surface at $\alpha = 26°$, where a precipitous drop in lift accompanied by a rapid increase in drag and strong nose down pitching moment is observed. At this point the airfoil could be said to be fully stalled. The design lift coefficient for the airfoil at $Re = 500{,}000$ is 1.033 at $\alpha = 5.79°$; this gives a maximum lift/drag ratio of 108.

As expected, the lift curve slope is not affected by changes in the Reynolds number, yet the value of cl_{max} is, where cl_{max} increases with decreasing Reynolds number. The drag coefficient is more affected by the Reynolds number in both the inviscid and viscous regions of the flow, especially at high angles of attack. The moment coefficient also appears to be more sensitive to Reynolds number at higher AoA which is to be expected. At higher Reynolds numbers, the maximum lift/drag ratio increases and occurs at lower design lift coefficients.

Appendix 2 displays the same set of polars and pressure distributions for the NACA 64-418 airfoil. In this case, the pressure distributions were provided for a Reynolds number of 1,000,000. Therefore, considering this case, again we see non-zero lift produced at $\alpha = 0°$ with $cl = 0.3$. From $\alpha = -6$ to 6° the lift increases linearly during the lift curve slope. From $\alpha = 7$ to 16° the rate of increasing lift begins to depreciate and the flow becomes increasingly separated from the upper surface. This can be observed as an aft movement of the separation point in the pressure distributions, from the trailing to the leading edge, as the AoA increases. $Cl\,\max = 1.22$ is achieved at $\alpha = 16°$ where after the lift begins to depreciate and the airfoil enters stall; however, the flow remains attached over the leading

edge of the airfoil, with a strong LE suction pressure coefficient observed in the pressure distribution at $\alpha = 21°$. Finally the airfoil becomes fully stalled at $\alpha = 22°$ with Cp values ≈ -1 consistent over the entire upper surface. The design lift coefficient at $Re = 1{,}000{,}000$ is 0.536 at $\alpha = 2°$; this gives a maximum lift/drag ratio of 152.

Reynolds number effects were similar to those witnessed for the Du91-W2-250 airfoil. However, in this case, airfoil characteristics for a Reynolds number of $300{,}000$ were produced. At this low tunnel speed, the behaviour of the polars tended to deviate more from those at the other two Reynolds numbers, in comparison to the Du91-W2-250 case, where the lowest Reynolds number tested was $500{,}000$. Looking at the lift polar, the behaviour of the airfoil in the stall regime is particularly different. Moreover, the moment coefficient distribution is notably different over the full range of AoA. At low Reynolds numbers, viscous effects on lift and drag are more pronounced in the lead up to and during stall, where flow separation begins to dominate the behaviour of the airfoil. As a result, the airfoil appears to stall at a lower AoA, resulting in a modified lift curve and moment coefficient. It can therefore be concluded that Reynolds number effects are minimal between $Re = 500{,}000$ and $1{,}000{,}000$ but become more influential below $Re = 500{,}000$ for this particular case.

The major differences between the performances of the two airfoils can be highlighted by considering the airfoil characteristics at $Re = 1{,}000{,}000$. The Du91-W2-250 has a higher $cl\ max$ which occurs at lower angle of attack, yet the airfoil produces a lower maximum lift/drag ratio. The NACA 64-418 exhibits a more benign post stall regime with gentler gradients in lift and drag observed. This is expected as the NACA 64-418 is employed on the outer section of the Mexico model where a higher lift/drag ratio, low $cl\ max$ and benign post stall regime is desired. This is highlighted in Figure [14]. Additionally, for stall regulated rotors, a restrained maximum lift coefficient allows for the use of a greater swept disk area and hence, better peak power control for a given generator size [22]. The Du91-W2-250 is 7% thicker than the NACA 64-418 and was employed on the inboard section of the blades where structural demands are more of a concern than aerodynamic performance.

Chapter 7

Computational Methods

The aim of this section is to give a brief description of the computational methods used within this project to reconstruct the 2D static experimental data of the two selected airfoils. It begins with a description of CFD and the software package, Fluent before describing the two airfoil design and analysis codes, XFOIL and RFOIL. Finally it ends with a short description of the BEM code provided by the researcher, Tom McCombes; this is used to highlight the discrepancies in using the airfoil characteristics calculated by each method to determine a wind turbines power output.

7.1 - CFD

7.1.1 - Introduction

The value of CFD in the field of aerodynamics is unprecedented. Since its introduction in the early 1960's, it has served as a tool for providing exact solutions to many complex aerodynamic flow fields that without it, would never have been solved theoretically [8]. CFD uses high speed digital computers to solve the full Navier-Stokes equations for any three-dimensional, steady, unsteady, incompressible, compressible, inviscid or viscous flow problem. How does it do this? In reference [23] CFD is defined as "the art of replacing the integrals or partial derivatives in the governing equations with discretized algebraic forms, which in turn are solved to obtain numbers for the flow field values at discrete points in time and/or space". In short, the final product is a numerical solution to the governing equations as opposed to a closed form analytical solution [24].

In terms of its application to wind turbines, and in the context of this report, CFD has began to replace wind tunnel testing for attaining the aerodynamic characteristics of airfoils and complete wind turbine systems. A general trend has developed where the cost of

computations has decreased compared to the increasing cost of wind tunnel tests, making it economically attractive [23]. However, this is making the assumption that the CFD solution is accurate and cost/time effective. In reality, the solution is not always accurate due to the limitations of CFD, described previously in *Section 4.* Moreover, an accurate solution can require a large amount of time and computational power which may not always be available. One of the core aims of this report is to evaluate the accuracy of a commercially available CFD code on desktop workstation within a limited period of time.

7.1.2 - Code Structure

When solving an aerodynamics problem with a CFD code, there are typically three stages that make up the analysis: pre-processing, solving and post-processing [24].

1) *Pre-processing*

   The first stage involves creating a computational domain for the physical surface to be analysed (e.g. an airfoil). This is usually performed using a meshing tool (e.g. gambit) where the domain is split into a number of finite elements (cells) to create a grid. Fluid properties and boundary conditions can then be applied to the grid where it is then ready for exporting to a solver. Careful consideration must be made when defining the resolution of the mesh cells in the grid [24]. For an accurate solution it is ideal to cluster cells in regions where the flow is modified the most [25]; this usually in the region close to the surface of the physical model, known as the near-wall region. Cells can become coarser away from the surface towards the farfield boundaries where the flow gradients approach zero [25]. Accuracy can also be improved by having smooth transitions in cell size, as opposed to large discontinuous changes [25].

2) *Solving*

   The second stage involves solving the problem via a solution algorithm (e.g. fluent). The procedure begins by modelling the problem unknowns as simple analytical functions. These are then substituted into the governing equations; replacing the

integral or partial derivatives, known as discretising [24]. Finally, a method for solving the algebraic system of equations over the complete computational domain is applied. This usually involves iterating the set of equations until a converged solution is reached

3) *Post - Processing*

After solving, each cell, or volume within the grid will now be assigned a number of variables, e.g. a value for velocity or static pressure. The final stage of the process involves analysing the results of the solution to observe the variation in those variables over the complete solved flow field [23]. This can be performed within a complete CFD package (e.g. fluent) but may otherwise have to be done in a post-processing tool. Some examples of post-processing analysis are listed below:

- Reporting wall forces, e.g. moments, normal forces
- Plotting pressure distributions
- Producing contour plots of velocity, pressure, turbulence etc

7.1.3 - RANS equations

As we already know, CFD involves solving the full Navier-Stokes equations for a wide range of practical fluid flow problems. At some point, the behaviour of most flow problems becomes turbulent, where transient, unsteady changes in velocities occur. The treatment of turbulence in the majority of most CFD solvers is to adopt the Reynolds Averaged Navier Stokes (RANS) equations [26]. By averaging a solution at multiple time steps, the effect of turbulence on the time dependant variables in the Navier-Stokes equations can be modelled.

RANS introduces a time-averaged and randomly fluctuating component to each time dependant variable in the Navier-Stokes equations [23]. This inherently produces new terms in the time averaged momentum equation, known as the Reynolds stresses [23]. These terms are functions of the velocity fluctuations and therefore account for the influence of turbulence on the flow problem [26]. The main benefit of RANS is that it makes solutions involving turbulence computationally less expensive to solve [28].

After RANS, the modified equations contain a number of additional unknown variables; in order to produce a closed system of solvable equations and determine these unknown variables in terms of known quantities, a turbulence model is required [26]. There is a number of available turbulence models, those of which used in the analysis within this report will be described later.

7.1.4 - The software – FLUENT and GAMBIT

The commercially available CFD code, Fluent is used in this report to model the 2D flow over two airfoils designed for wind turbine applications. A license for the software was available through the University of Strathclyde, making it an immediate choice. Being a commercially available CFD code and able to run on a desktop workstation, Fluent meets the criteria set out in the aim of this project. In order to create a domain for the problem and hence a mesh to be solved using Fluent, the meshing tool Gambit was also used to supplement the use of Fluent in the CFD analysis. A short description of Gambit will follow before describing some of the key features of Fluent.

7.1.4.1 GAMBIT

Gambit is a design tool used to create mesh models for CFD applications. Users can input commands to Gambit via a graphical user interface (GUI). An example of the Gambit user interface is shown below in Figure [18].

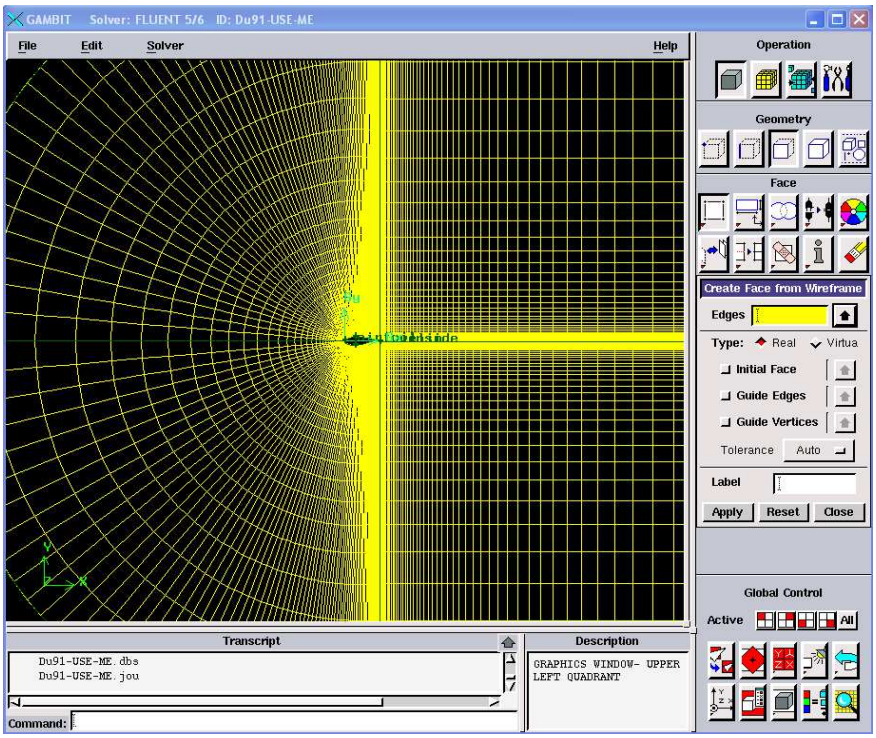

Figure 18 – Gambit GUI

The various command functions allow the user to create a geometry for, mesh and assign zones and boundary conditions to a flow model. A mesh can either be created as unstructured or structured with the differences shown below in Figure [19].

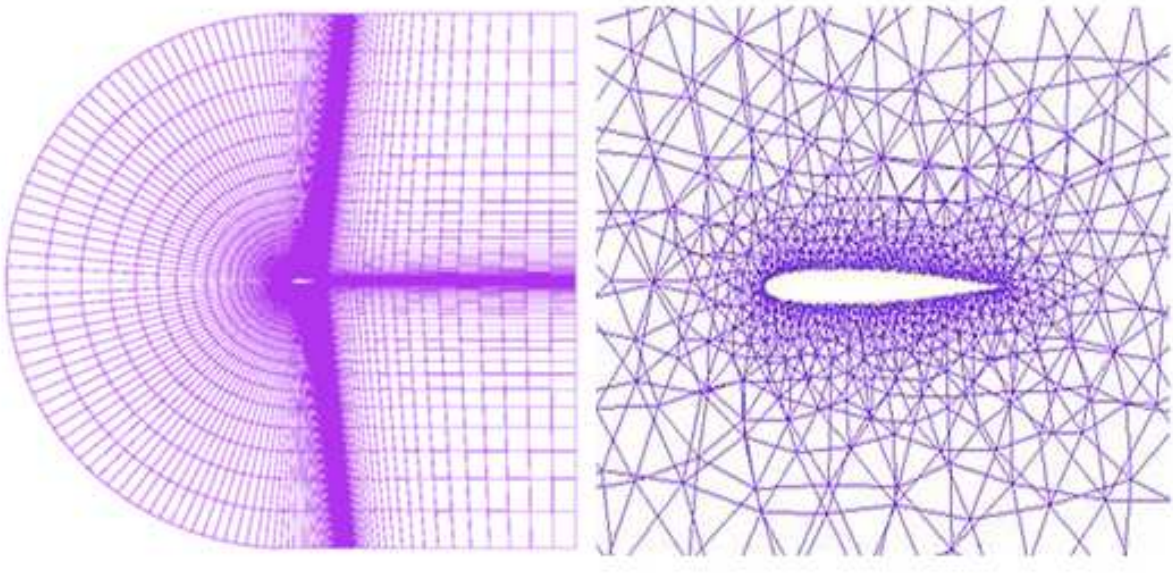

Figure 19 – Difference between a structured (left) and unstructured mesh (right) [44]

The choice of mesh is largely dependant on the geometry to be meshed and the availability of storage, with an unstructured mesh requiring greater storage capabilities [27]. The software also allows the user to input text commands in order to create journal files for creating meshes. By employing programming functions, customized journal files can be created which allow the generation of multiple versions of a single mesh over a fast and convenient period of time.

7.1.4.2 FLUENT

Similarly to Gambit, user inputs to FLUENT are achieved via a graphical user interface, where pull down menus are provided to allow the user to set up the simulation technique. After reading in a mesh previously created in Gambit, the user can set up the simulation in any order but will generally make primary choices based on the following categories:

1) Flow Solver

Fluent has a choice of two numerical methods for solving the solution:

- Pressure-based solver
- Density-based solver

Each method solves the governing equations of a moving fluid by applying a control-volume technique to a generated mesh. Here the integral form of the governing equations are integrated on the individual control volumes to create a series of algebraic equations for the unknowns (e.g. velocity, pressure, turbulent quantities) which are then linearized and solved to give new updated values of the unknown variables [28]. Here the code is always ensuring that the mass, momentum and energy (if compressible flow) is conserved for each cell in the grid. The governing equations are solved repeatedly over a number of iterations until a converged solution is reached.

The pressure based solver is generally used for low-speed, incompressible flows, while the density based solver is used for high-speed, compressible flows [28].

2) Boundary Conditions

Setting up the boundary conditions which specify the flow variables on the boundaries of the physical model is an important stage in the set up of a FLUENT simulation [28]. Boundary zones for the physical model are generally set up in Gambit then assigned inlet and outlet conditions in Fluent, for example: Velocity inlet boundary conditions are used to define the velocity and scalar properties of the flow at inlet boundaries [28].

3) Viscous Model

FLUENT provides a number of viscous models to choose from when setting up a simulation. The choice of the model depends on a number of considerations, such as: the underlying physics related to the flow, the established practice for a specific class of problem, the computational power available, the level of accuracy required and the amount of time available for the simulation [28]. The available models are:

- Inviscid
- Laminar
- Spalart-Allmaras
- k-e
- k-ω
- Reynolds Stress

Choosing the inviscid model will neglect the effect of viscosity on the flow and hence, the effects of fluid viscosity and turbulent viscosity will be removed from the calculation of the forces on the physical model. To include these viscous terms in the governing equations, the simulation must enable laminar or turbulent flow. This can be done by selecting the laminar model or a variation of one of the four turbulence models provided by fluent (Spalart-Allmaras, k-e, k-ω or Reynolds Stress model). Again the choice of the turbulence model will depend on the aforementioned considerations within this section.

Other important considerations that must be made in the set up of the problem are: the materials and corresponding values for the flow problem, e.g. air density for a 2D airfoil problem, and the choice of monitoring for the simulation, for example setting the monitoring for the scaled residuals of continuity, momentum and turbulent terms. Remembering that the CFD code is attempting to find a solution such that mass, momentum and energy are being conserved for each cell, by monitoring the residuals of the variable terms within these quantities we can determine how well a solution is converged. One important step in the fluent software is to set the convergence criterion for the residuals, e.g. the value at which the

iterations terminate. Figure [20] below shows a plot of the residuals for the flow over an airfoil using the Spalart-Allmaras turbulence model with a convergence criterion of 10^{-6}.

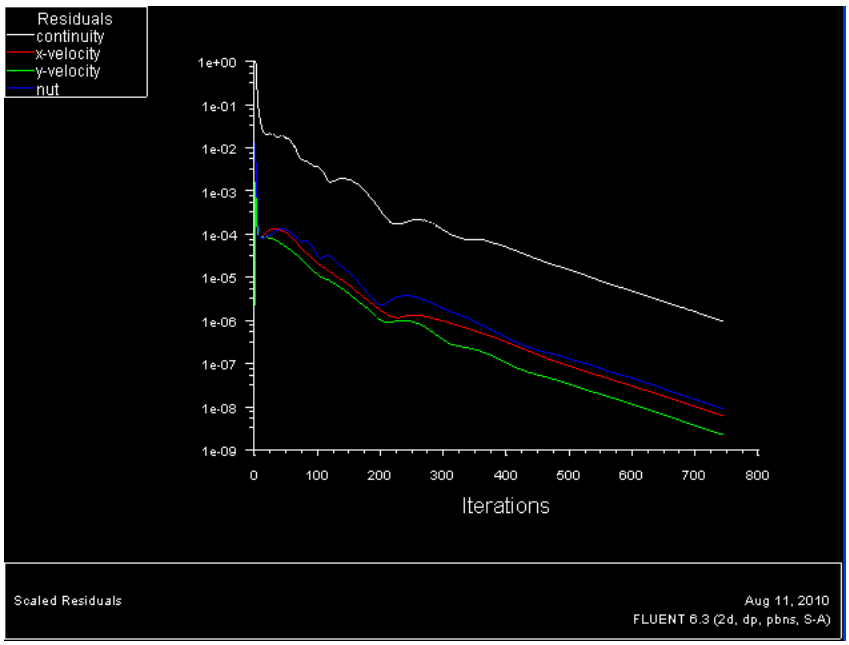

Figure 20 – Residuals plot with convergence criterion set to 10^{-6}

FLUENT is written in C-Language so again this allows for the development of journal files to allow the user to perform modifications to simulations without having to access the GUI. This can make life easier when a large number of simulations on the same grid are required.

FLUENT allows for an extensive range of post-processing, such as the development of contour plots and pressure distributions, and the reporting of wall forces and fluxes. It also has a useful adapt function which allows you to amend a grid in FLUENT, negating the need to re-mesh the model in Gambit.

7.2 – XFLR5

XFOIL is a program which specialises in the analysis and design of subsonic isolated airfoils. This code was chosen for this analysis because it is open sourced and can be easily downloaded and run on a desktop workstation. In this project the recently updated version of XFOIL, XFLR5 is used. In this version a graphical user interface replaces the old command driven format of the original XFOIL; however the functions and operations of the code remain the same. The GUI for XFLR5 is shown below in Figure [21]. A set of airfoil co-ordinates can be loaded into the program and

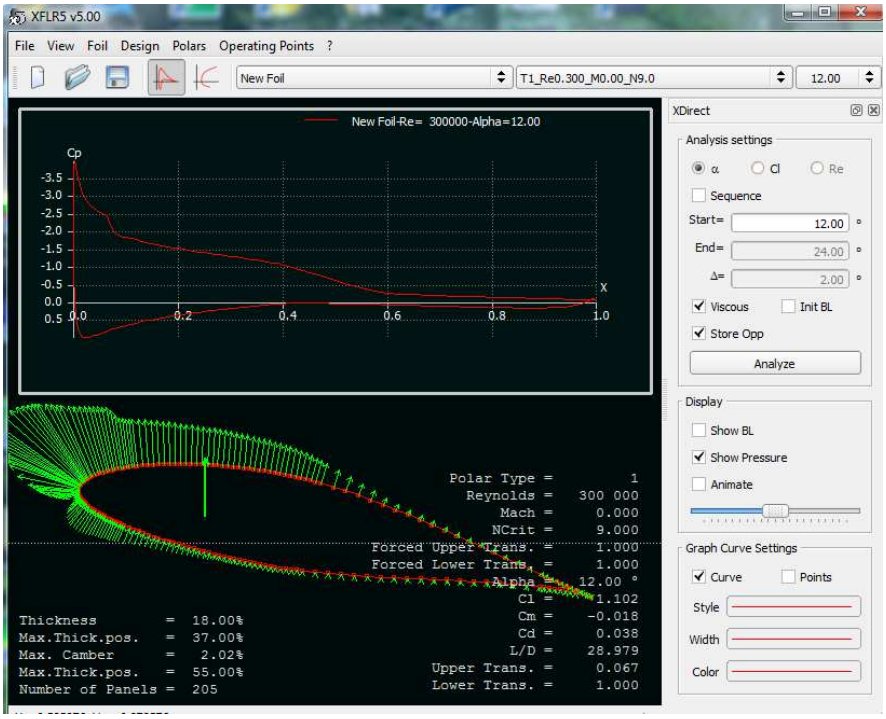

Figure 21 – XFLR5 GUI

analysed in a number of ways. In this case a pressure distribution of the airfoil has been produced for an airfoil at $\alpha = 12°$. Useful functions which can be performed include:

- Viscous or inviscid analysis of an existing airfoil
- Plotting of geometry, pressure distributions, and polars

- Airfoil design and re-design by specification of new geometric parameters

For a full description of the methodology behind XFLR5, refer to reference [29]. Some of the fundamental features are however described below.

7.2.1 Inviscid Formulation

For calculating inviscid flow, XFLR5 uses a linear vorticity stream function panel method [30]. Panel methods are fast and effective for modelling fully attached, incompressible flow (e.g. potential flow). As a result they are a popular method in aerodynamics for calculating the lift and pressure drag forces on an airfoil [31]. However, panel methods are incapable of modelling viscous forces and are therefore cannot predict boundary layer effects and separation [31].

7.2.2 Viscous Formulation

To model viscous effects, the boundary layer and wake are modelled with a two equation lagged dissipation integral boundary layer formulation and an envelope e^n transition criterion [31]. The viscous solution is combined with the inviscid formulation allowing the calculation of separated regions of flow. In this configuration the skin friction drag can be calculated and hence, the full lift and drag forces on an airfoil can be determined for both viscous and inviscid flow. In terms of determining free transition within the flow, XFLR5 uses the e^n transition criterion. Here the user can specify the parameter, Ncrit "which is the log of the amplification factor of the most amplified frequency which triggers transition" [31]. For standard wind tunnel tests this is assumed to be 9 and is the default prediction for the location of transition using XFLR5.

7.3 – RFOIL

RFOIL is a modified version of XFOIL which was developed at Delft University of Technology. Again, it is open sourced and can be downloaded and run on a desktop workstation; therefore, it was chosen to supplement and form a comparison to the results produced by XFLR5 and CFD. Unlike XFLR5, RFOIL is a command driven program without a GUI, however it can perform the same number of operations and functions. The main drive behind the development of RFOIL was to create an airfoil design and analysis code which could include the effect of rotation on airfoil performance [32]. The effect of rotation has shown to delay stall beyond that predicted by 2D airfoil data towards the inboard sections of wind turbine blades.

The first step towards achieving this was to improve the two dimensional post stall prediction of XFOIL. An issue with XFOIL was that the code broke down and failed to converge at high angles of attack when an airfoil entered the post stall regime [32]. To overcome this, adjustments to some of the closure relations for the turbulent boundary layer formulation were made in RFOIL, resulting in improved predictions for airfoil stall characteristics up to and above angles of 25 degrees [32]. These adjustments improved the prediction of the turbulent separation point, which is an important flow parameter with respect to rotational flow effects [32].

With the prediction of stall improved the next step was to include 3D radial flow equations in the XFOIL boundary layer formulation. With these adjustments made the code was shown to improve the prediction of the maximum lift coefficient and the angle of attack at which stall occurred for a given airfoil. For a more full description of the adjustments made to XFOIL refer to reference [32].

7.4 BEM code

The BEM code used in this analysis was produced by Tom McCombes and was written in the programming language, Matlab. The code accepts user inputs for a specified turbine geometry e.g. blade radius, no of blades, twist distribution and hub pitch setting, and lift and drag data for the airfoil employed on the blades. Inputs for the operating conditions of the turbine are also accepted, requesting the user to specify the maximum and minimum allowable tip speed ratios for the device. The tip speed ratio (TSR) is the ratio between the rotational speed of a blade at the tip and the velocity of the wind, defined in Equation (18) as:

$$\lambda = \frac{\Omega R}{U} - \text{Equation (18)}$$

Where, Ω is the rotational speed of the turbine, R is the radius of the blade and U is the wind velocity. The code splits the blades into a number of user specified elements and applies a BEMT algorithm to determine the thrust and power coefficients over a range of user specified TSR increments. In this process the calculated lift and drag coefficients of the airfoil are used to determine the aerodynamic forces on the blade at each tip speed increment and hence, the torque, thrust and power generated by the turbine. The outputs of the code are plots of the thrust and power coefficient versus tip speed ratio over the specified tip speed range, an example of which is shown below in Figure [22]; the legend indicates the hub pitch angle.

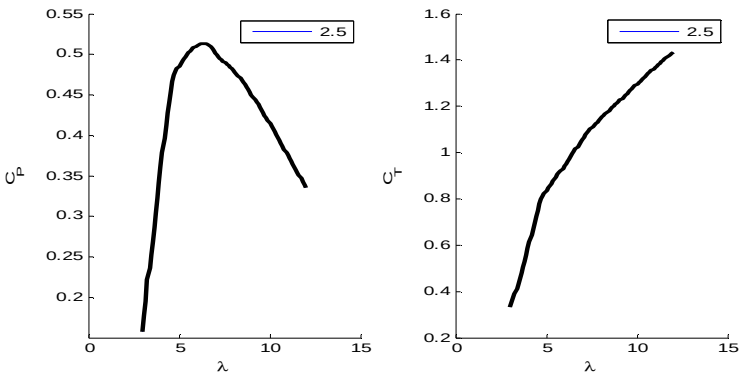

Figure 22 – Example output of BEM code

Chapter 8

Project Approach

In order to reconstruct the experimental airfoil characteristics of the two airfoils chosen for this analysis, the three previously described computational tools were chosen and applied. From the outset it was decided to break the project down into the following two stages:

Stage 1) - *2D airfoil analysis*

The development of airfoil characteristics using the three computational tools coinciding with a direct comparison to the experimental data: airfoil characteristics include: lift, drag, moment, normal force and axial force polars and selected pressure distributions. A look at some of the flow plots produced by CFD is also included in this section to try to define some of the underlying flow physics responsible for the behaviour of the results.

Stage 2) – *BEM analysis*

Making use of a simple BEM code, this section evaluates the impact of the results obtained from the 2D analysis on the power and load predictions for a turbine configuration. The lift and drag coefficients form the 2D analysis form the inputs to the BEM code.

8.1 - 2D Airfoil Analysis

The main body of the work in this section involved becoming familiar with the computational tools and their various operations. Having no previous experience in the use of these tools, this took some time, more so in the use of GAMBIT and FLUENT and less in the use of XFLR5 and RFOIL. Once this was achieved, a methodology for using each code was developed and applied to determine the 2D characteristics of the two airfoils.

To highlight the learning curve and the established methodologies for the 2D airfoil analysis, the following section describes the approach adopted for each code, beginning with the airfoil design and analysis codes, XFLR and RFOIL. It then provides a full description of the methodologies adopted for using GAMBIT and FLUENT.

8.1.1 Methodology – XFLR5 and RFOIL

Producing airfoil characteristics with XFLR5 and RFOIL is a fairly standardised process as this is what the codes were specifically designed for; unlike CFD which is used to analyse a wider class of engineering flows. The instructions for the code are clearly outlined in the user manuals, which were followed for guidance. The basic process involved: (1) loading the coordinates of the two airfoils into the codes, (2) setting up a viscous formulation, (3) defining the Reynolds number, (4) defining the AoA range, (5) running the program, (6) exporting the polars and pressure distributions to EXCEL for analysis. This method could be followed to produce airfoil characteristics in less than ten minutes.

Computed results of airfoil characteristics from XFLR5 and RFOIL were produced for both airfoils at two Reynolds numbers each. Polars of force and moment data were compared against computed results from FLUENT to examine the validity of using each code to reproduce the experimental data. The results from this analysis are presented in *Section 9 – Results and Discussion*.

8.1.2 Methodology – FLUENT and GAMBIT

There is no standardised process for analysing airfoil flows using FLUENT; therefore, the user must establish their own methodology. There exist many recommendations and hints in various forms of literature and these were followed for guidance. Figure [23] shows a road map of the steps taken throughout the course of this project when using CFD to re-produce airfoil characteristics; all steps up to step 11 were completed. These steps will now be discussed in turn

8.1.2.1 - Step (1)

Creating a standard base-line mesh in GAMBIT was the first step in the road map towards developing full CFD simulations of the flow fields around the two airfoils. In order to become familiar with the software, a tutorial provided by the Sibley School of Mechanical and Aerospace Engineering at Cornell University was followed. The tutorial considers the flow over a NACA 4412 airfoil and provides a step by step account of how to mesh an airfoil in GAMBIT. The full tutorial can be viewed in reference [33].

After careful consideration of the advice given in the tutorial, a method was adopted for meshing the two airfoils chosen for this analysis.

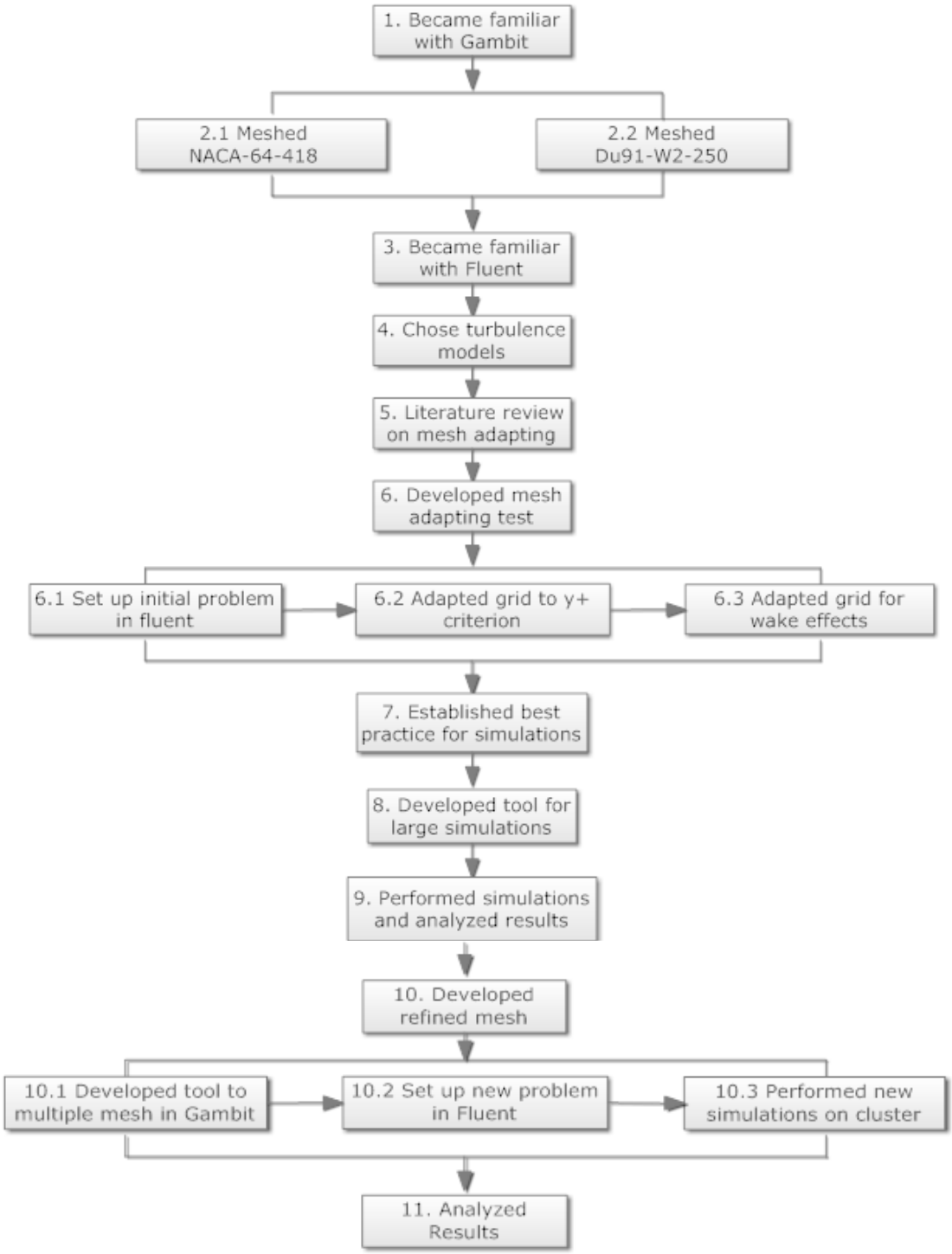

Figure 23 – Road map of steps taken when using CFD for airfoil analysis

8.1.2.2 - Step (2)

The methodology for meshing each airfoil in GAMBIT was as follows. For illustrative purposes the mesh developed for the Du91-W2-250 airfoil is used. An identical mesh was generated for the NACA 64-6418 foil.

1) *Define the Geometry*

Figure [24] displays the geometry created for the mathematical domain of the physical model, where *c* is the chord length of the airfoil. This geometry was set up to create a C-grid in GAMBIT, which is commonly used for structured airfoil meshes. A C-grid around an airfoil has lines of points in one direction which are shaped like the letter "C", where the line which describes the airfoil surface meets at the trailing edge [34].

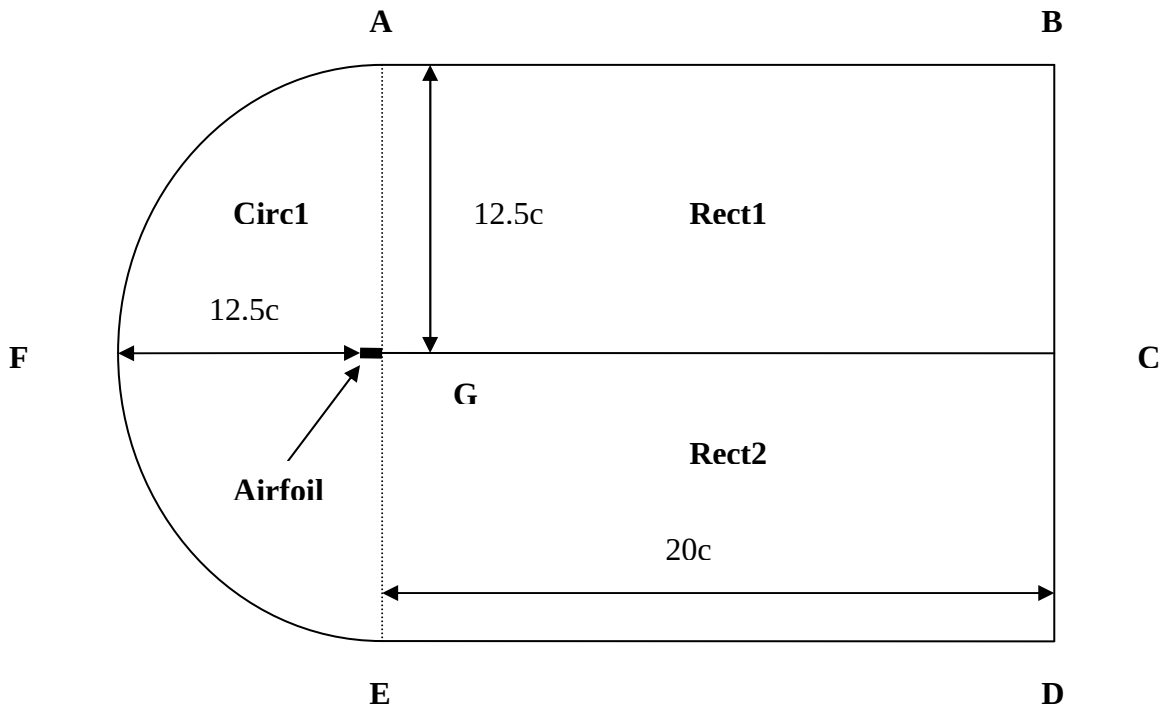

Figure 24 – Geometry of wireframe created in GAMBIT

Here, a farfield boundary is defined at reasonable distance away from the airfoil where ambient conditions are used to define the boundary conditions. Closer to the airfoil surface, large gradients in flow variables (pressure, velocity) will dominate the flow. Creating this geometry ensures the farfield boundary conditions are not affected by the flow around the airfoil making the definition of the farfield boundary condition more accurate.

2) Import Airfoil Co-ordinates and Create Geometry

The airfoil co-ordinates, stored as a dat-file were then be loaded into GAMBIT and the domain geometry was created. Figure [25] shows the airfoil co-ordinates and the wireframe for the C-grid created in GAMBIT.

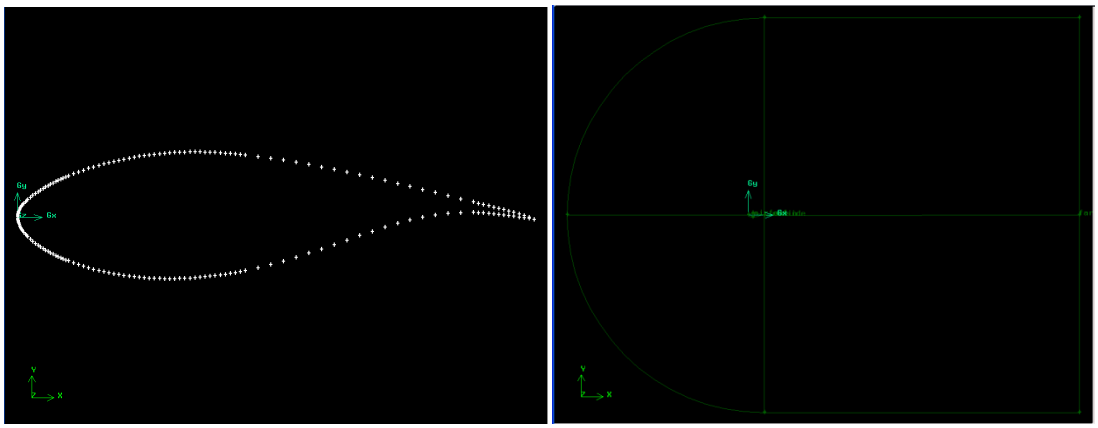

Figure 25 – Airfoil coordinates and wireframe created in GAMBIT

3) Mesh the Geometry

With the wireframe for the grid created, the region between the airfoil geometry and the farfield boundary could then be meshed. A structured mesh pattern was chosen to save computational time. Unstructured grids can be advantageous over structured grids because you do not have to have high resolution in regions where it is not required (e.g. in the farfield) in order to cluster cells close to the airfoil. However, a trade off was made after careful consideration of the time frame of this project. The

two rectangular faces were meshed in order to cluster and refine cells in the region of the wake behind the airfoil as this is where the flow is modified the most. The mesh for this region is shown in Figure [26]. Towards the farfield boundary, where the flow field gradients approach zero, the mesh resolution becomes progressively coarser. The mesh edge command in GAMBIT was used to perform this operation. Careful control of this function was required to ensure the transitions in mesh size were smooth and continuous.

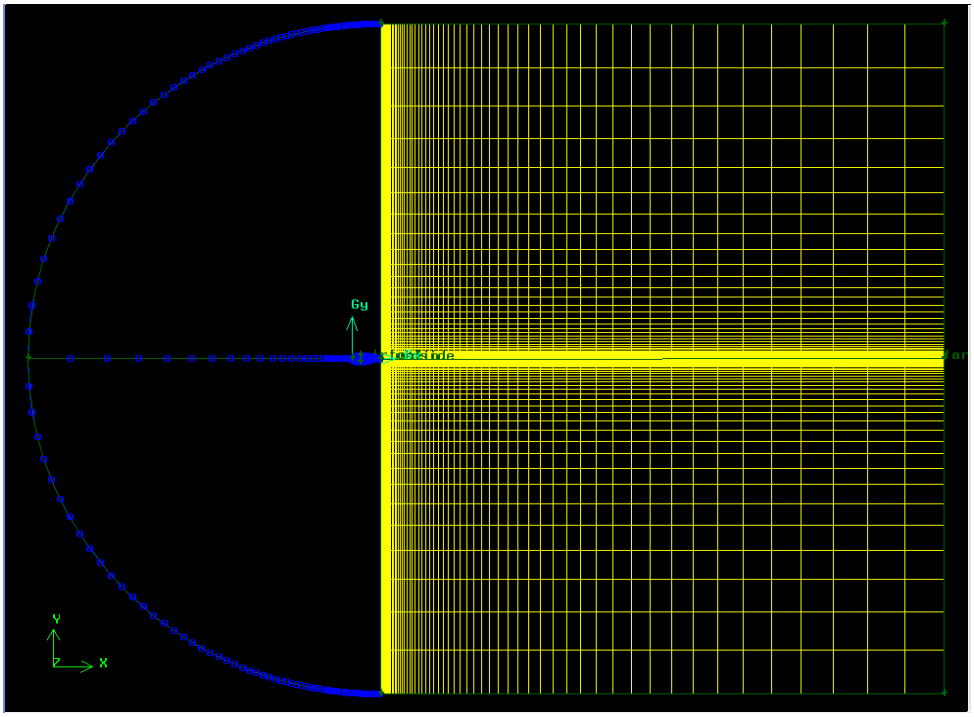

Figure 26 – Mesh generated for rectangular regions of C-grid in GAMBIT

The semi circular face was then meshed, using the mesh edge command function to cluster cells at the airfoil surface in the near-wall region, with added resolution at the leading and trailing edges. Here the steepest gradients are observed and it is critical to have a mesh resolution which allows the solver to calculate these rapid changes in flow variables.

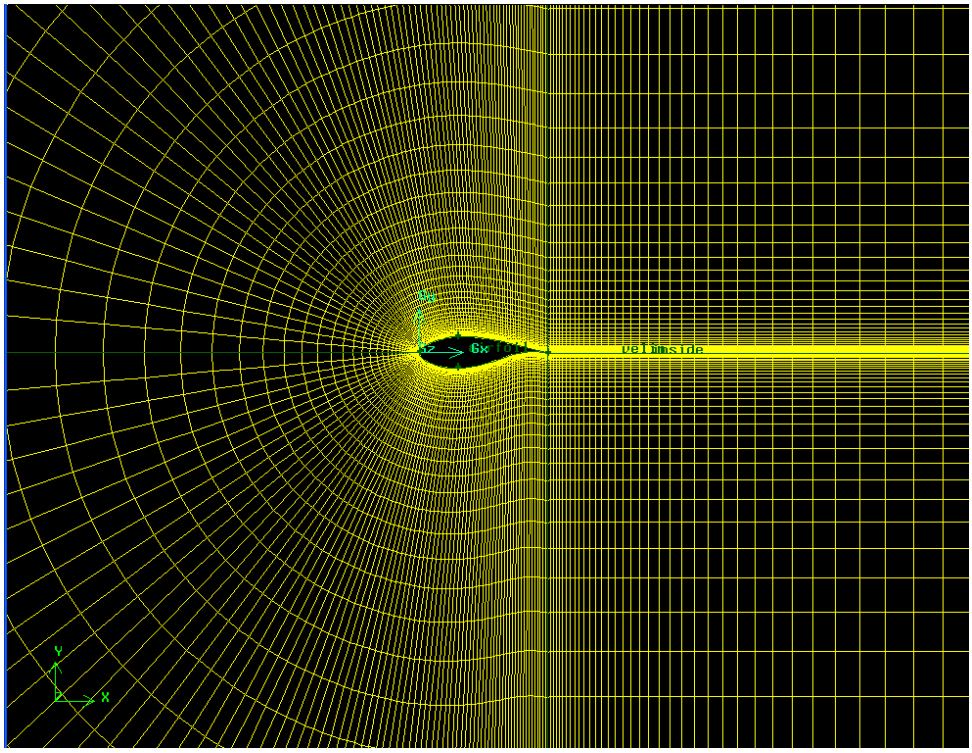

Figure 27 – Mesh Zoomed in showing increased resolution around airfoil surface

Figure [27] shows the mesh resolution around the airfoil with added refined around the leading and trailing edges.

4) Specify the Boundary Types

Three boundaries were then set up for the domain: the velocity inlet, airfoil and the farfield boundaries. This was done by assigning the regions within the domain, group names and specifying a boundary type to each group. The velocity inlet described the boundary for the flow approaching the airfoil. The airfoil described the boundary for the airfoil itself and was defined as a wall boundary and the pressure outlet described the boundary for the flow leaving the airfoil and was defined as a pressure outlet. The final mesh with specified boundary conditions is shown in Figure [28].

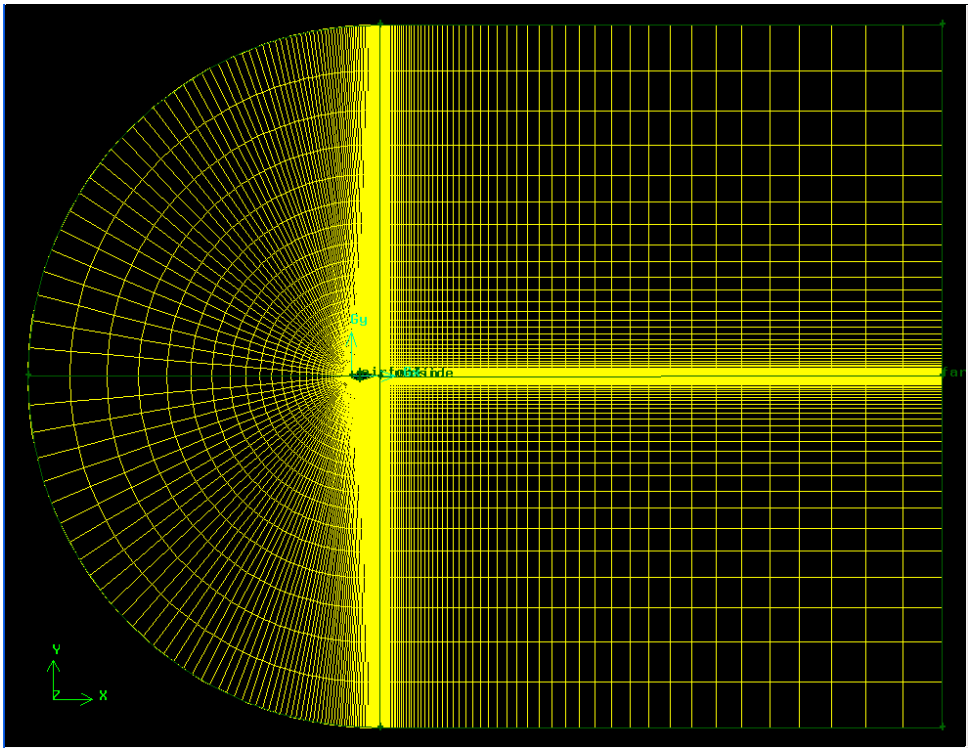

Figure 28 – Image of complete mesh generated in GAMBIT for the airfoil sections

8.1.2.3 - Step (3)

The next stage of the process was to export the base-line mesh generated in GAMBIT into FLUENT and define the solution. Time was taken here to become familiar with the FLUENT software and to fully understand its functionality. To do so, the Cornel tutorial was again referred to which described how to set up a simulation for the NACA 4412 previously meshed in GAMBIT. The FLUENT user guide was also a valuable source for understanding the terms and functions described in the tutorial. Simulations were run on the two airfoils chosen for this analysis, following the Cornel tutorial as a guide. During this initial trial period it became clear how varied the results could be depending on the choice of turbulence model. Early comparisons to the experimental force coefficients showed quite notable discrepancies in the modelled data.

Before carrying out any further simulations it was thought necessary to research the available turbulence models and their applications to my area of research. Additionally, it was deemed

important to research other works of a similar kind to establish the current state of the art for modelling airfoil characteristics using CFD.

8.1.2.4 - Step (4)

Perhaps one of the most important stages in setting up a simulation in FLUENT is the selection of the turbulence model. For this analysis three turbulence models were selected for the purpose of addressing the differences in the outputs of each, with regard to modelling the aerodynamic characteristics of airfoils. Each of the three models used in this analysis employ the Boussinesq Approach to model the variation of the Reynolds stresses with the mean velocity gradients, in the RANS equations. A full description of the Boussinesq hypothesis can be found in reference [35]. An advantage of this approach is the small computational time required to produce simulations as only a maximum of two transport equations are ever solved to model turbulent phenomena. This was a primary reason behind the selection of these models. A transport equation describes the generation, accumulation and destruction of transport phenomena (e.g. turbulent viscosity) by a applying a conservation principal to the transport process [24]. In the case of CFD, the aim is to develop a mathematical formulation that will transport each creative and destructive turbulent term into an algebraic equation at each cell in the grid. This can then be applied to a complete grid to obtain a set of solvable linear equations [24].

The models and the reasons for their selection are now discussed.

1) *Spalart-Allmaras Model*

   The Spalart-Allmaras model was chosen for this analysis because it was specifically designed for low-Reynolds-number, aerospace applications involving wall bounded flows, which is synonymous to the flow over airfoils designed for wind turbines. Additionally, it has been shown to give good results for boundary layers subjected to adverse pressure gradients [28]. The adverse pressure gradients over airfoils and their contribution to flow separation have already been discussed in some detail in *Section 3.* The model itself is fairly simple, comprising of a one equation model that solves a modelled transport equation for the kinematic eddy

(turbulent) viscosity [28]. The kinematic eddy viscosity describes the response of a turbulent fluid to an external perturbation [36]. As this is only a one equation model, simulation times are reduced, which is another reason for choosing this model considering the time frame of this project.

The transported variable in the Spalart-Allmaras model, ν, defines the turbulent kinematic viscosity out with the near-wall viscous affected region [28]. The transport equation for ν is given below in Equation (19) [28].
:

$$\frac{\partial}{\partial t}(\rho\nu) + \frac{\partial}{\partial x_i}(\rho\nu u_i) = G_\nu + \frac{1}{\sigma_\nu}\left[\frac{\partial}{\partial_{x_j}}\left\{(\mu + \rho\nu)\frac{\partial_\nu}{\partial x_j}\right\} + C_{b2}\rho\left(\frac{\partial_\nu}{\partial x_j}\right)^2\right] - Y_\nu + S_\nu \quad \text{Equation (19)}$$

Here, G_ν is the production of turbulent viscosity and Y_ν is the destruction of turbulent viscosity that occurs in the near-wall region due to wall blocking and viscous damping. σ_ν and C_{b2} are constants, and S_ν is a user defined term [28].

2) Standard k-ε Model

The standard *k-ε* model is a simple two equation turbulence model which solves the turbulent velocity scales within a turbulent flow via the solution of two independent transport equations [28]. The model has proven to be robust and reasonably accurate for a wide range of turbulent flows, providing solutions over relatively short simulation times in comparison to other plus-two equation turbulence models. As a relatively crude grid was used for this analysis, the *k-ε* model was chosen for its numerical stability and reasonable accuracy. The model is also semi-empirical, meaning its constants were derived from experiment in an attempt to model the underlying physical phenomena behind turbulent flows. With a respect for empiricism and support for the view that all scientific evidence should be based, as much as possible, on evidence that can be observed through experiment; this model was chosen as a personal preference.

The transported variables in the model are the turbulent kinetic energy (*k*) and its dissipation rate (*ε*). Assumptions made in the derivation of the transport equations for these variables are that the flow is fully turbulent, and the effects of molecular viscosity are negligible [28]. For this reason, the *k-ε* model is only valid for fully turbulent flows.

The turbulent kinetic energy, *k*, and its rate of dissipation, *ε*, are obtained from the Equations (20) and (21) [28]:

$$\frac{\partial}{\partial t}(\rho k) + \frac{\partial}{\partial x_i}(\rho k u_i) = \frac{\partial}{\partial x_j}\left[\left(\mu + \frac{\mu_t}{\sigma_k}\right)\frac{\partial k}{\partial x_j}\right] + G_k + G_b - \rho\varepsilon - Y_M + S_k \text{ - Equation (20)}$$

and

$$\frac{\partial}{\partial t}(\rho \varepsilon) + \frac{\partial}{\partial x_i}(\rho \varepsilon u_i) = \frac{\partial}{\partial x_j}\left[\left(\mu + \frac{\mu_t}{\sigma_\varepsilon}\right)\frac{\partial_\varepsilon}{\partial_{x_j}}\right] + C_{1\varepsilon}\frac{\varepsilon}{k}(G_k + C_{3e}G_b) - C_{2\varepsilon}\rho\frac{\varepsilon^2}{k} + S_\varepsilon - \text{Equation (21)}$$

Here, G_k represents the generation of turbulent kinetic energy due to the mean velocity gradients and G_b is the generation of turbulent kinetic energy due to buoyancy [28]. Y_M represents the contribution of the fluctuating dilation in compressible turbulence to the overall dissipation rate, and $C_{1\varepsilon}$, $C_{2\varepsilon}$ and C_{3e} are constants [28]. σ_k and σ_ε are the turbulent Prandtl numbers for k, and ε and S_k and S_ε are user defined source terms [28].

3) SST k-ω Model

The SST *k-ω* model is an amalgamation blending the robust and accurate formulation of the original *k-ω* model in the near wall region with the free stream independence of the *k-ε* model in the far field [28]. It is similar to the standard *k-ω* model, which incorporates modifications to the *k- ε* model for low Reynolds numbers, but with a few modifications. The most notable difference is the

incorporation of a blending function which activates the *k*- ω model for flows in the near-wall region and activates the transformed *k*-ε model for flows in the farfield [28]. As a result, the model becomes more accurate and reliable for modelling a wider class of flows, including those with adverse pressure gradients, making it suitable for performing an analysis of airfoil characteristics. For this reason the SST *k*-ω model was chosen over the standard *k*-ω model.

The transported variables in the model are the turbulent kinetic energy (*k*) and the specific dissipation rate (ω); these can be obtained from transport Equations (22) and (23)

:

$$\frac{\partial}{\partial t}(\rho k) + \frac{\partial}{\partial x_i}(\rho k u_i) = \frac{\partial}{\partial x_j}\left(\Gamma_k \frac{\partial k}{\partial x_j}\right) + G_k - Y_k + S_k \quad \text{Equation (22)}$$

and

$$\frac{\partial}{\partial t}(\rho \omega) + \frac{\partial}{\partial x_i}(\rho \omega u_i) = \frac{\partial}{\partial x_j}\left(\Gamma_\omega \frac{\partial \omega}{\partial x_j}\right) + G_\omega - Y_\omega + S_\omega \quad \text{Equation (23)}$$

Here, G_k represents the generation of turbulent kinetic energy due to mean velocity gradients and G_ω represents the generation of ω [28]. Γ_k and Γ_ω represent the effective diffusivity of *k* and ω, and Y_k and Y_ω represent the dissipation of *k* and ω due to turbulence [28]. S_k and S_ω are user defined terms [28].

8.1.2.5 Step (5)

By carrying out a literature review of some other works which focused on the modelling of 2D airfoil characteristics, a better understanding of the current state of the art was established. The most notable areas of research and development came in the field of mesh generation and adaption. This appeared to be almost a whole discipline in itself, with many journal papers focussing on methods to reduce the computational time and effort required to produce the

most accurate mesh and achieve grid independence. Grid independence is achieved when further changes in the mesh size does not affect the solution. The classic procedure for determining the most accurate mesh is to perform various test runs on different mesh sizes and configurations until the solution converges and grid independence is achieved [37]. However, this can be quite labour intensive, with much time needed to make adjustments to the grid and run new simulations. The following guidelines establish some recommendations, provided by a review of current literature on how to improve the accuracy of commercial CFD codes, helping to also reduce the computational time and effort required to model airfoil characteristics.

1) The Wall y^+ Criterion for Wall Bounded Turbulent Flows

The wall y^+ is a non-dimensional parameter commonly used in boundary layer theory and in defining the law of the wall [38], defined for a wall bounded flow in Equation (24) as:

$$y^+ = \frac{u^* y}{\upsilon} - \text{Equation (24)}$$

Where u^* is the friction velocity ($u^* = \sqrt{\frac{\tau_w}{\rho}}$), y is the distance to the nearest wall and υ is the kinematic viscosity of the fluid. The law of the wall describes the velocity profile near a solid wall surface, stating that the average velocity U of a turbulent flow can be described in terms of the shear stress at the surface τ_w, the distance to the nearest wall y, the fluid density and the molecular viscosity μ [38]. The law of the wall is defined in Equation (25) as:

$$U^+ = \frac{1}{k} ln\, y^+ + C^+ - \text{Equation (25)}$$

Where U^+ is the average velocity made dimensionless by the friction velocity, k is the Karman constant and C^+ is a constant determined from experiment.

The turbulence models in CFD deal with flow in the boundary layer (near-wall region), which is divided into an inner and outer region. The inner region can be divided further into a laminar (viscous) sub layer and a fully turbulent region [39]. In the fully turbulent region ($y^+ > 30$) the dimensionless mean velocity is governed by the law of the wall. In the viscous sub layer ($y^+ < 5$) the variation of U^+ to y^+ is 1.1 such that: $U^+ = y^+$ [38]. The log-linear relationship between the mean dimensionless velocity and the wall y^+ in the inner region of the boundary layer is shown in Figure [29].

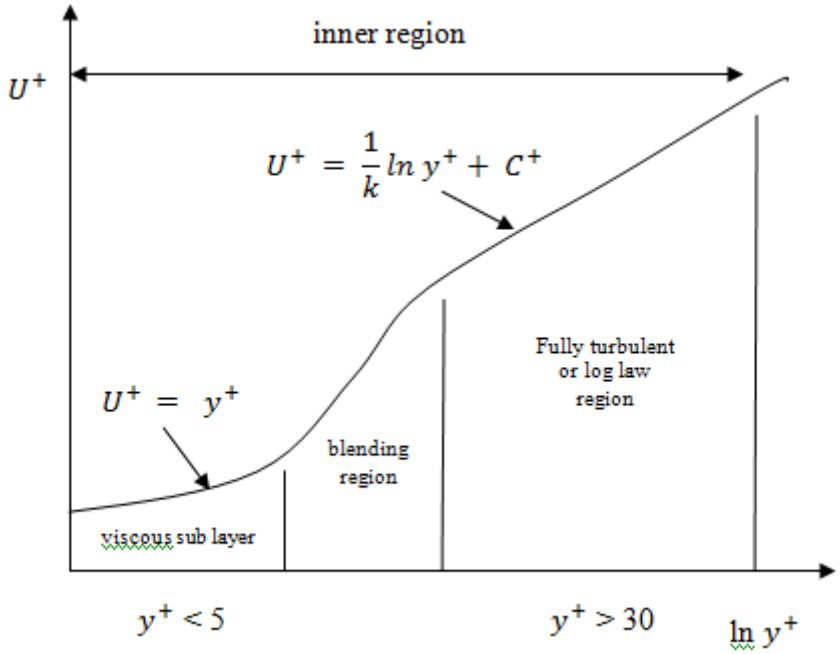

Figure 29 – Log – linear relationships in the inner region of the boundary layer

In CFD y^+ is the non-dimensional distance from the wall to the centroid of the first adjacent grid cells. The accuracy of using each turbulence model in CFD has been shown in many studies to be dependent on the wall y^+ values. A recent study entitled *"Wall y^+ Strategy for Dealing with Wall-bounded Turbulent Flows"* [37] set out to

establish a set of guidelines for selecting the appropriate grid configuration and corresponding turbulence models for modelling wall bounded turbulent flows in FLUENT. It concluded that depending on the choice of wall treatment used, be it near (S-A, k-ω models) or standard (k-ε model) careful consideration must be made over the determination of the first grid point from the wall [37]. Near wall treatment should be applied when the flow characteristics in the viscous sub layer need to be captured [40] e.g. for low Reynolds number flows. The Spalart-Allmaras and k-ω models employ near wall treatment and are designed to be applied throughout the boundary layer. The accuracy of using these models can be increased by ensuring the first grid points from the wall are in the viscous sub layer ($y^+ < 5$), to ensure flow behaviour in this region is captured during the computations [37]. Standard wall functions may be used when there is little variation in the flow resolution until the log law region is reached, e.g. high Reynolds number flows [40]. The k-ε model approximates the log law region coupled with standard wall functions to approximate the viscous sub layer. This was therefore shown to work best when the wall adjacent cells are in the log law region ($y^+ > 30$) [37]. The accuracy of using this model was shown to reduce when the wall adjacent cells were resolved in the viscous sub layer or blending region ($y^+ < 30$), as here the law of the wall becomes invalid [37].

This study highlighted the importance of applying the proper levels of near wall grid refinement when using a particular turbulence model. By doing so, a more accurate solution was proven to be possible. By adopting this method from the outset, computational time and effort may be saved in the re-meshing required to achieve a converged solution using the classical procedure.

2) Grid Adaption Criterion for the Wake of Wind Turbine Airfoil Flows

When modelling the characteristics of wind turbine airfoils using a structured C-grid, special care must be taken when meshing the wake region of the grid. This point was raised and addressed in the recent study conducted at the University of Glasgow entitled “CFD Modelling of Wind Turbine Airfoil Characteristics” [41]. It described the limitations in using a straight cut C-mesh (similar to the mesh generated in stage

2) to model the wake of wind turbine airfoils, stating that this "may introduce unacceptable under-resolution of the wake" [41]. The issue here is that most wind turbine airfoils (particularly those employed at the root) have a non-symmetric profile and a sharp and cambered trailing edge; this results in the lower side becoming concaved [41]. This is particularly synonymous with the Du91-W2-250 airfoil. A consequence of this is a modified wake distribution in comparison to more symmetric airfoils like the NACA 4412 used in the Cornel tutorial. In the paper it was noted that for highly non-symmetric airfoils, the orientation of the wake was synonymous to the airfoil angle of attack [41]. This is in stark contrast to most recommended mesh configurations which refine a region behind the airfoil parallel to the trailing edge in order to capture the flow gradients in the wake. This type of configuration is applied for the base-line mesh in this analysis.

The paper suggests that to improve the wake resolution of a C-mesh used for the CFD analysis of a wind turbine airfoil, any of the following three methods could be adopted:

a) Increase the refinement in the wake region
b) Adapt the geometry of the grid in the wake region to the wake, or
c) A combination of both actions

From a RANS solution, the forces on an airfoil using CFD are determined from the velocity field in the boundary layer and the wake; therefore, the accuracy of computed values should be improved by adapting the resolution of a structured C-mesh in the region of the wake [41].

8.1.2.6 - Step (6)

In order to put these recommendations into practice, a mesh adaption method was developed, which aimed to adapt the base-line meshes to the y^+ and wake resolution criterions. To quantify the impact that varying the near wall and wake resolutions may have on the aerodynamic forces computed with the standard mesh, a simple mesh test was developed. The test was carried out on the Du91-W2-250 airfoil at a Reynolds number of 500,000 for

each of the three selected turbulence models, over a range of increasing angles of attack to test their conformity to the modifications made. During the test, no comparison was made between the performances of each turbulence model.

Grid Adaption Method and Mesh Test

Grid adaption was performed in FLUENT using the adapt function. This allows you to refine or coarsen cells on a predetermined mesh generated in GAMBIT, without having to alter the mesh geometry. Having limited experience with the software, this convenient method was originally adopted in order to save computational time and effort. Using this technique altered the overall number of nodes for the given mesh geometry.

The base-line mesh was first loaded into FLUENT and the solution method was defined. Important details of the solution method are summarised below.

- Pressure based solver, steady formulation
- Absolute criteria for residuals set to 0.0001
- Pressure velocity coupling set to SIMPLE
- Discretization methods:
    - Pressure set to PRESTO
    - Momentum set to Second Order Upwind
    - Turbulent Viscosity set to Second Order Upwind

The velocity inlet boundary conditions were defined for each simulation from on the Reynolds number and the angle of attack, which ranged from -3 to 18 degrees at 3 degree incriminations. In the Reynolds number formulation, the density of air was taken as 1.225 kg/m^3 and the freestream dynamic viscosity was taken as 1.7895e-05 $/ms$. Simulations were then run for a maximum of 2000 iterations until the solutions converged. The computed aerodynamic forces could then be converted to lift and drag coefficients using the conversion described in *Section 3.22.*

Using the Yplus adapt function, the original grid was then adapted to the y^+ criterion which is reinstated as:

- Spalart-Allmaras and SST k-ω ($y^+ < 5$)
- k-ε ($30 < y^+ < 300$)
  *note for k-ε $y^+ < 300$ to avoid applying the log law in the outer region where it becomes invalid [37]

To illustrate this process, Figure [30] displays the original mesh, and the adapted mesh at the airfoil leading edge, for a simulation set up using the Spalart-Allmaras model.

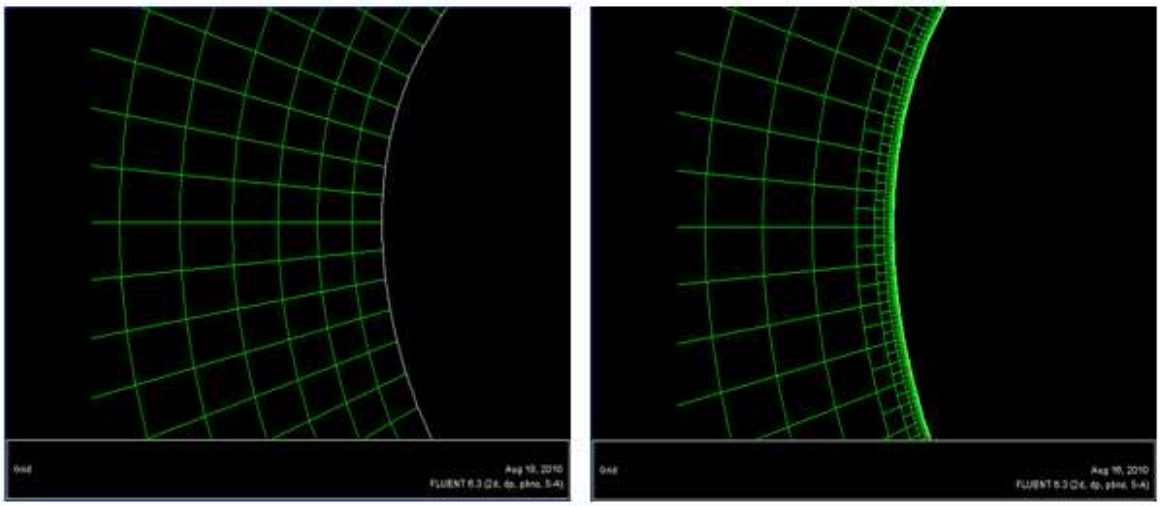

Figure 30 – Original mesh (left) and adapted to y+ criterion mesh (right)

Here we can see cells added close to the airfoil surface at the leading edge, chosen for illustrative purposes. Additional cells would have been added over the entire airfoil surface. For the Spalart-Allmaras model it is desirable to have cells in the viscous sub layer, hence the strong refinement in this region. This process was performed on the original cases and new simulations were run over the same range of AoA to quantify the impact on the computed aerodynamic forces

To determine the behaviour of the wake and a method for adapting the grid to the wake region, contour plots of turbulent viscosity were analysed at each AoA. Figure [31] shows two contour plots of the airfoil at 6 and 12 degrees for illustrative purposes. Here it can be

observed that the wake does not lie in the refined region behind the airfoil but at an angle, similar to that of the AoA, within a region of coarse and low resolution cells. In this configuration, the resolution of the cells in the wake may not be high enough to capture the high gradients within this turbulent region of the flow, rendering the solution inaccurate. To remedy this, the Iso-value adapt function in FLUENT was employed to refine the cells in the region of the wake. This allows you to adapt cells within or outwith a selected range of values, in this case, Iso-values of modified turbulent viscosity ($m2/s$) were employed. In Figure [31], the red area shows the selected cells for adaption for the two chosen AoA. It can be seen that these match the region of the wakes shown in Figure [30]. The grid could then be adapted producing the meshes shown in Figure [32]. The grids previously adapted to the y^+criterion were each adapted using this method and the mesh test was reproduced to quantify its impact on the computed aerodynamic forces.

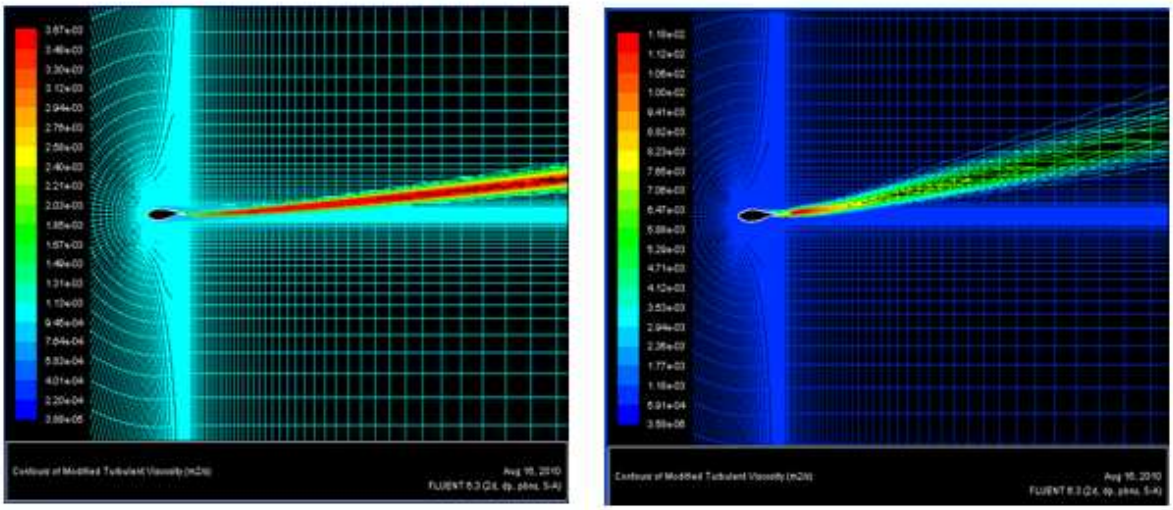

Figure 31 – Contour plots of turbulent viscosity at α = 6° (left) and 12° (right)

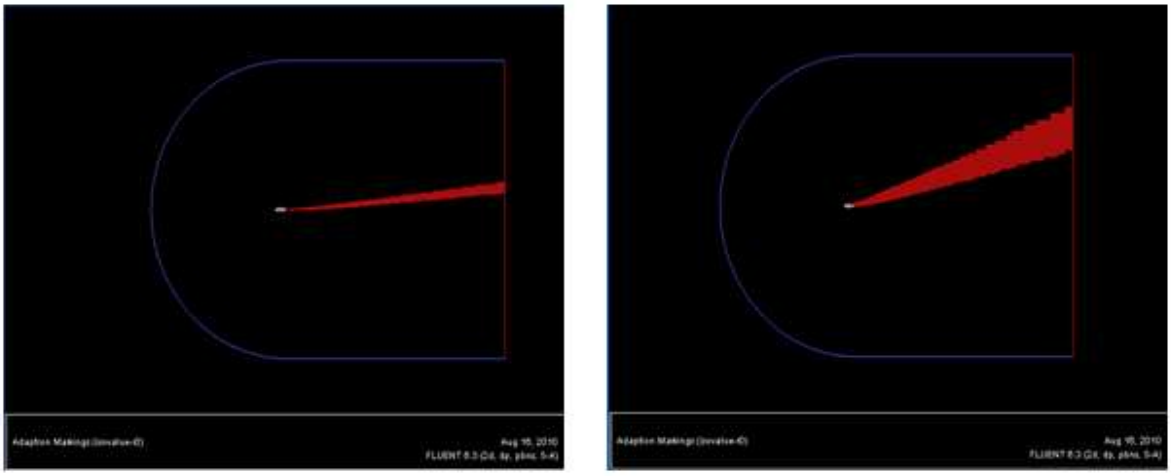

Figure 31 – Selected cells for refinement using Iso values of modified turbulent viscosity technique

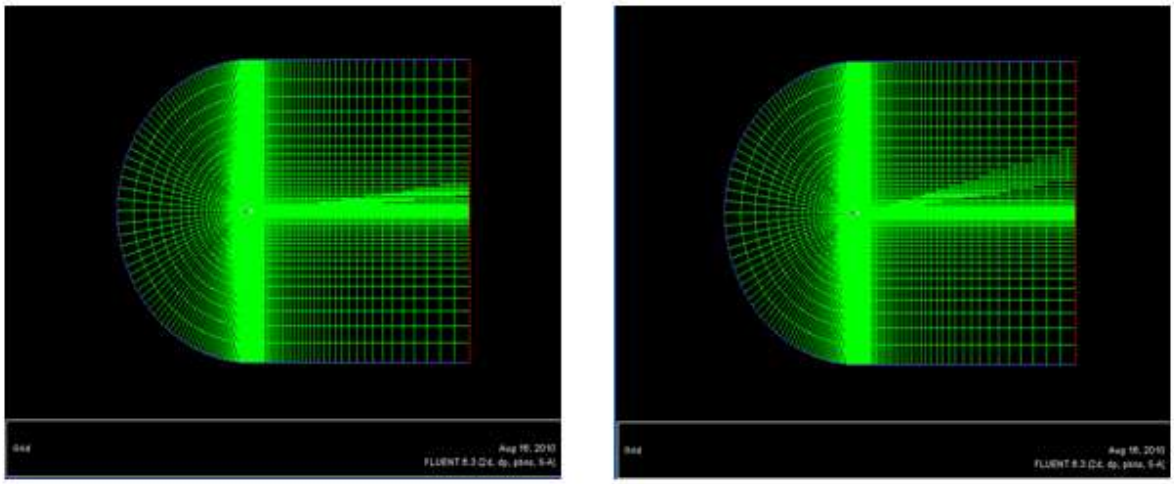

Figure 32 – Wake adapted grids at α = 6° and 12°

8.1.2.7 - Step (7)

An analysis of the results from the grid adaption and mesh test was then performed to establish the best practice for performing large scale simulations over a wider range of AoA, and at other Reynolds numbers for both the Du91-W2-250 and NACA-64418 airfoils. The results from the test are presented in *Chapter 9 – Results and Discussion.* From this analysis, it was confirmed that by adapting the mesh to the y^+ criterion and in the region of the wake, accuracy could be improved; therefore, this method was adopted for the next stage of simulations.

8.1.2.8 - Step (8)

One issue which became evident when running the simulations for the mesh test was the time it took to set up each solution in FLUENT when a new AoA was to be analysed. This required user inputs to redefine the velocity inlet conditions and reinitialise the flow. The next stage of the process involved producing simulations over a wider range of AoA, at more Reynolds numbers and for both airfoils. This data was required to reproduce the experimental polars of the two airfoils, ranging from -14 to 30 degrees. Having to physically input the new boundary conditions at each alpha increment, proposed a large issue in terms of the computational time and effort it would require to run these simulations.

One benefit of FLUENT is that it has a text user interface (TUI) which allows scripts, or journal files to be run through it, negating the need for human inputs to the GUI. By generating a script, a full set of simulations can be set up in FLUENT, initialised and run without having to physically re-set the boundary conditions, initialise the flow and re-run the simulation each time a new AoA is analysed. This method was adopted, and a script was produced which mirrored the inputs used in the mesh test to set up the solution and adapt the grid. In order to simulate a range of AoA, a Matlab code was produced to generate a script which ran simulations for a user inputted AoA range and Reynolds number, and outputted the airfoil characteristics (forces, moments, pressure distributions) to a file after each run. The code is displayed in *Appendix 3*.

The benefits of having this tool were unprecedented. The main benefit being the time and effort saved in running multiple simulations. A full set of simulations could be run over night, with the airfoil characteristics at each AoA outputted to a desired location for analysis the next day.

8.1.2.9 - Step (9)

With a method set up for grid adaption and performing simulations, the next stage compared the performance of the three selected turbulence models for modelling airfoil characteristics. A full set of polars was produced for each airfoil at two Reynolds numbers and compared against those produced by experiment, XFLR5 and RFOIL. Pressure distributions were generated over the AoA range and at the Reynolds numbers given in the experimental data. A full analysis is presented in *Section 9- Results and Discussion.*

8.1.2.10 Step (10)

The performance of the three turbulence models was varied and although distinct improvements were made using the grid adaption techniques, discrepancies remained between the CFD computations and the experimental data. One potential cause of concern was the large discontinuous variations in cell size between the wake adapted region and the freestream region of the mesh. This is highlighted below in Figure [33].

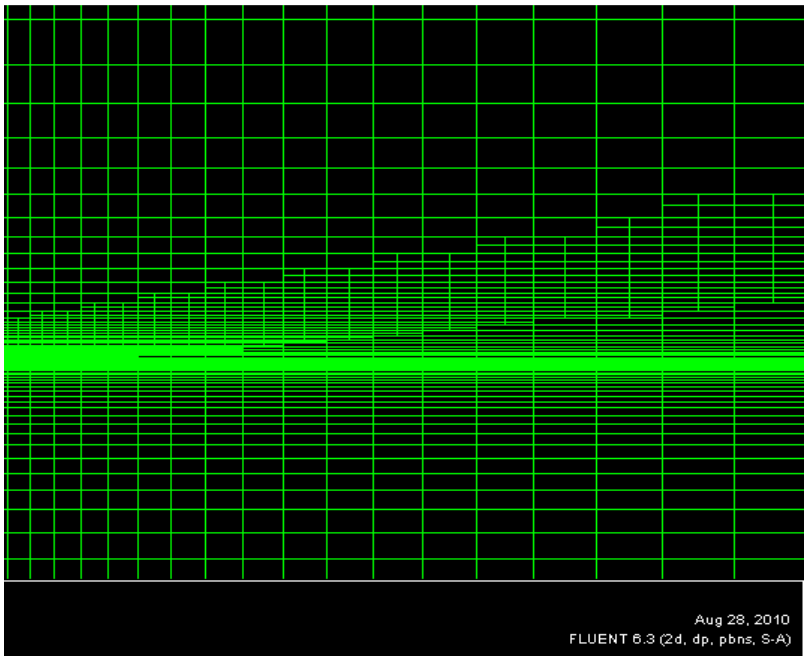

Figure 33 – Grid plot highlighting discontinuities in cell size within wake adapted region

Large discontinuous variations in cell size can destabilise a solution and reduce its accuracy and hence, is an unfavourable outcome when generating meshes. To remedy this, and to potentially capture more detailed flow behaviour, a refined mesh was generated. The original coarse mesh with 18,183 nodes was redefined and increased to 404,736 nodes, with particular refinement made within the wall bounded and wake regions of the flow. With the knowledge of how the wake behaves with respect to AoA, the mesh geometry was specifically defined to increase the resolution in this region. Figure [34] shows an example of the new refined mesh at $\alpha = 5^{o}$.

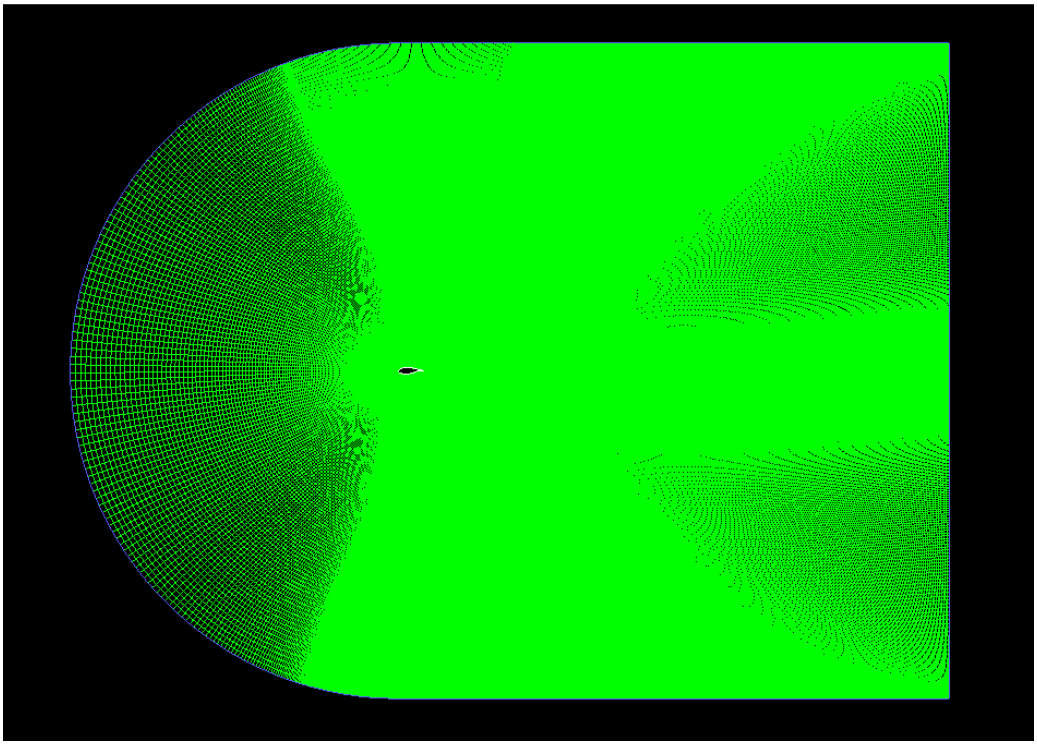

Figure 34 – Refined mesh at $\alpha = 6°$

In comparison to the original coarse mesh, the new mesh is visibly more refined, with the average cell size considerably smaller. The resolution within the region of the wake and airfoil surface is particularly high in an attempt to better capture the changing gradients of the flow properties. The cell size changes between the wake and the freestream region are more smooth and continuous; alleviating the old issues had with the original grid adapted mesh.

The time taken to generate a mesh of this size was quite considerable. As the inclination of the wake varies with AoA, a separate mesh is required for each chosen interval. Lift and drag data at AoA's ranging from -14:2:30º is the minimum required to justify their use in BEM; therefore, requiring in the region of 20 separate mesh files. To do these individually would take a considerable amount of computational time and effort. Like FLUENT, GAMBIT has a TUI which allows you to run script files through it, negating the need for human inputs into the GUI. The benefit being that once a script is written; it can be modified and reused to generate other mesh files.

To reduce computational time and effort, a script was generated which created the refined meshes in GAMBIT for a user specified AoA range. With the assistance of Tom McCombes, a Matlab code was written which repeatedly redefined the geometry of the wake affected region, whilst holding the remaining mesh geometry constant. This tool was used to create a script which could be run through GAMBIT in one sitting to generate and store multiple mesh files of a varying geometry. These files could then be called in the script used for initialising simulations in FLUENT to define the airfoil characteristics at each AoA. Figure [35] displays examples of meshes created at their respective AoA.

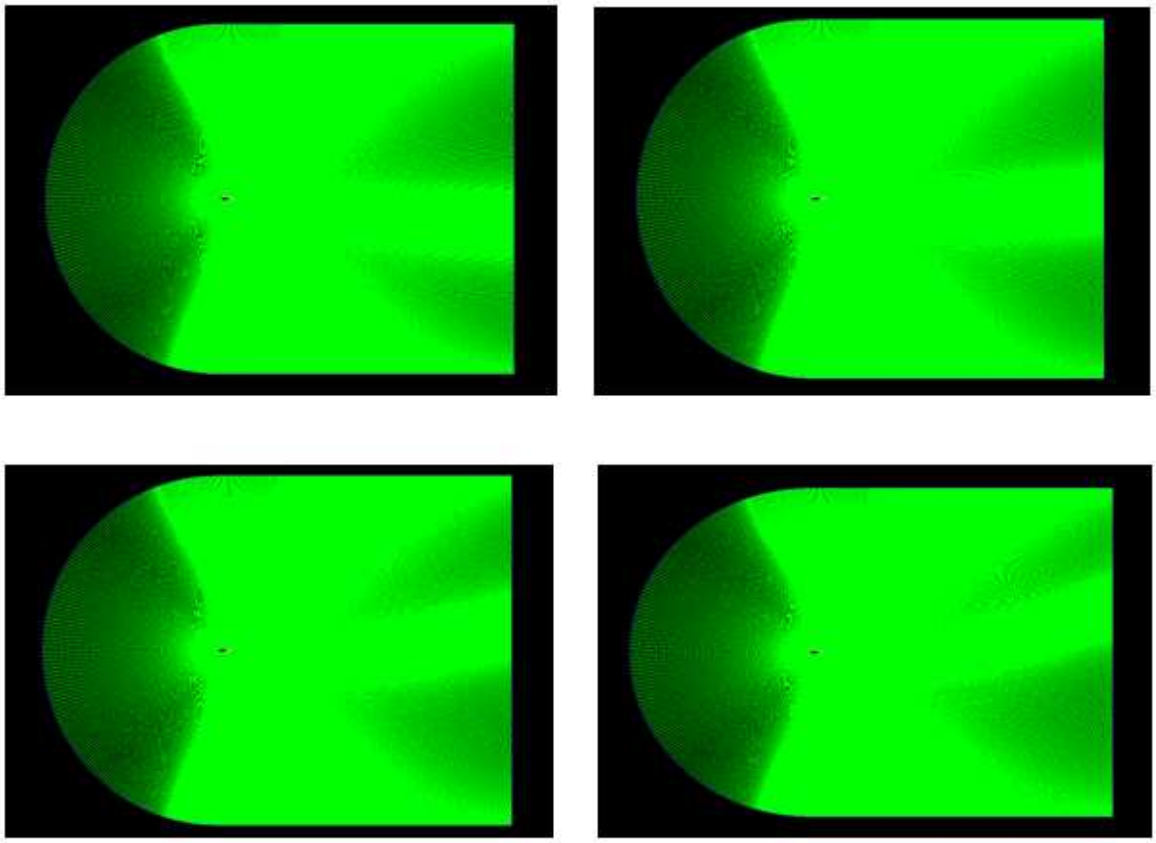

Figure 35 – Meshes at α = -5°, 5°, 10° and 15° highlighting movement of the wake region (top left to bottom right)

The intention was to run these meshes through FLUENT with the three turbulence models and witness the impact of using a more refined mesh on the produced airfoil characteristics. Running a full set of simulations with such a refined set of meshes ended up taking over three days. After the first set of simulations, the following analysis highlighted some severe discontinuity within the results, and an error was spotted in the simulation set up. This meant redefining the solution method and carrying out further simulations. Unfortunately, as this method was not adopted until the latter stages of the project, time and resources became unavailable to achieve a full set of airfoil characteristics using the refined mesh.

Consequently there is no inclusion of any results or discussion from using this method within this report.

8.2 – Methodology – BEM analysis

The experimental and computed lift and drag data were exported from EXCEL and placed into a matrix within the BEM code, as illustrated in Figure [36]. Plots of power and thrust coefficient versus tip speed ratio were developed for a selected set of computed results and compared to those produced by experiment.

```
%data(:,2) = data(:,2)  - data(end,2);

Rt = max(data(:,1));      %   Tip radius
Rh = min(data(:,1));      %   Root radius
BEradius = repmat(linspace(Rh,Rt,nr),NS,1);

theta = deg2rad(th0 + interp1(data(:,1),data(:,2),BEradius,'cubic','extrap'));
chord = interp1(data(:,1),data(:,3),BEradius,'cubic','extrap');
sigma = N.*chord./(2*pi.*BEradius);

%%  Inputs: Foil Data

clcd = [-32.25  -0.802  0.64090
-31.25  -0.761  0.59723
-30.25  -0.726  0.55935
-29.26  -0.689  0.52291
-28.26  -0.641  0.48115
-27.26  -0.589  0.43947
-25.26  -0.511  0.37711
-23.26  -0.501  0.34593
-21.25  -0.449  0.27766
-20.79  -0.962  0.12981
-20.29  -0.952  0.12478
-19.29  -0.962  0.11236
-18.29  -0.956  0.09763
```

Figure 36 – Location of the airfoil lift and drag coefficients in the BEM code

The turbine geometry chosen for this analysis was based on the model turbine developed for the NREL Unsteady Aerodynamics Experiment (UAE), which is documented in reference [42]. It would have been desirable to use the geometry of the Mexico model, yet information regarding the twist distribution of the blades was unavailable.

The NREL model was a 10m diameter horizontal-axis research wind turbine, tested in a wind tunnel similar to that of the Mexico project. One of the aims of the Mexico project was to supplement the work previously done by NREL; the Du91-W2-250 airfoil is very similar to the S809 used by NREL on the UAE model. For these reason, the UAE model geometry was used in this analysis.

Chapter 9

Results and Discussion

In this chapter the most significant results from the project are presented and discussed. For the 2D analysis of the airfoil characteristics, results are presented in graphical form and in tabular form for a selected range of values. Contour plots of velocity magnitude are also included to help describe the behaviour of the flow and its impact on the computed lift and drag coefficients.

9.1 – 2D Airfoil Analysis

9.1.1 – Mesh – Test

The results of the test applied to determine the impact of adapting the base line mesh, generated for use in the CFD solver FLUENT, to the recommendations made within the review of literature in *Section 8.1.2* are displayed and discussed in this section. Computed results are displayed for the Du91-W2-250 airfoil at Re = 500,000 using the Spalart-Allmaras turbulence model as the viscous solver in FLUENT.

9.1.1.1 – Results

Table [3] displays a comparison between the computed and experimental lift and drag coefficients over a range of angles of attack using the base line mesh. A % error is also calculated to determine the deviation from experiment using the CFD solver. Table [4] displays the same results set for the base line mesh adapted to the y+ criterion. Table [5] displays the results set for the base line mesh adapted to both the y+ and the wake resolution criterions. Figure [37] displays the experimental and computed lift and drag polars to highlight the impact on performance of using each mesh configuration. Mesh 1 is the base line, Mesh 2 is the base line adapted to the y+ criterion and Mesh 3 is the base line adapted to both the y+ and wake resolution criterions.

Alpha (°)	Cl	Exp	% error	Cd	Exp	% error
-3	0.045	-0.0224	49.66	0.027	0.0073	72.39
0	0.409	0.346	15.44	0.023	0.0047	79.20
3	0.756	0.711	5.93	0.024	0.0106	55.40
6	1.048	1.033	1.49	0.029	0.0095	67.16
9	1.244	1.391	11.78	0.042	0.0173	58.61
12	1.276	1.416	10.96	0.086	0.0234	72.65
15	1.136	1.278	12.42	1.331	0.0884	33.55
18	1.103`	1.200	8.78	0.199	0.1246	37.34

Table 3 – Experimental and computed lift and drag coefficients – Base line mesh

Alpha (°)	Cl	Exp	% error	Cd	Exp	% error
-3	0.045	-0.0224	54.28	0.021	0.0073	65.51
0	0.404	0.346	14.44	0.020	0.0047	76.75
3	0.734	0.711	3.036	0.022	0.0106	51.65
6	1.0329	1.033	0.02	0.026	0.0095	63.51
9	1.280	1.391	8.64	0.034	0.0173	48.97
12	1.462	1.416	3.10	0.057	0.0234	58.97
15	1.499	1.278	14.75	0.103	0.0884	13.94
18	1.395	1.200	13.97	0.144	0.1246	13.53

Table 4 – Experimental and computed lift and drag coefficients – y+ adapted mesh

Alpha (°)	Cl	Exp	% error	Cd	Exp	% error
-3	0.049	-0.0224	54.29	0.022	0.0073	65.94
0	0.411	0.346	15.89	0.020	0.0047	76.02
3	0.742	0.711	4.10	0.021	0.0106	49.75
6	1.068	1.033	3.27	0.025	0.0095	61.79
9	1.271	1.391	7.22	0.034	0.0173	49.63
12	1.460	1.416	2.99	0.048	0.0234	51.21
15	1.376	1.278	7.15	0.086	0.0884	2.59
18	1.301	1.200	7.75	0.125	0.1246	5.97

Table 5 – Experimental and computed lift and drag coefficients – y+ & wake adapted mesh

9.1.1.2 - Discussion

Using Mesh 1, the errors in the computed drag values were considerably larger than those computed for lift, as shown in Table [3]. The maximum error in cl was half of the minimum error in cd; errors in drag coefficient ranged from 33.5 – 79.2% whilst errors in lift coefficient only ranged from 1.5 – 15.3 % (with the exception of an error of 50% in the prediction of the cl at $\alpha = 3°$). In the prediction of cd, the deviations from the experimental values were largest during the lift curve slope and those at stall between values of $\alpha = -3$ and 12°. The errors reduced by around half during the post stall regime at AoA above $\alpha = 12°$. Within the predicted values of cl, in some cases, the errors within the post stall regime were around 10% higher than those predicted during the lift curve slope. Despite a recovery at $\alpha = 18°$, in general the CFD solver was more apt at predicting the lift curve slope than the stall and post stall regime using Mesh 1. This can be seen in Figure [37] below.

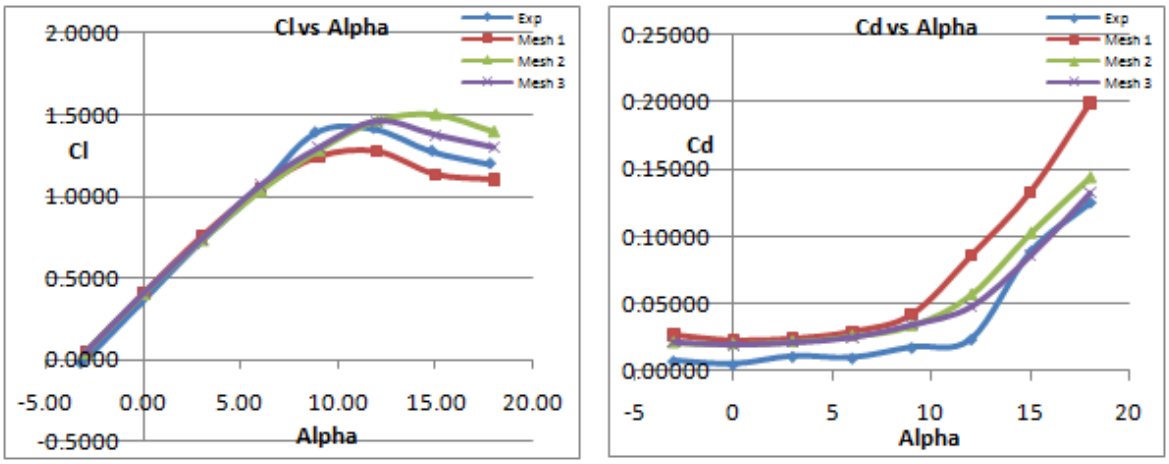

Figure 37 – Mesh test lift and drag polars

Comparing the results of Mesh 2 in Table [4] to Mesh 1, across the entire range of values there is an improvement in the prediction of cd; particularly during the post stall regime were the error has reduced by half. The prediction of cl in general has improved, particularly around stall ($\alpha \approx 11°$); however, at $\alpha = 15°$ and above the error has in fact increased when moving from Mesh 1 to the refined Mesh 2. Figure [37] clearly displays the vast improvement in the prediction of cd in the stall and post stall regime when adopting Mesh 2

over Mesh 1. In fact, the prediction of cd over this range has become more accurate than the prediction of cl, which is in stark contrast to the trend seen in the results for Mesh 1. Figure [37] highlights this showing that although the prediction of cl has improved in the lead up to stall, the performance of the solver has declined during the post stall regime. However, in general it can be still said that the solver exhibits vast improved characteristics when predicting cl over cd

Now comparing the results of Mesh 3 in Table [5] to Mesh 2 and Mesh 1, again there is an improvement in the prediction of cd across the range of values. The improvement is again most pronounced during the post stall regime. This is highlighted in Figure [37] where the computed results using Mesh 3 correlate extremely well with the experimental data over this range of values. The prediction of cl has improved during the stall and post stall regimes, yet there is a slight decrease in performance during some values within the lift curve slope. Despite these deviations, Figure [37] shows how improved the correlation with the experimental data becomes when using Mesh 3 over Meshes 2 and 1.

9.1.1.3 - Analysis

The results from the Mesh Test provide conclusive evidence to show, that by adhering to the two applied mesh adaption techniques, an improvement in the accuracy of the calculated lift and drag coefficients can be achieved when using a CFD solver.

By adapting the base line mesh (Mesh 1) to the y+ criterion to create Mesh 2, a distinct improvement was made in the calculation of cl. This was more pronounced within the lead up to stall and around stall in comparison to the lift curve slope. The y+ criterion is used to refine cells in the viscous sub layer, where the flow characteristics are largely influenced by viscous effects. During the lift curve slope, the flow is almost entirely inviscid therefore refinement in this area has less of an impact on the results; however, improvements in computed values were observed which may be attributed to the increased resolution of the cells providing a more accurate representation of the flow. In contrast, at higher AoA where the airfoil approaches stall, the effects of viscosity become more pronounced and are the main contributors to flow separation. Flow separation creates a modified lift distribution which is the main contributor to the generation of lift. By refining the cells in the viscous sub

layer, the impact of these viscous effects on the calculated lift force could be better resolved within the solution. The calculation of cd was shown to improve across the entire range of values when using Mesh 2. The drag force on an airfoil is influenced by both skin friction effects and flow separation therefore viscosity will have more of an impact on its magnitude. Adapting to the y+ criterion is particularly beneficial for the prediction of drag. In the post stall regime where viscous effects become increasingly pronounced the prediction of cd was shown to dramatically improve using the y+ adapted mesh.

Refining cells in the region of the wake within the mesh adapted to the y+ criterion provided further improvements in the accuracy of the computed lift and drag coefficients. The turbulent wake downstream from an airfoil significantly reduces lift. By increasing the resolution of the cells in the wake, the calculation of cl reduced further towards its experimental value at high AoA where the impact of the wake becomes more pronounced. The large region of turbulent, recirculating flow created by the wake also increases the pressure drag experienced by an airfoil, influencing the magnitude of the total drag force. The calculated values of cl were again improved by adapting to the wake criterion, providing further evidence to warrant the application of this technique. As will be seen in some of the following contour plots, the wake region within the proximity of an airfoils surface becomes larger as the AoA increases; this may account for the considerable improvement in computed cd values during the post stall regime.

The mesh test was carried for both the k-ε and SST k-ω turbulence models to check their conformity to the trends observed in the above results. Similar behaviour was recorded and as a result the mesh adapted to both the y+ and wake resolution criterions was chosen as the new base line mesh for any further simulations using CFD.

9.1.2 – Du91-W2-250

9.1.2.1 - Results

The computed results for the Du91-W2-250 airfoil are presented in this section and compared to those acquired via experiment. Figures [4.1, to 4.6] in *Appendix 4* display the lift, drag and moment polars from the experimental data and the corresponding computed results using the two airfoil analysis and design codes and the three turbulence models used in FLUENT. Table [6] displays a select number of lift and drag coefficients in tabular form taken from the results set at Re = 500,000.

Alpha (°)		Cl							Cd					
		EXP	XFLR5	RFOIL	S-A	k-w	k-e		EXP	XFLR5	RFOIL	S-A	k-w	k-e
0		0.346	0.423	0.388	0.365	0.361	0.323		0.0047	0.0122	0.0118	0.0203	0.0468	0.0872
7		1.156	1.227	1.097	1.151	1.149	0.897		0.0116	0.0149	0.0142	0.0298	0.0701	0.1355
11		1.492	1.435	1.236	1.465	1.428	1.117		0.0175	0.0252	0.0276	0.0443	0.0823	0.1711
18		1.197	1.337	0.977	1.358	1.150	1.289		0.1413	0.1131	0.1240	0.1326	0.1843	0.2841

Table 6 – Experimental and computed lift and drag coefficients – Du91-W2-250 (Re = 500,000)

9.1.2.2 – Discussion

Considering first Re = 500,000: on first inspection of the lift polars in Figure [4.1], *Appendix 4*, the two airfoil design and analysis design codes, XFLR5 and RFOIL both predict the lift curve slope ($\alpha = -12°$ to 10°) reasonably well. However, in the lead up to stall, values predicted by RFOIL begin to deviate away from the experimental data leading to an under prediction of $cl\ max$. Experimentally, $cl\ max = 1.494$ recorded at $\alpha = 10.81°$. Although RFOIL under predicted $cl\ max$ it did predict its occurrence fairly well, estimating $cl\ max$ to be 1.289 at $\alpha = 10°$. XFLR5 exhibited better pre stall and stall characteristics, estimating $cl\ max = 1.454$ at $\alpha = 10°$. Post stall behaviour in the lift coefficient was at first very well predicted by XFLR5. An example of which is shown in Table [6] where the error in the computed value at $\alpha = 11°$ is only 3%; however, above $\alpha = 13°$, XFLR5 tended to over predict experimental values with predominant errors of $\approx 12\%$ in the data, as shown at $\alpha = 18°$ in Table [6]. The post stall regime was in general under estimated by RFOIL.

Of the three turbulence models tested in FLUENT, the S-A and SST k-ω models produced the best agreement with the experimental data over the full lift polar at Re = 500,000. The gradient of the lift curve slope was fairly well predicted with both of these models, matching that of RFOIL (with exception to a few results at $\alpha < -8°$). In a similar fashion to RFOIL, the two models began to under predict cl in the lead up to stall, more so in the SST k-ω model; however, the deviation from experiment only resulted in a modified curve shape with the calculation of the magnitude of $cl\ max$ well executed. The S-A model estimated $cl\ max = 1.495°$ and the SST k-ω predicted $cl\ max = 1.458°$. As a result of the modified curve shape the occurrence of $cl\ max$ was delayed in both cases to $\alpha = 12°$.The modelling of the post stall regime using the two models was initially of a similar standard to that of XFLR5 and an improvement on RFOIL. At $\alpha > 20°$ both models exhibited improved performance over that of XFLR5. The worst performing computational method was the k-ε model used in FLUENT. The gradient of the lift curve slope was too shallow leading to an under prediction of $cl\ max$ and an over prediction of its occurrence, with $cl\ max = 1.33$ at $\alpha = 22°$.

Looking at the drag polars in Figure [4.2] *Appendix 4*, again at Re = 500,000, of the five computational methods analysed, the computed data from XFLR5 and RFOIL during the pre

stall regime ($\alpha = -12°$ to 10°) correlates best with the experimental data. There are marginal differences between the performances of the two, as can be seen at $\alpha = 0°$ and 7° in Table [6]. The best performing turbulence model in FLUENT during the pre stall regime was the S-A model, with the k-ε providing the poorest correlation with the experimental data. At stall, the two airfoil design and analysis codes continue to produce the most accurate predictions of cd, with the previous trend continuing in the performance of the three turbulence models. In the latter stages of the post stall regime, between $\alpha = 14°$ and 30°, XFLR5 and RFOIL under predict the experimental data, and their performances begin to deteriorate. In this regime, the S-A model provides the closets correlation to the experimental data, mapping the sharp changes in the gradients of the curve fairly well. The SST k-ω model over predicts the gradient of the curve after $\alpha = 17°$, leading to highly over estimated values of cd.

The moment polars in Figure [4.3] *Appendix 4* show a fairly good correlation between the experimental data and those produced by XFLR5 and RFOIL, with XFLR5 providing the closest match of the two. In stark contrast, the polars produced by the three turbulence models are considerably inaccurate and do not resemble those of a common moment curve for an airfoil.

Now considering the same results set at Re = 1,000,000: observing the lift curve slopes in Figure [4.4] *Appendix 4,* XFLR5 continues to provide the best estimate of the lift curve slope out of the five computational methods. The performance of XFLR5 in general is very good, providing a good estimate of the value of $cl\ max$ and the AoA at which it occurs. Experimentally, $cl\ max = 1.408$ recorded at $\alpha = 9.33°$. XFLR5 predicts $cl\ max$ with an error of only 0.28% to be 1.412 at $\alpha = 10°$. However, its prediction of the post stall regime is too gentle in comparison to experimental data, where at first a steep negative gradient is witnessed after stall. The performance of RFOIL is much the same with fairly good correlation to the lift curve slope, yet still an under estimation of cl values in the lead up to stall, stall and the post stall regime; however, the errors in these values are reduced at the higher Reynolds number. Unfortunately, experimental data beyond $\alpha = 22°$ was unavailable, but looking at the trend of the graph, it appears that RFOIL may of under predicted the latter stages of the post stall regime by not that much in comparison to the other models. Again, out of the three turbulence models analysed, the S-A and SST k-α models in general provided the best estimation of the lift curve slope, with the S-A model providing the most accurate

representation of the lead up to stall. However, at low AoA ($\alpha < 6°$) errors in cl were highest in the predictions made by the S-A model. Both models again reasonably predict the value of $cl\ max$ but in a similar fashion to before, they over predict the angle at which it occurs. The post stall regime is not as well mapped by both models in comparison to the curves at the lower Reynolds number. The SST k-ω model encountered convergence issues at high AoA when running simulations, producing extreme irregularities in the results. Consequently, these results were omitted from the analysis. The poorest representation of the experimental data is again provided by the k-ε model used in FLUENT, with a similar under estimate of the gradient of the lift curve slope and a considerable over estimate of $cl\ max$ and the angle at which it occurs.

The behaviour witnessed within the drag polars in Figure [4.5], *Appendix 4* is similar to that witnessed at the lower Reynolds number. XFLR5 and RFOIL continue to provide the best estimate of cd prior to stall with the S-A model producing the closest correlation, and the k-ε providing the poorest out of the three turbulence models analysed in FLUENT. The deviations from the experimental data using FLUENT may seem more extreme at the higher Reynolds number but this is due to the smaller scale used on the graph. The post stall behaviour is much the same with the S-A model providing the closest estimates. It can be seen in this graph that RFOIL actually exhibits better performance in the early stages of the post stall regime compared to XFLR5. This trend is likely to of continued if more experimental data was available for comparison.

In Figure [4.6], *Appendix 4* the moment curve is fairly well predicted again by the two airfoil design and analysis codes, with XFLR5 providing the closest correlation. The curves predicted by FLUENT are yet again significantly unrepresentative of their experimental counterpart.

9.1.2.2 – Analysis

To help describe the underlying reasons behind the behaviour of the polars produced for the Du91-W2-250 by computational methods; Figure [38] displays pressure distributions at AoA intervals representative of those chosen for the tabulated data in Table [6]. These are for a Reynolds number of 500,000 in order to make direct comparisons to those provided by

experiment in Figure [39]. This should especially provide a good insight into the discrepancies in the lift polars as the lift force is almost entirely defined by the pressure distribution. Contour plots of velocity magnitude at these incident values are also included to analyse the differences between the solutions provided by three turbulence models used in the CFD solver, FLUENT.

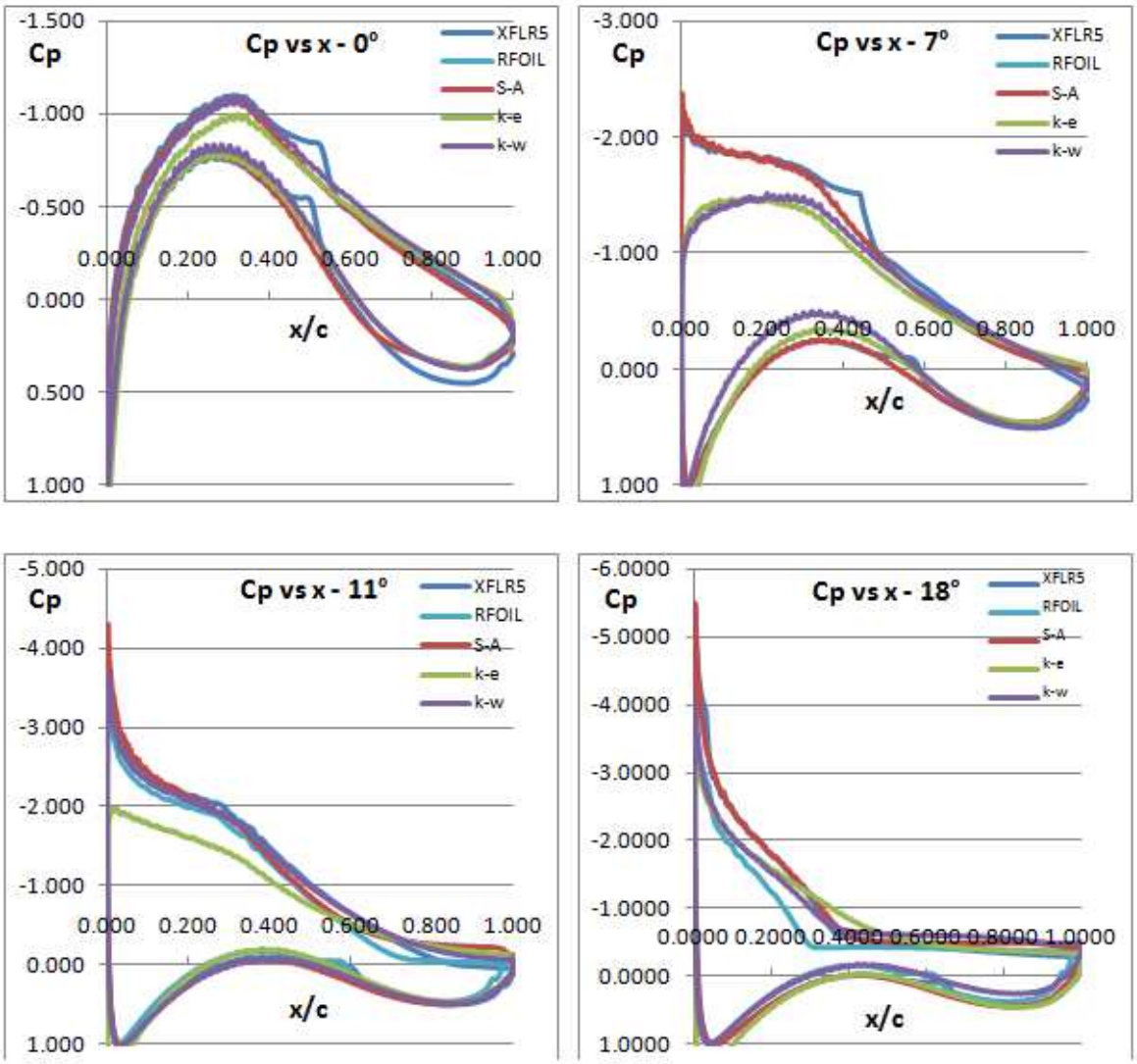

Figure 38 – Computed Du91-W2-250 pressure distributions (Re = 500,000)

For Re = 500,000, XFLR5 was shown to predict the lift curve slope and corresponding values of drag very well. It also made a reasonable estimate of the magnitude and occurrence of $cl\ max$. In the post stall regime, the errors in the predicted values of cl and cd were at first small before increasing at

higher AoA, where the code overestimated cl values and underestimated cd values, deduced via experiment. Looking at the pressure distributions predicted by XFLR5, they are almost identical to those predicted by RFOIL during the lift curve slope at $\alpha = 0°$ and 7°. RFOIL was also shown to provide a good estimate of the lift curve slope. They also match those deduced by experiment fairly well, giving explanation to the well predicted cl values during this inviscid regime. At $\alpha = 0°$, the magnitude of the maximum suction pressure ($-Cpmax$), and the occurrence of mild transition on both the upper and lower surfaces, and its location along the chord, are relatively well predicted by XFLR5 and RFOIL. At $\alpha = 7°$, $-Cpmax$ is again well predicted; however, the location of the transition points are delayed in comparison to that predicted by experiment. The subsequent adverse pressure gradients are also stronger than their experimental counterpart, yet the flow remains attached, recovering to above ambient pressure at the trailing edge. As a result, the predictions of cd are not affected, matching that of experiment very well.

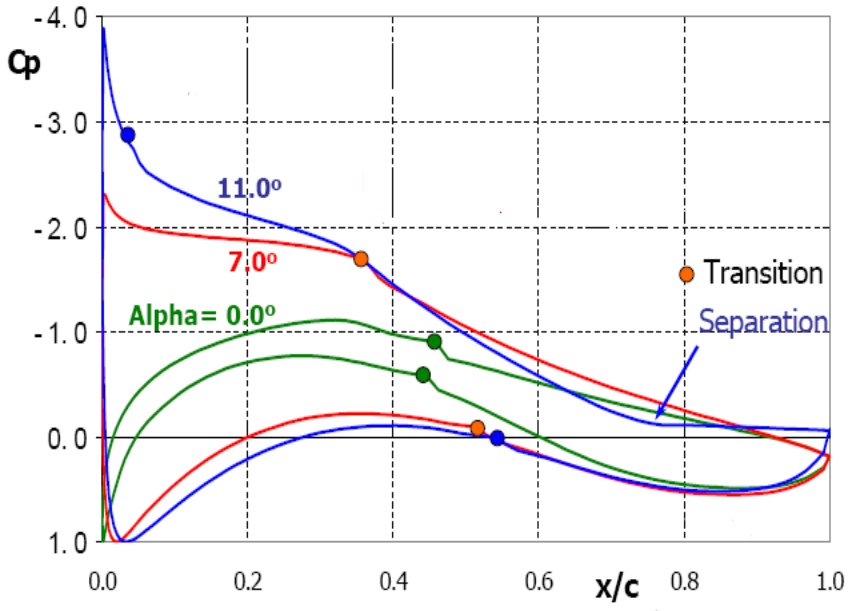

Figure 39 – Pressure distributions - Du91-W2-250 (Re =500,000)

At $\alpha = 11°$, the flow becomes separated at $x/c \approx 0.75$ in the experimental data. This is well predicted by XFLR5, after a good estimate of $-Cpmax$, the transition point and the severity of the subsequent adverse pressure gradients. As a result, the performance of XFLR5 in predicting the values of cl in stall and the post stall regime is very good. As drag is heavily influenced by viscous flow and the

increased pressure drag created by the turbulent separated wake, the accurate prediction of the separated region also contributes to a good prediction of cd. Consequently, the occurrence and magnitude of the nose down pitching moment at stall is well estimated as a result of a good prediction of both the lift and drag forces present on the airfoil. RFOIL however, under predicts $cl\ max$ and the post stall regime. Looking at the pressure distribution at $\alpha = 11°$, the flow appears to be more developed towards a fully turbulent regime in comparison to that portrayed in the experimental data. $-Cpmax$ is under predicted and the adverse pressure gradients following transition are more severe. As a result, around 5% more of the flow over upper surface appears to be separated. This premature development of the flow may explain the under prediction of cl values during and after stall, as the flow was estimated to break from the inviscid regime too early.

Unfortunately, no experimental data was available for a pressure distribution at $\alpha = 18°$. However, looking at the pressure distributions in Figure [38] at this AoA, they highlight how more advanced the results produced by RFOIL are towards a fully stalled state than those produced by XFLR5. The flat bar of pressure, indicating the separated region is around 10% larger, indicating a larger region of turbulent recirculating flow. Looking at the tabulated results, RFOIL actually exhibits better performance characteristics at this AoA than XFLR5. It may be that the actual flow suddenly developed faster towards a fully stalled state, after an initial slow development, which was at first predicted well by XFLR5, however was mapped poorly at higher AoA which lead to over predictions of cl.

Comparing the results of the three turbulence models used in the CFD solver FLUENT, the S-A model and SST k-ω produced the best estimate of the lift curve slope, on a par with that of RFOIL. The k-ε model produced the poorest correlation. Looking at the pressure distributions at $\alpha = 0°$, the S-A and SST k- ω models both predict the magnitude and the occurrence of $-Cpmax$. The shape of the pressure distributions is not too dissimilar to experiment; therefore the state of the flow has been modelled quite well. The plot from the k-ε model under predicts $-Cpmax$, suggesting that the flow is lagged in comparison to the experimental data, highlighting a possible reason behind the under prediction of the lift curve slope. The model also predicts Cp to be > 1 at the leading edge, which is highly inaccurate as a value of 1 should be present here to indicate a stagnation point and the location of the maximum static pressure. This may also contribute to an inaccurate solution. It is not evident if the transition points on upper and lower surfaces have been identified by either of the models. On close inspection of the contour plots in Figure [40], there does seem to be s small region close to the trailing

edge on the lower surface where the velocity magnitude approaches zero (Dark Blue indicates zero velocity, dark red indicates maximum velocity). Therefore, this slow in the flow may have been triggered by mild transition, yet this is unapparent in the pressure distribution. At this stage, little can be drawn from the contour plots as there is minimal sign of any separation affecting the flow.

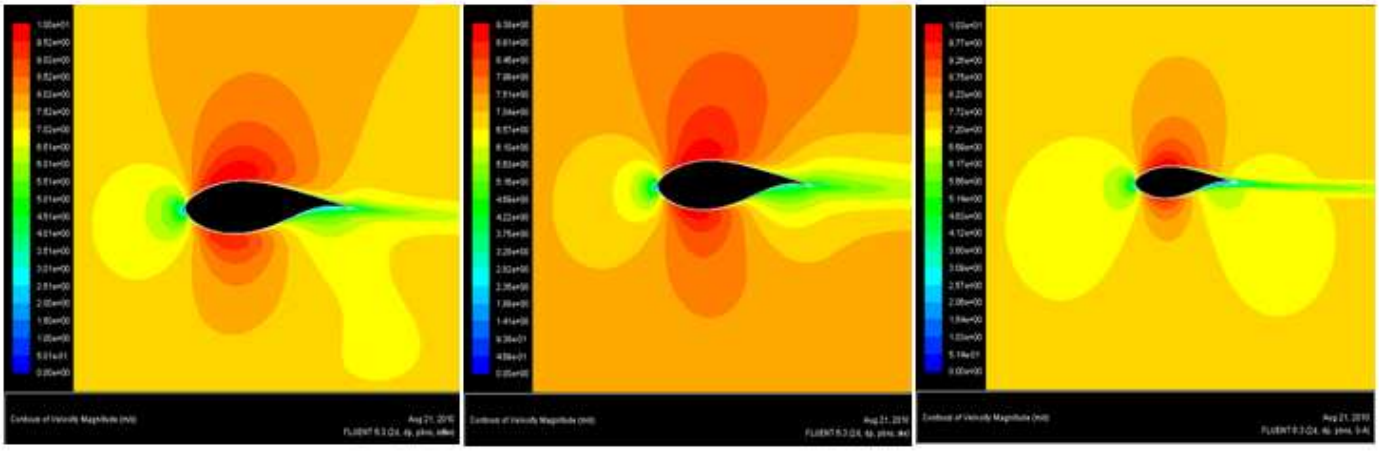

Figure 40 – Contour plots of velocity magnitude at $\alpha = 0°$ – Du91-W2-250 (Re = 500,000)

At $\alpha = 7°$ the S-A produces an excellent correlation with the experimental data. The magnitude of $-Cpmax$ and the location of the transition point are both modelled very well and to a better degree than both XFLR5 and RFOIL. In general, the shape of the pressure distribution is within a good agreement with the experimental data. As a result, the estimate of cl is the most accurate out of the five computational methods tested. Despite providing a good estimate of cl, the pressure distribution produced by the SST k-ω model is not in good agreement with that produced by experiment. It is unknown why this occurred, as the model generally performed well over the lift curve slope. Again the k-ε model under estimated $-Cpmax$, providing further evidence to suggest that the lagged flow could be a reason for the poor estimate of cl.

In terms of predicting cd, the S-A model was the closets out of the three turbulence models to matching the experimental data in the pre stall regime. Looking at the contour plots at $\alpha = 7°$ in Figure [41], paying close attention to the wake near the trailing edge, it can be seen that the

wake is relatively thin for the S-A model and quite thick for SST k-ω and k-ε. This thin wake may be the reason why the S-A model predicts the low values of drag better than the other models, as the thickness of the wake has a large impact on the pressure drag experienced by the airfoil. However, XFLR5 and RFOIL both performed better than FLUENT in predicting cd during the pre stall regime.

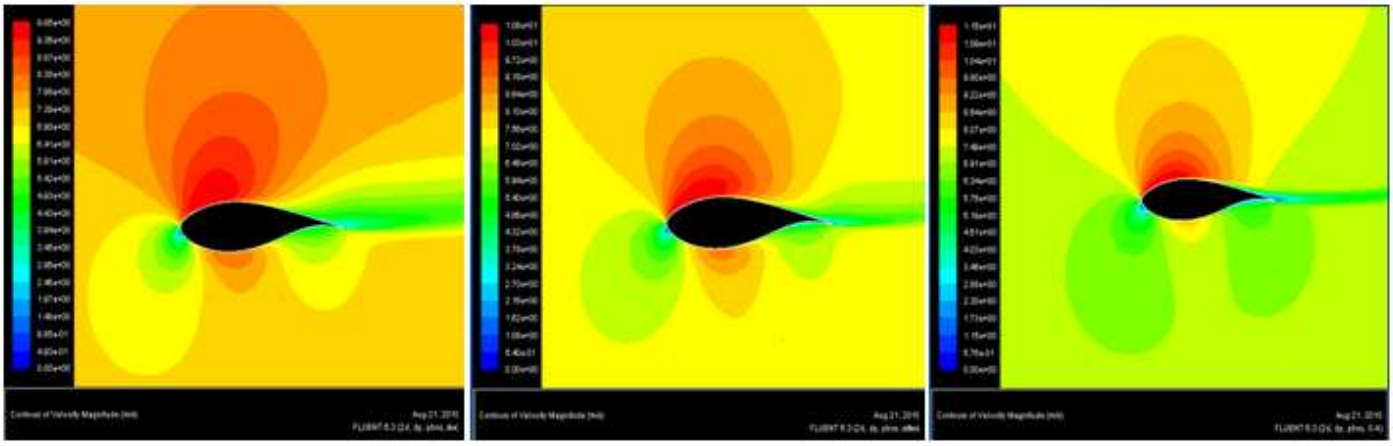

Figure 41 – Contour plots of velocity magnitude at $\alpha = 7°$ – Du91-W2-250 (Re = 500,000)

Both the S-A and SST k-ω models under predicted cl in the lead up to stall, and as a result, slightly overshot the AoA at which stall occurred. However, they still predicted $cl\,max$ reasonably well. The k-ε model overshot both the magnitude and occurrence of $cl\,max$. Looking at the pressure distributions at $\alpha = 11°$, which is just after stall, the k-ε plot has under estimated $-Cpmax$ and the severity of the adverse pressure gradients following transition. As a results the flow remains in the pre stall regime and the location of $cl\,max$ is delayed to a higher AoA. The S-A model predicts the separated region well yet over shoots the prediction of $-Cpmax$ which may be the cause of a delayed stall. $-Cpmax$ is accurately predicted by the SST k-ω model; however, the adverse pressure gradients following transition are not strong enough to cause the flow to separate over the region defined by experiment. This may be the cause of a delayed stall using this model as the flow remains attached over more of the upper surface. This prolonged region of attachment can be seen in the contour plots of velocity magnitude at $\alpha = 11°$ in Figure [42]. Comparing the SST k-ω model to the

S-A model, which models the separated region quite well, less of the flow appears to be separated from the surface at the trailing edge. Separated flow is denoted by dark blue, as this defines flow with near to zero velocity.

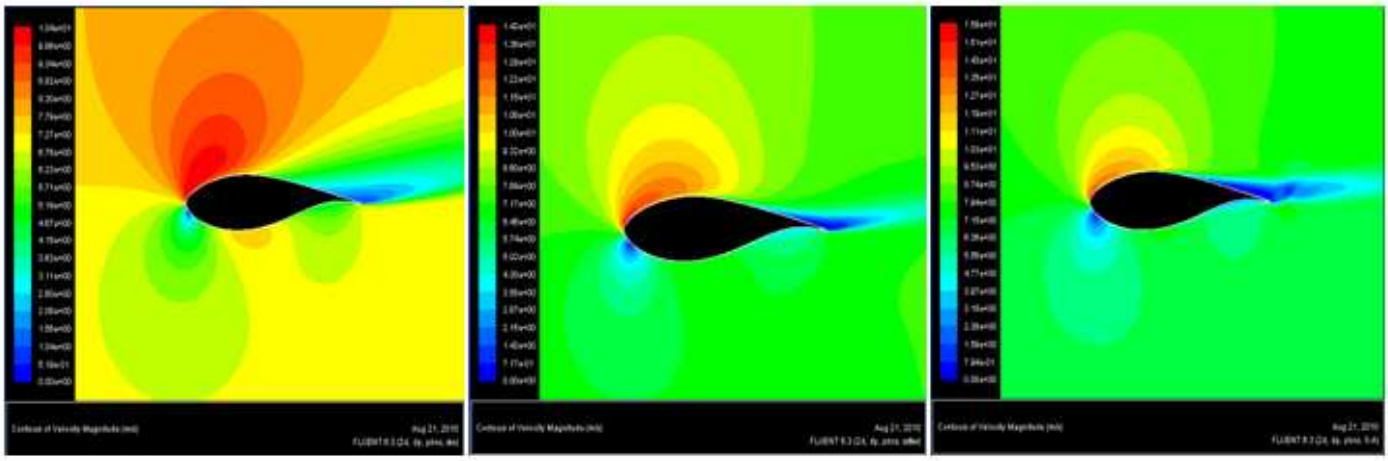

Figure 42 - plots of velocity magnitude at $\alpha = 7°$ – Du91-W2-250 (Re = 500,000)

In the post stall regime, the S-A and SST k-ω models performed better than the two airfoil design and analysis codes when predicting cl. The S-A exhibited the most accurate post stall characteristics when predicting cd. However, with no experimental pressure distributions available at high AoA, no conclusion can be made by examining the pressure distributions at $\alpha = 18°$.

The poor performance of the turbulence models when predicting cm can be put down to an error in the set up of the problem in FLUENT. When calculating the moment on a body in FLUENT, the software requires a frame of reference to take moments about. This was taken as the airfoil quarter chord at the coordinate location (-0.25, 0, 0) within the mesh. On close inspection of the script developed to perform large scale simulations, an error was made when setting this reference. Unfortunately, there was not the time available at the end of the project to re-do these simulations.

9.1.3 – NACA-64-418

9.1.3.1 - Results

The computed results for the NACA 64-418 airfoil are presented in this section and compared to those acquired via experiment. Figures [4.7 to 4.12] in *Appendix 4* display the lift, drag and moment polars from the experimental data and the corresponding computed results using the two airfoil analysis and design codes and the three turbulence models used in FLUENT. Table [7] displays a select number of lift and drag coefficients in tabular form taken from the results set at Re = 1,000,000.

Alpha (°)		Cl							Cd					
		EXP	XFLR5	RFOIL	S-A	k-w	k-e		EXP	XFLR5	RFOIL	S-A	k-w	k-e
10		1.157	1.159	1.151	1.222	1.254	1.112		0.0324	0.0191	0.0226	0.0250	0.0381	0.1121
12		1.199	1.221	1.181	1.369	1.261	1.197		0.0588	0.0278	0.0355	0.0324	0.0489	0.1389
16		1.221	1.3365	1.170	1.306	1.294	1.2642		0.1042	0.0564	0.0735	0.0774	0.0735	0.2014
22		1.084	1.361	1.098	1.104	1.176	1.168		0.2019	0.1363	0.1793	0.1764	0.1281	0.3153

Table 7 – Experimental and computed lift and drag coefficients – NACA 64-418 (Re = 100,000,000)

9.1.3.2 – Discussion

Considering first Re = 1,000,000; looking at the lift polars in Figure [4.10], *Appendix 4* the performances of XFLR5 and RFOIL are again very good when predicting the lift curve slope. In the lead up to stall they continue to give a good estimate of cl, as seen in Table [7] at $\alpha = 10°$ where the deviations from the experiment are 0.17% for XFLR5 and 0.51% for RFOIL respectively. Errors in the data in Table [7] continue to be marginal as the airfoil moves further towards stall at $\alpha = 12°$. From experiment the airfoil is said to eventually stall at $\alpha = 16°$ with cl max $= 1.22$. RFOIL under estimates $cl\ max$ at 1.17 and predicts its occurrence too early at $\alpha = 14°$; however, the stall is gentle enough to still make an accurate prediction of cl at $\alpha = 16°$ with an error of only 4%. XFLR5 overshoots both the magnitude and occurrence of stall, predicting cl max $= 1.37$ at $\alpha = 20°$. In the post stall regime RFOIL performs better, just under estimating cl values by errors consistent of around 4%. As a result of it overshooting stall, XFLR5 consistently over predicts the value of cl during the post stall regime.

The S-A and SST k-ω models again provide a good correlation with the experimental data during the lift curve slope, with XFLR5 and RFOIL performing marginally better. The k-ε model performs better than previously in this case. In the lead up to stall, both the S-A and SST k-ω models over predict cl as seen at $\alpha = 10°$ and 12° in Table [7], with the SST k-ω model performing better out of the two. Despite an initial drop in performance, the k-ε model for the first time exhibits the best performance out of the three turbulence models, making errors of only 4% and 0.16% in the lead up to stall at $\alpha = 10°$ and 12°. The model also accurately predicts the occurrence of stall at $\alpha = 16°$ but overshoots the value of $cl\ max$, however only by an error of 3.6%. Here it again performs better than the S-A and SST k-ω models, despite the SST k-ω accurately predicting the occurrence of $cl\ max$. In the post stall regime all the turbulence models compare comparatively well to the performance of RFOIL in providing a good correlation to the experimental data.

Looking at the drag polars in Figure [4.11], *Appendix 4* a similar pattern is witnessed to before with the Du91-W2-250 with significantly larger errors present than the lift data. Deviations from the experimental data are at best 30%. Out of the five methods tested, XFLR5, RFOIL and the S-A model in FLUENT again provide the most accurate correlation

with the experimental data. The worst performing model is again the k-ε model used in FLUENT.

Once again the three turbulence models used in FLUENT significantly over predict Cm, with the shape of the curves barely coming close to representing that of the experimental data in Figure [4.12] *Appendix 4*. XFLR5 and RFOIL both predict the moment coefficient well during the lead up to stall and both overestimate values at stall and in the early stages of the post stall regime. At high AoA i.e. > 16°, RFOIL exhibits the better performance.

Experimental data for the NACA 64-418 was provided at Re = 300,000. This was the lowest number analysed using computational methods. Considering the lift polars in Figure [4.7], *Appendix 4* XFLR5 and RFOIL provided the closets correlation to the experimental data during the lift curve slope. Experimentally, stall is predicted at $\alpha = 9°$ with cl max $= 1.251$. XFLR5 and RFOIL both under estimate the occurrence of stall at $\alpha = 8°$ and the magnitude of $cl\ max$ with errors of 5.27% and 6.17% respectively, with XFLR5 performing slightly better out of the two. During the initial stages of the post stall regime, RFOIL under predicts the experimental data with errors consistent of ≈ 11%; however, at high AoA, i.e. > 16° RFOIL failed to provide a converged solution and hence no data was available for comparison. XFLR5 provided a similar correlation; however, with errors of ≈ 5% consistently less than RFOIL. It too encountered convergence issues, failing to provide a converged solution above $\alpha = 14°$.

The lift curve slope was initially predicted very well by the S-A model; however, in the lead up to stall values of cl are under estimated leading to an eventual overshoot in the prediction of the occurrence of stall, with $\alpha = 14°$, and in the magnitude of $cl\ max$, estimated at 1.292. The performance of the SST k-ω and k-ε models are comparatively worse, both providing poor estimates of the lift curve slope and predicting stall at $\alpha = 18°$, doubling that of the experimental data. Of the three models tested, the SST k-ω model performed the worst, predicting cl max $= 1.4709$ with an error of 27%; the highest encountered throughout the entire analysis. Despite their ability to provide a converged solution at high AoA, all three turbulence models used in FLUENT performed worse than XFOIL and RFOIL in the lead up to and during stall.

The drag polars in Figure [4.8] *Appendix 4* display a common pattern observed throughout this analysis, with XFLR5 and RFOIL providing the closest correlation to the experimental data in the lead up to and just after stall, and the S-A model performing the best out of the three turbulence models. The k-ε model again provides the poorest correlation with errors exceeding 400% at stall. Of all the Reynolds numbers tested, the performance of S-A model in the latter stages of the post stall regime, which is usually fairly good, is the least accurate.

For the moment polars in Figure [4.12] *Appendix 4* errors in the turbulence models are again significantly higher than XFLR5 and RFOIL; however, the two codes do not perform as well as previously at this low Reynolds number. The moment distribution remains fairly static and does not map that of the experimental data well in the lead up to and after stall.

9.1.3.3 Analysis

Similarly to before with The Du91-W2-250 airfoil, a comparison of the pressure distributions generated by the models to the experimental data can be useful in describing some of the underlying reasons behind the discrepancies in the results within the lift and drag polars. Experimentally, pressure distributions were provided at a Reynolds number of 1,000,000 for the NACA 64-418, displayed below in Figure [43]. Computed pressure distributions at Re = 1,000,000 are displayed in Figure [44].

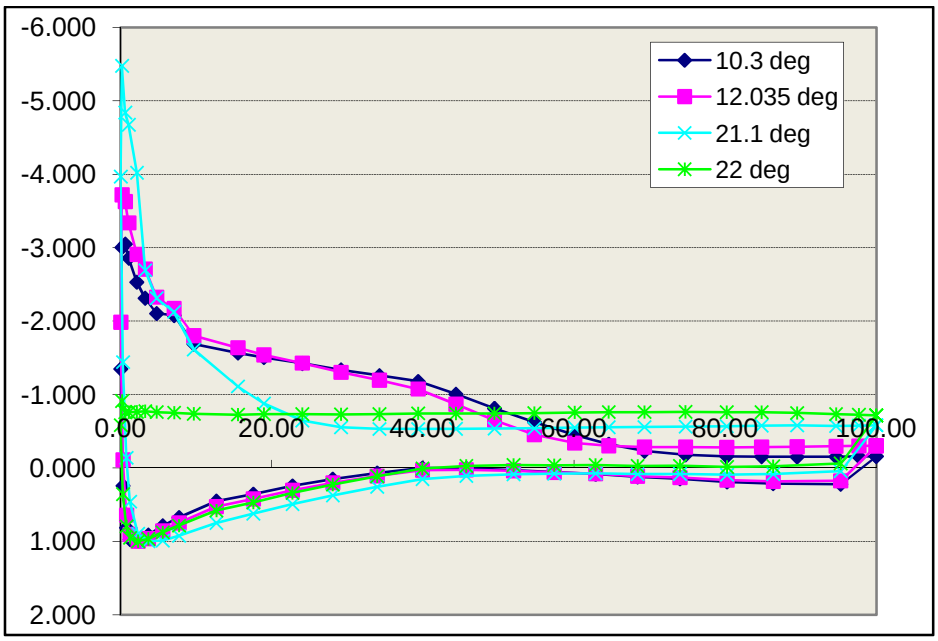

Figure 43 - Pressure distributions – NACA 64-418 (Re =1,000,000)

XFLR5 was shown to predict the lift curve slope well, yet it overshot the occurrence of stall and the magnitude of $cl\,max$. Values of cl continued to be over estimated during the post stall regime. Experimentally, stall was shown to occur at $\alpha = 16°$. Looking at the pressure distributions in the lead up to stall at $\alpha = 10°$ and12°, transition occurs at $\approx$ 10% the chord from the leading edge. The following adverse pressure gradients are strong enough to separate the flow near the trailing edge with around 30% of the upper surface stalled at $\alpha = 10°$ and 40% stalled at $\alpha = 12°$. $-Cpmax$ rises from -3 at to -3.75. Comparing these plots to those produced by XFLR5, the locations of the transition points are well estimated; however, the separation points are under estimated leading to smaller regions of separated

flow near the trailing edge. This delay in the aft movement of the separation point may be the reason why XFLR5 eventually overshoots stall. As a result, the code over predicts cl values in the post stall regime as it assumes the flow to be less developed towards a fully stalled state. This is highlighted in the pressure distributions at $\alpha = 22°$. In the experimental data the flow is fully stalled with Cp values close to -1 across the entire upper surface. In the plot produced by XFLR5 there is still attached flow at the leading edge, encompassing around 30% of the total upper surface.

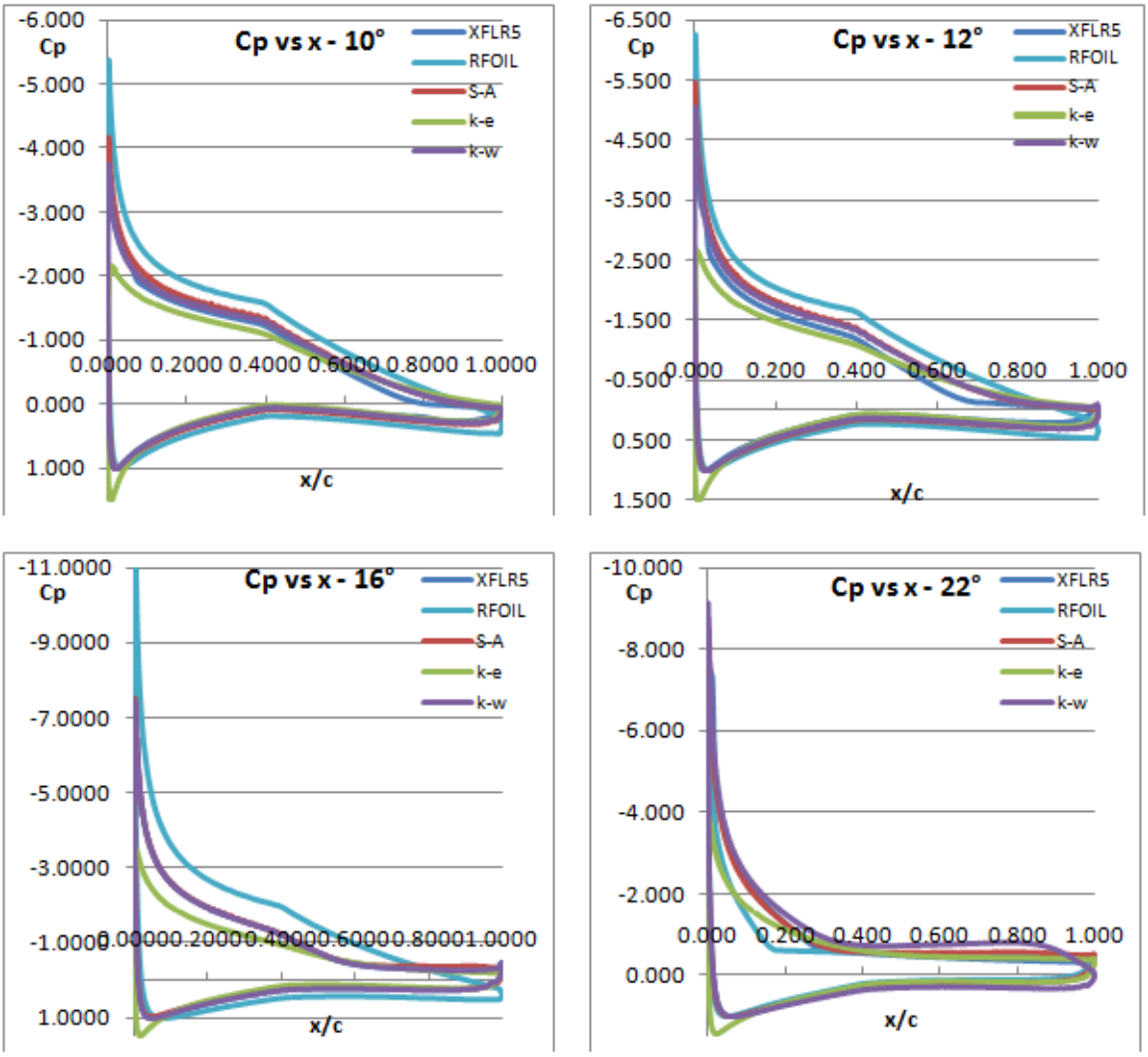

Figure 44 – Computed NACA 64-418 pressure distributions (Re = 1,000,000)

RFOIL was shown to again provide a good estimate of the lift curve slope; however, in contrast to XFLR5 it under shot the occurrence of stall, but due to the mild stall that it predicted, cl values in the post stall regime were relatively well estimated. To explain the good performance of RFOIL is difficult via an analysis of the pressure distributions, as they do not portray well the events that occur in the lift and drag polars. The occurrence of transition is delayed and the following adverse pressure gradients are not strong enough to separate the flow at the trailing edge. If anything this suggests that the flow is delayed in becoming stalled. Despite this, the pressure plot at $\alpha = 22°$ compares well with that of experiment, with a good estimate of the fully stalled region on the airfoil upper surface. This may explain why RFOIL predicts the lift and drag coefficients during post stall regime so well.

Of the three turbulence models analysed, all three predicted the initial stages of the lift curve slope fairly well. However, when predicting cd pre stall, the S-A and SST k-ω models performed significantly better the k-ε, with the S-A producing the most accurate results. Figures [45] and [46] show contour plots of the velocity magnitudes around the airfoil at $\alpha = 10°$ and 12°. As shown previously with the Du91-W2-250 airfoil, the wake region is again a lot fuller with the solution provided by the k-ε model. This may produce a large pressure drag resulting in a significant overestimate of drag

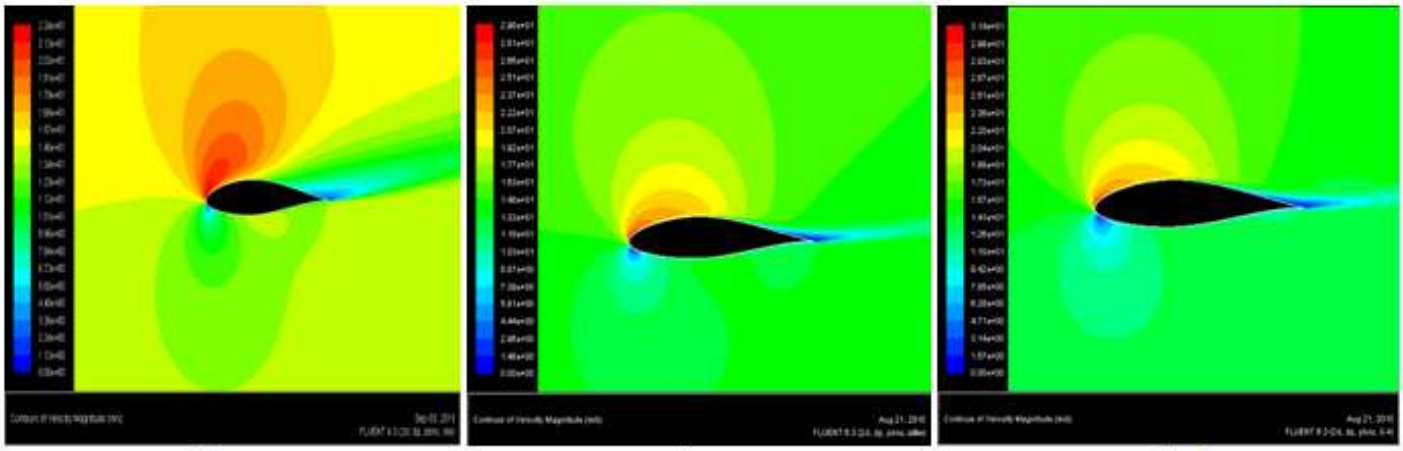

Figure 45 - Plots of velocity magnitude at $\alpha = 10°$ – NACA 64-418 (Re = 1,000,000)

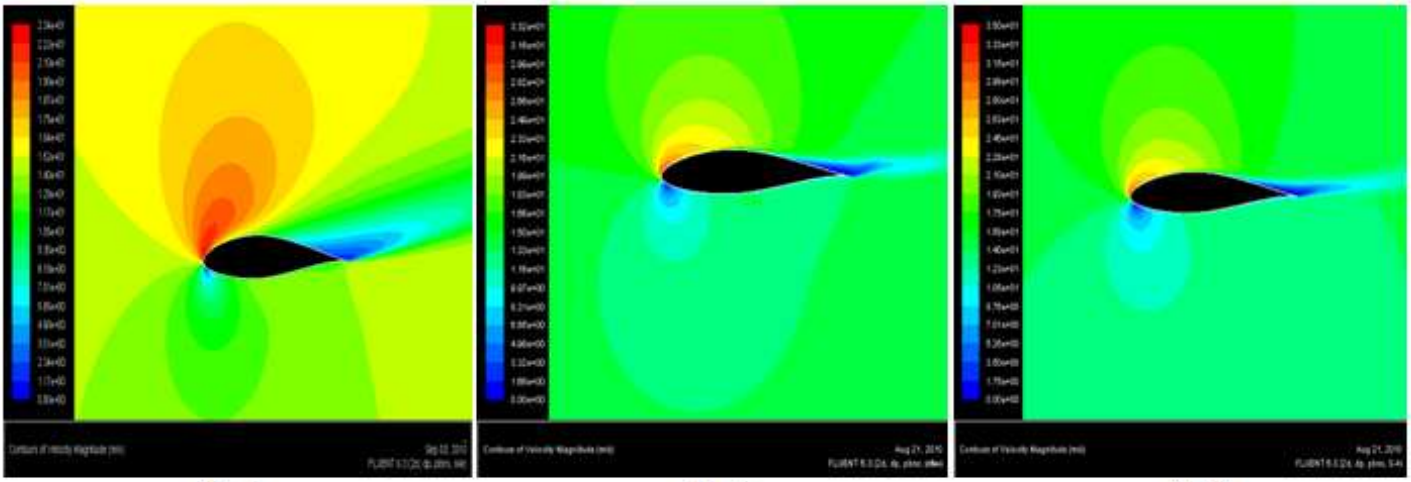

Figure 46 - Plots of velocity magnitude at $\alpha = 12°$ – NACA 64-418 (Re = 1,000,000)

Despite a good early performance, all three turbulence models over estimated the value of cl in the lead up to and during stall, to a further extent than XFLR5. Looking at the pressure distributions at $\alpha = 10°$ and 12° the regions of separated flow are smaller for the turbulence models in comparison to experiment and XFLR5. At $\alpha = 12°$ they should encompass around 40% of the airfoil upper surface from the trailing edge; however, looking at the contour plots in Figure [46] the dark blue regions of separated appear to all cover less than this. For similar reasons previously described with XFLR5, this delayed movement of the separation point may account for the overshoots in lift experienced in the lead up to and during stall.

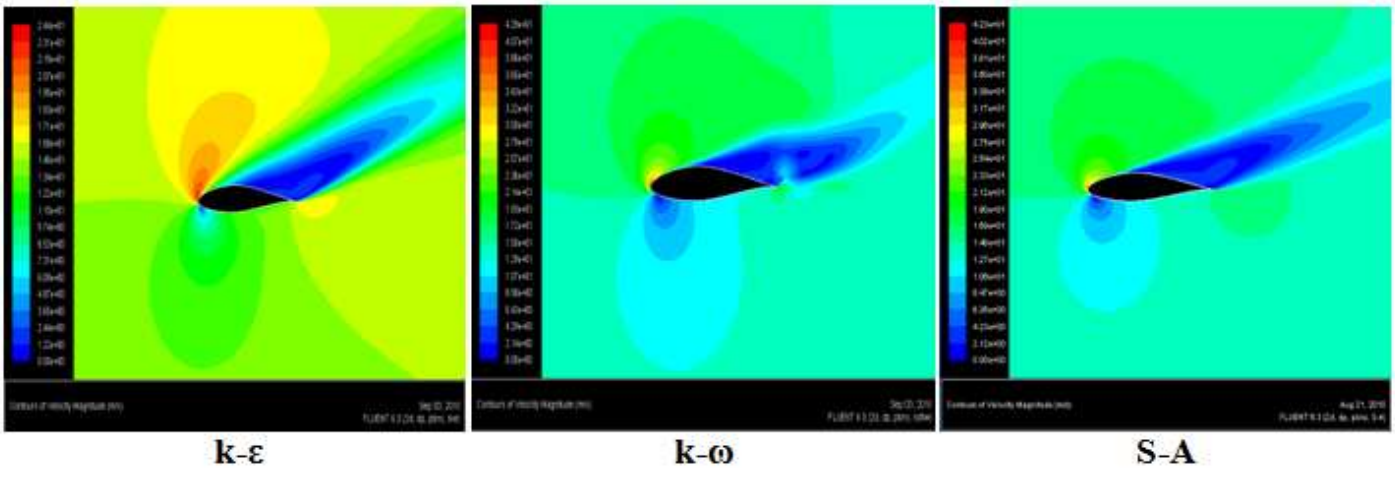

Figure 47 - Plots of velocity magnitude at $\alpha = 12°$ – NACA 64-418 (Re = 1,000,000)

In the post stall regime all three models perform relatively well and to a similar standard; however, overshoots in lift are still consistent across the entire alpha range. Again, looking at the pressure distributions at $\alpha = 22°$ the flow should not still be attached near the leading edge, it should be fully separated as shown in the experimental data. This delayed region of attached flow is illustrated above in Figure [47] where, for each turbulence model a small region of high velocity (red) flow can be seen at the leading edge. As flow separation dramatically reduces lift, this provides evidence to illustrate why the models over estimate cl during the post stall regime.

9.1.4 – Overall Analysis

Looking at the analysis as a whole, there was a wide variety of results produced by each computational method between the two airfoils analysed and the three Reynolds numbers tested. In the use of CFD, the S-A and SST k-ω models performed to a higher standard than k-ε model, despite performing better at Re = 1,000,000 with the NACA 64-418 airfoil than with the Du91-W2-250. This illustrates that there can be some variability with the performance of the models depending on the geometry of the airfoil analysed. The S-A model consistently provided the most accurate representation of the drag polar and in general an above average estimate of the lift; as a result, it exhibited the highest performance characteristics of the three models used in FLUENT. The models seemed to improve at higher Reynolds numbers, providing the poorest correlation at Re = 300,000. XFLR5 produced excellent results each time when modelling the lift curve slope, with less variability than with the CFD solver. However, in the turbulent post stall regime it tended to consistently over predict lift and under predict drag, performing to a lower standard than the highest performing turbulence model. These problems were exasperated at higher Reynolds numbers. The code also experienced convergence issues at the lowest Reynolds number. RFOIL tended to perform better at higher Reynolds numbers and under predict lift during the post stall regime. Like XFLR5, in general it performed better at modelling the lift and drag values during the inviscid lead up to stall than during the turbulent post stall regime in comparison to the best performing CFD solver. It too encountered convergence issues at the low Reynolds number. An attempt to provide a first look analysis of the reasons behind the discrepancies within these results was described in the previous two sections. The following looks at the

underlying philosophies behind the models in more detail in order to supplement those findings.

In a general sense, the lift curve slope and the corresponding drag coefficients were modelled better than the stall and post stall regime. Errors in the prediction of cl were on average around 40% less than those in the prediction of cd, indicating that the drag force is the most difficult to predict when applying a computational method. This is likely to be due to the fact that the drag force is much more influenced by surface friction and hence, viscous forces than lift, which derives the majority of its value from the pressure distribution. Viscous behaviour in the boundary layer is more difficult to evaluate and accurately model. Additionally, the lift force during and after stall also becomes harder to model as it becomes more influenced by flow separation as a result of added viscosity in the flow.

The result showed that perhaps the most important aspects of modelling the aerodynamic characteristics of airfoils are to accurately predict the adverse pressure gradients in boundary layer flows, the location of separation and the behaviour of the turbulent wake region. Particular attention was drawn to the ability of the models to predict the separated region and the size and behaviour of the turbulent wake. The performance of the k-ε model in FLUENT was shown in general to be deficient in modelling the aerodynamic characteristics of both airfoils. The particularly full wake region was identified as a possible reason for its poor prediction of drag. In the derivation of the k-ε model, the assumption is that the flow is fully turbulent, and the effects of molecular viscosity are negligible [28]. Therefore, this makes it only valid for fully turbulent flows and hence, deficient for modelling adverse pressure gradients flows with transition from laminar to turbulent flow. One reason for the model performing relatively better at the higher Reynolds number is perhaps due to the decreased viscosity in the flow allowing a closer estimate to be made. Here standard wall functions (i.e. $y+ > 30$) can sometimes be sufficient. On the contrary, the S-A model was designed specifically for aerospace applications involving wall-bounded flows with boundary layers subjected to adverse pressure gradients [28]. This makes it more applicable for the evaluation of the flows over airfoils. Both the S-A and SST k-ω models require the flow to be resolved in the viscous sub layer ($y+ < 5$) which make them more applicable for adverse pressure gradient flows over airfoils. This has been shown to be true within this analysis. The improved results gained by using the wake adapted mesh highlighted the importance of

accurately modelling the wake affected region when using CFD to model airfoil characteristics.

The poor performance of the turbulence models at the low Reynolds number (Re = 300,000) may be due to the fact that at this flow velocity the flow over the airfoil may be predominantly laminar, as opposed to turbulent at high angles of attack. Experimental data at this Reynolds number was provided for the NACA 64-418 airfoil which was employed at the tips of the blades on the MEXICO model. At the tips of the blade, where most of the useful lift is generated, laminar airfoils are often employed to minimise drag and increase the lift to drag ratio. Here the boundary layer is often uninterrupted by turbulence at high AoA. Therefore, using a turbulence model to determine the airfoil characteristics in a predominantly laminar regime may not provide the most accurate solution. Here it may have been more wise to use the laminar viscous model in FLUENT. This also goes some way to explaining why the lift curve slope is not always accurately predicted using turbulence models in FLUENT. The models have no means for predicting the transition from laminar to turbulent flow and hence, produce inaccurate results. The best case scenario would be to run both the laminar and turbulence models with some sort of transition model together; however, this is unavailable in most commercially available CFD codes [17].

9.2 - BEM Analysis

The following section takes the lift and drag coefficients, determined from the 2D airfoil analysis and inputs them into the available BEM code to evaluate the impact that the deviations in the results may have on the prediction of turbine performance. The aim here is to show how important it is to make a careful selection of the method used if a design team chooses to determine the aerodynamic characteristics of the airfoils they employ on the turbine via computational means. As this section is only intended to illustrate this point, only a few examples are shown. Results used as inputs to BEM are those obtained for the Du91-W2-250 airfoil at Re = 500,000 using experimental values, XFLR5, and the S-A and k-ε models used in FLUENT.

9.2.1 - Results

Figures [48- 51] display the outputs of BEM when using the four methods to determine the lift and drag coefficients of the Du91-W2-250 airfoil.

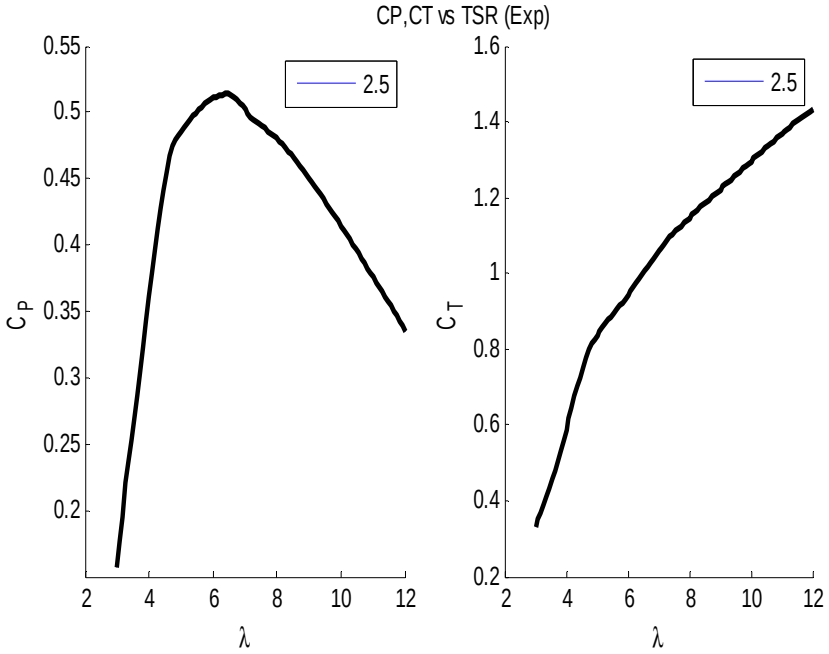

Figure 48 – BEM outputs using Experimental airfoil characteristics

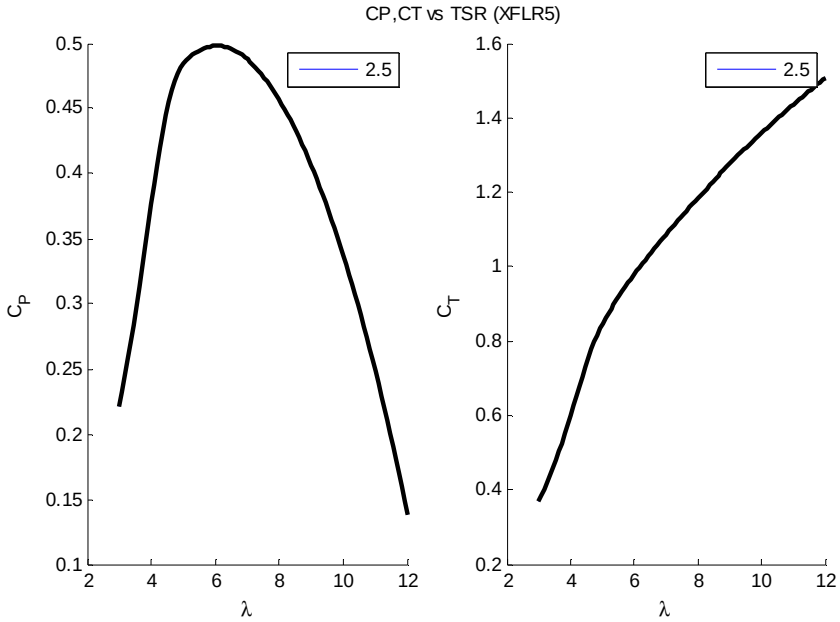

Figure 49 – BEM outputs using XFLR5 airfoil characteristics

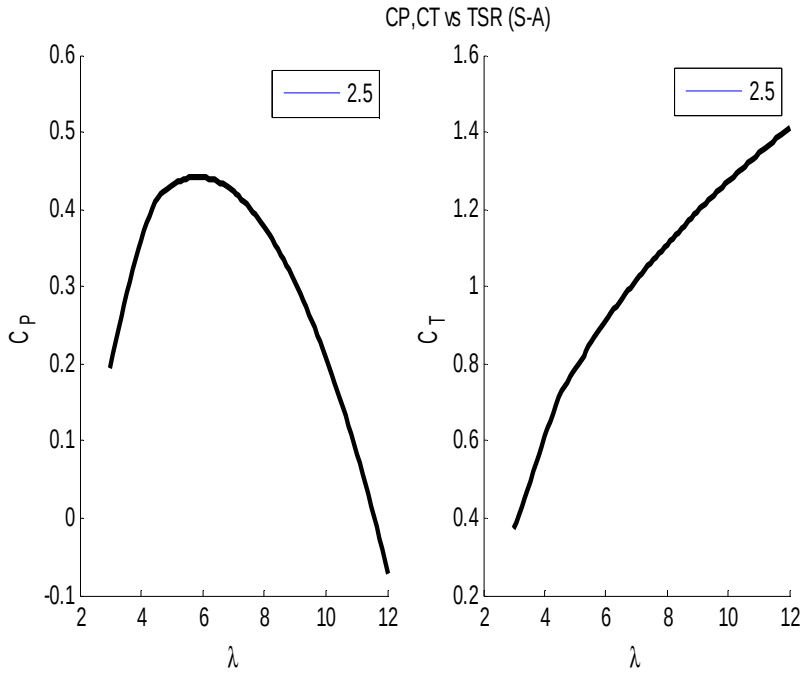

Figure 50 – BEM outputs using S-A model airfoil characteristics

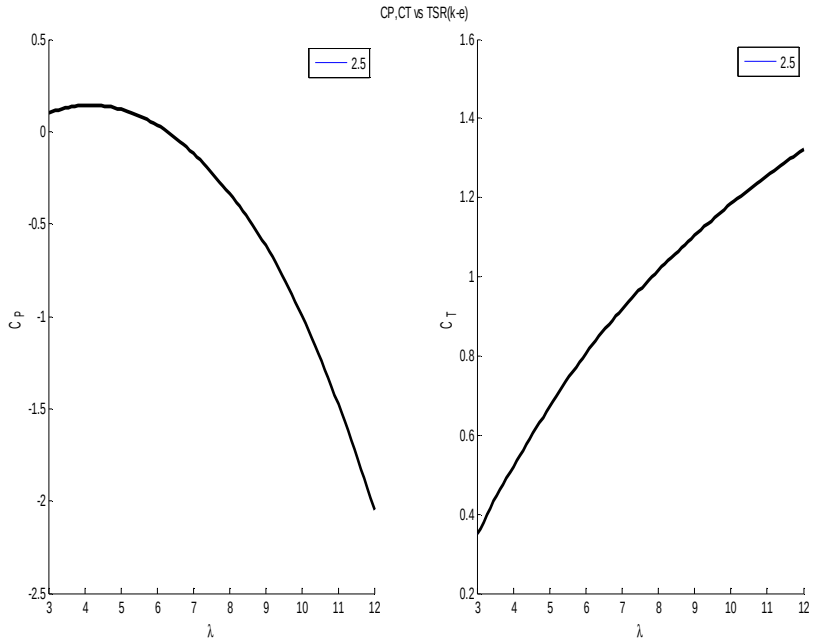

Figure 51 – BEM outputs using k-ε airfoil characteristics

9.2.2 – Discussion

It can be seen in the above figures that the deviations in the lift and drag coefficients has a negligible effect on the outputted thrust coefficient, yet a noticeable effect on the power coefficient. Using the experimental data it can be seen in Figure [48] that the turbine operates at an optimum TSR of 6 with efficiency close to that of the Betz limit, with $CP \approx 0.53$. Applying the data gathered using XFLR5, efficiency at TSR = 6 has dropped a little to ≈ 0.51 and a notable decrease in efficiency can be seen at higher TSR, as shown in Figure [49]. Now applying the data determined using the S-A model in FLUENT, the efficiency has dropped further at TSR = 6 to ≈ 0.45 and the turbine is actually producing CP values less than 0 at the higher TSR. Finally assessing the k-ε model in Figure [51], the efficiency of the turbine has dropped significantly across the full TSR range with CP values less than 0 experienced at much of the higher values.

9.2.3 – Analysis

In this example, the outputs from BEM highlighted that XFLR5 was in fact the best computational option for determining the airfoil characteristics of the Du91-W2-250, as it provided the closest correlation to the experimental data in terms of the power output of the model turbine. The worst option would be to use the k-ε model in FLUENT, although this was to be expected considering the poor correlation it made with the experimental data during the 2D airfoil analysis. For any designer considering the use of a computational method for determining wind turbine airfoil characteristics, this method of comparison using BEM would need to be adopted, as it was not at first clear from the 2D analysis whether or not the S-A model or XFLR5 produced the overall closest correlation to the experimental data.

Chapter 10

Conclusion

The main aim of this thesis was to highlight and address some of the issues that can arise when trying to model the aerodynamic characteristics of wind turbine airfoils using commercially available computational methods. Each method chosen was to be analysed for its ease of use and accuracy when used to remodel the aerodynamic characteristics of two airfoils, previously determined by experiment.

When using CFD those issues mainly fell under two headings – “Grid management” and “Selection of Turbulence model”. It was shown that to accurately model the characteristics of wind turbine airfoils using CFD, special care needs to be made when refining the region of the wake within the computational grid. Wind turbine airfoils have a wake distribution unlike that of symmetric airfoils commonly used in other aerospace applications. Appropriate mapping of this wake needs to be made in the grid when running simulations to develop lift and drag polars over a large range of angles of attack. For an accurate solution, the selection of the turbulence model has been shown to be very important. This thesis identified the S-A and SST k-ω models as the best options for modelling the adverse pressure gradient flows over airfoils. The k-ε model was the worst performing model out of the three tested as it was unable to resolve the behaviour of the flow in the viscous sub layer of the boundary layer. Evidence from this report has reinforced many works that can be found in literature that show that for a turbulence model to accurately model the aerodynamic characteristics of airfoils, it needs to be able to accurately model adverse pressure gradients flows.

In terms of ease of use, the two airfoil analysis and design codes, XFLR5 and RFOIL, were considerably faster and easier to use than CFD. The use of the codes took less than a day to master and simulations could be set up and run in under one minute. In contrast, it took over three months to learn how to use CFD appropriately for modelling airfoils, having to learn how to generate a mesh and run the mesh in FLUENT. Simulations sometimes took over a day to run and process. If a quick solution is required, it would be advisable to use either

XFLR5 or RFOIL as they have the ability to provide a relatively accurate solution within minutes, at no cost to the designer. However, if the time and funds were available, the use of CFD would be recommended. This report highlighted the learning curve that comes with using CFD. By the cessation of the project, results using the S-A model were becoming increasingly close and often better than those produced using XFLR5 or RFOIL. Despite being very fast and easy to use, XFLR5 and RFOIL at times failed to provide a converged solution and struggled to model fully turbulent flow. These programs are limited in their use in this instance as modifications to their codes are not easily applied. However, with CFD a designer can always use their own intuition in the theory of aerodynamic flows to refine the grid or redefine the solution method to achieve a converged or improved result.

This learning curve was shown in the development of the grid adaption test in this report. The methodology behind this test, including the method for running large scale simulations in FLUENT and generating multiple mesh files in GAMBIT using script files is therefore a key deliverable of this thesis. The use of this methodology can significantly cut simulation and grid development times and improve the accuracy of results. The next stage in the process would be to run the refined meshes and see if any further improvement could be made on the current results determined in this thesis using CFD. If improvements were made, this stage of the process could be added to the methodology.

A final deliverable would be the view that designers cannot whole heartedly trust airfoil characteristics they determine using computational methods, unless they have experimental data to verify their results. If a turbine was developed using inaccurate results, a false evaluation of the performance levels and economic value of the turbine could be made. This was shown to be true in the short BEM analysis conducted in this report. Computed results should therefore always be backed up with results from experiment if wind turbines are to be fully trusted as reliable means for generating electricity.

Appendix 1

Du91-W2-250 – Experimental airfoil characteristics

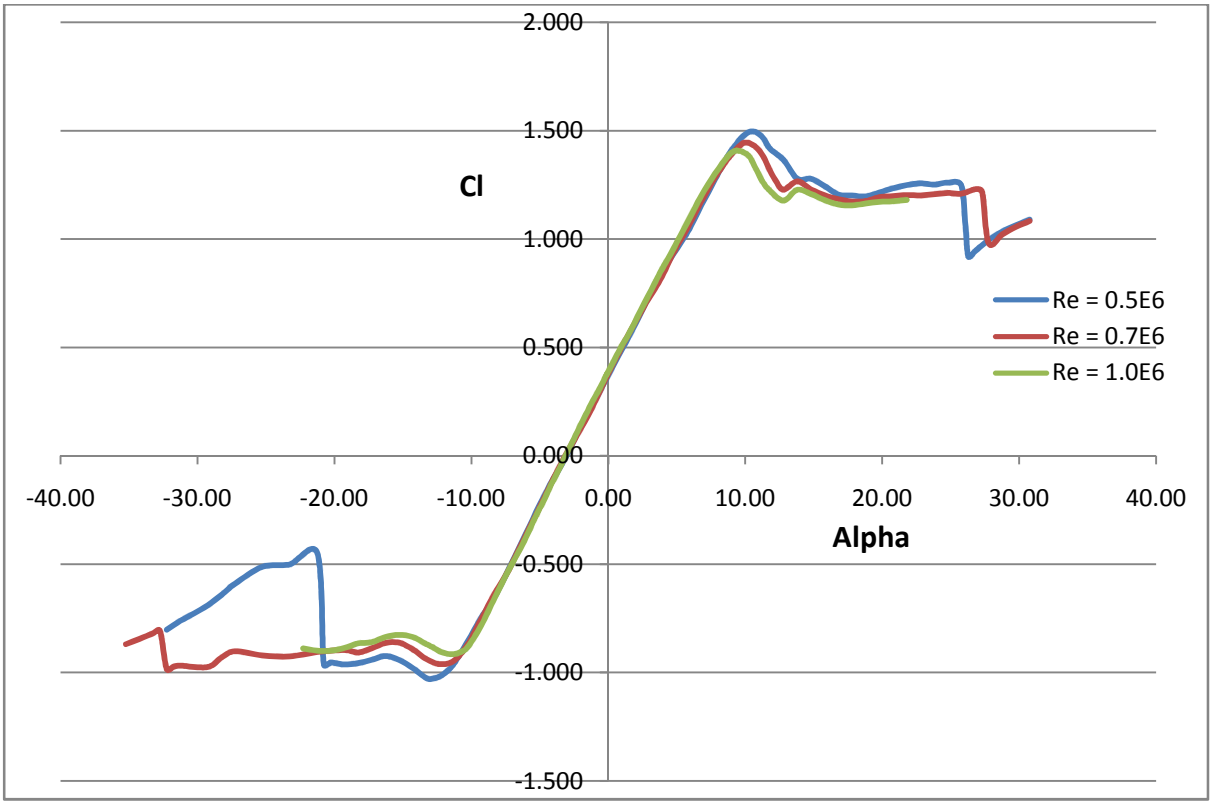

Figure .1 – Experimental Cl vs α - Du91-W2-250

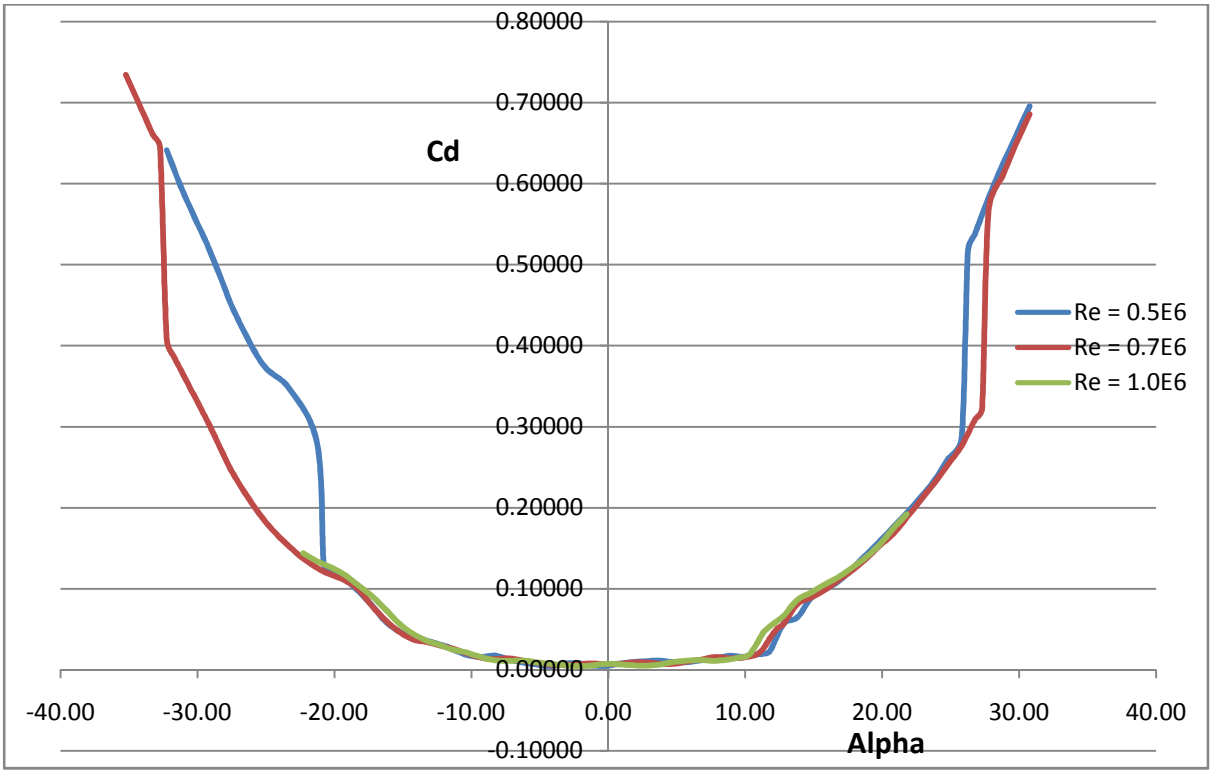

Figure 1.2 Experimental Cd vs α - Du91-W2-250

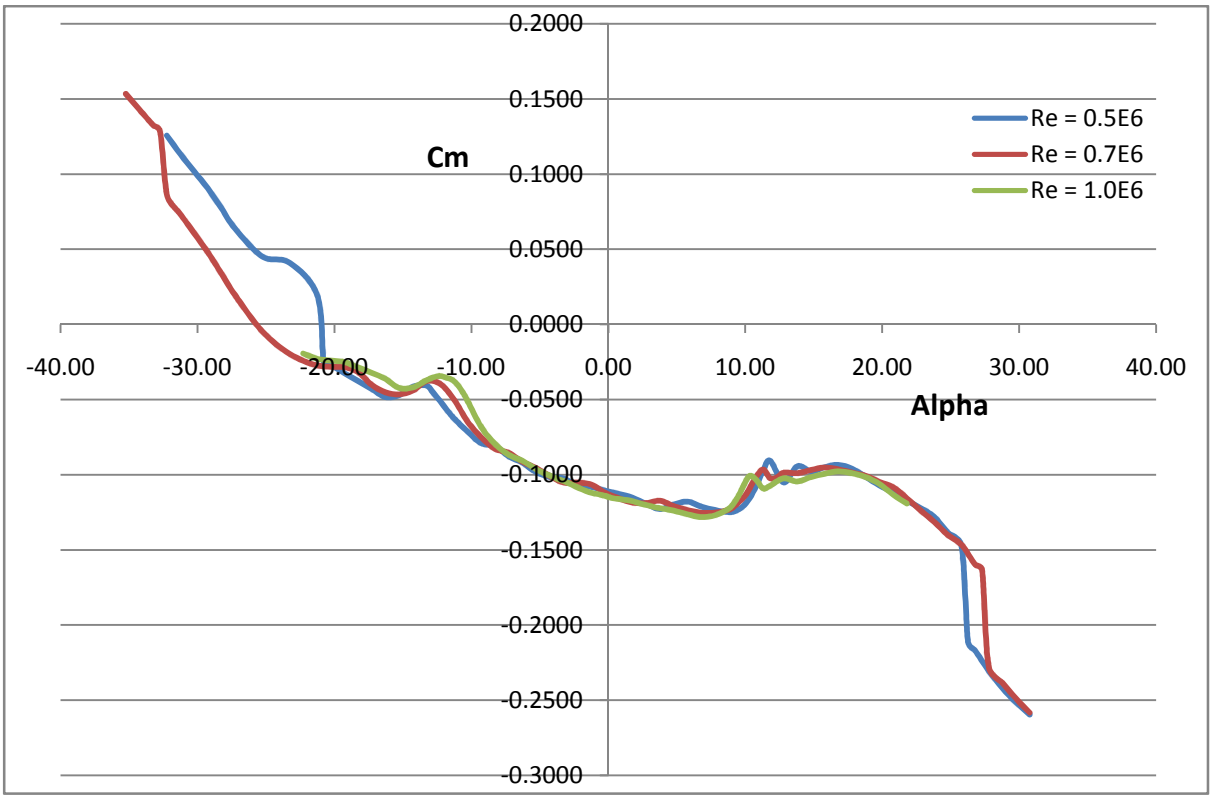

Figure 1.3 – Experimental Cm vs α – Du91-W2-250

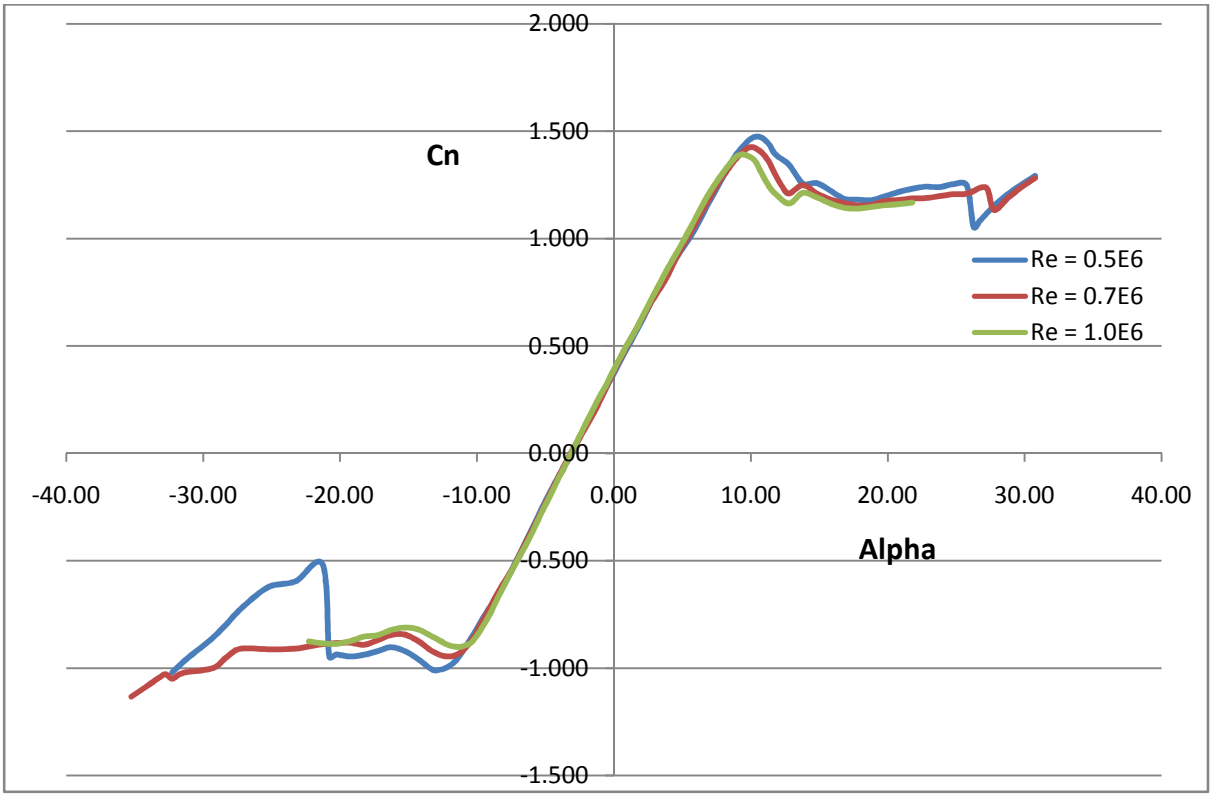

Figure 1.4 – Experimental Cn vs α – Du91-W2-250

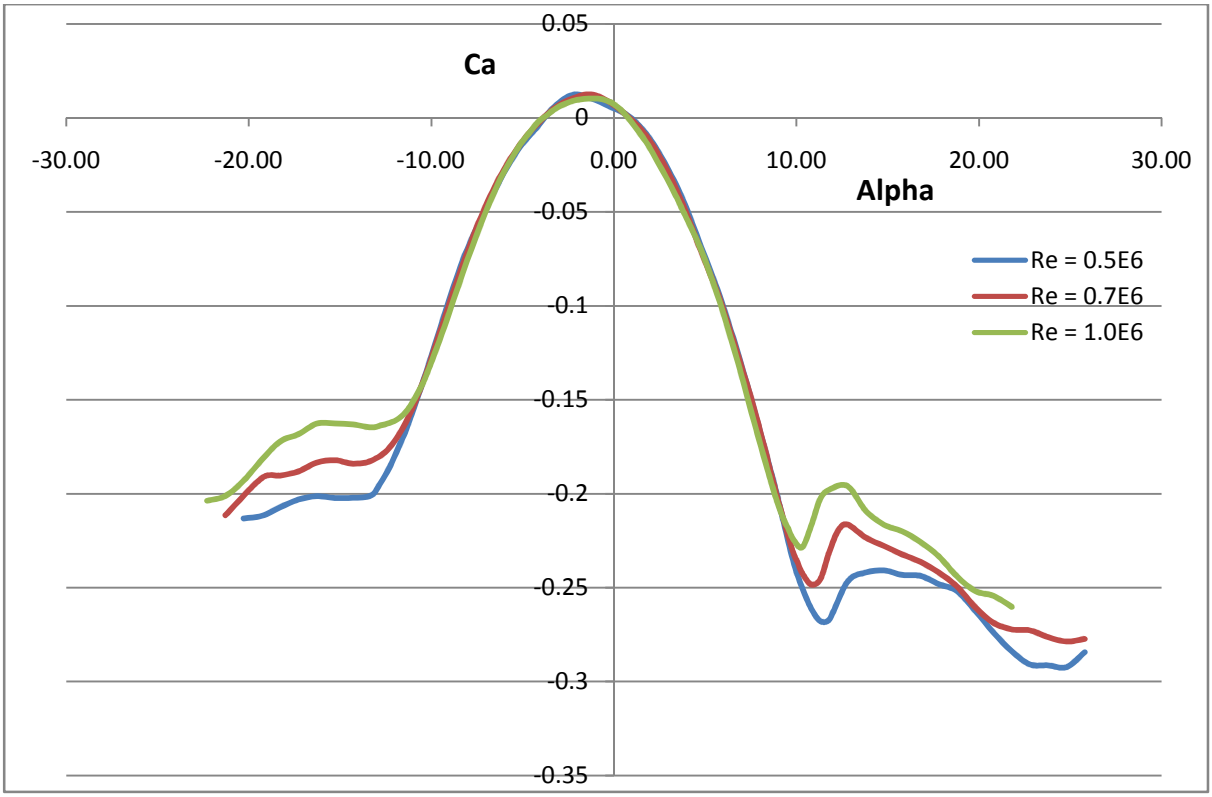

Figure 1.5 – Experimental Ct vs α – Du91-W2-250

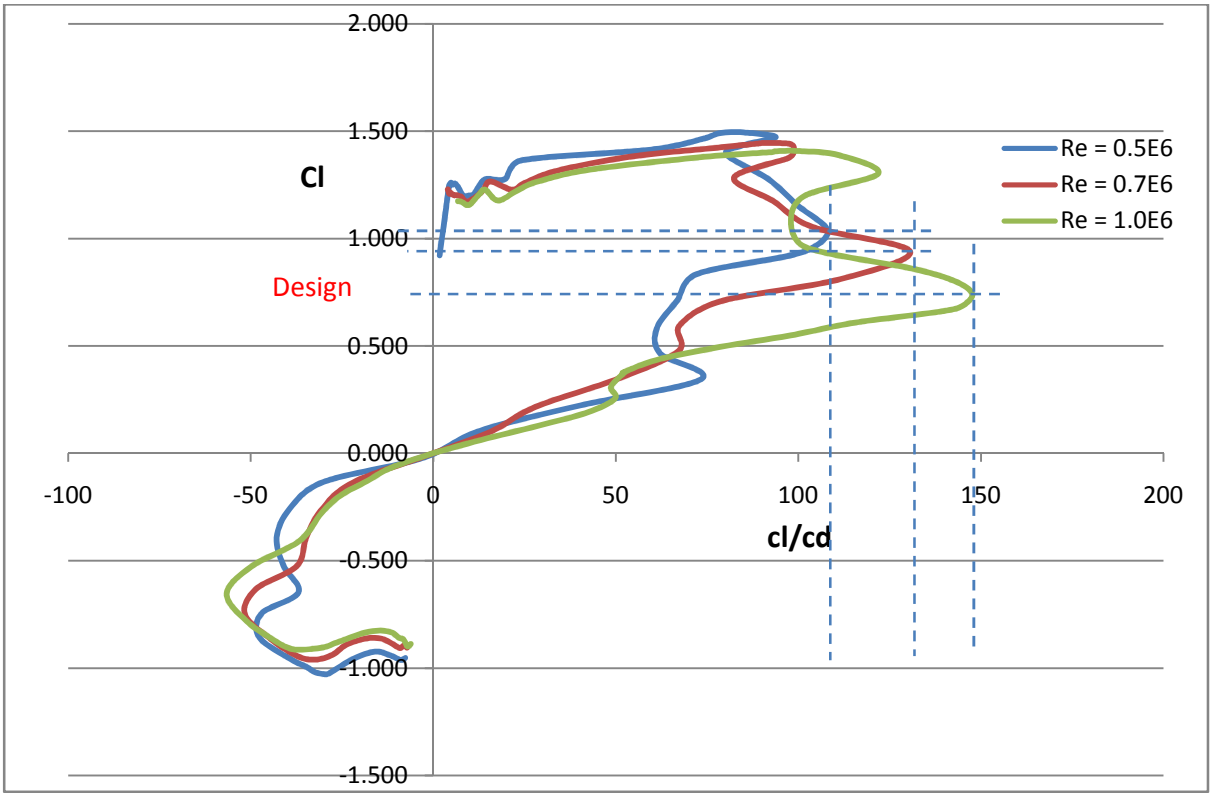

Figure 1.6 – Experimental Cl vs Cl/Cd – Du91-W2-250

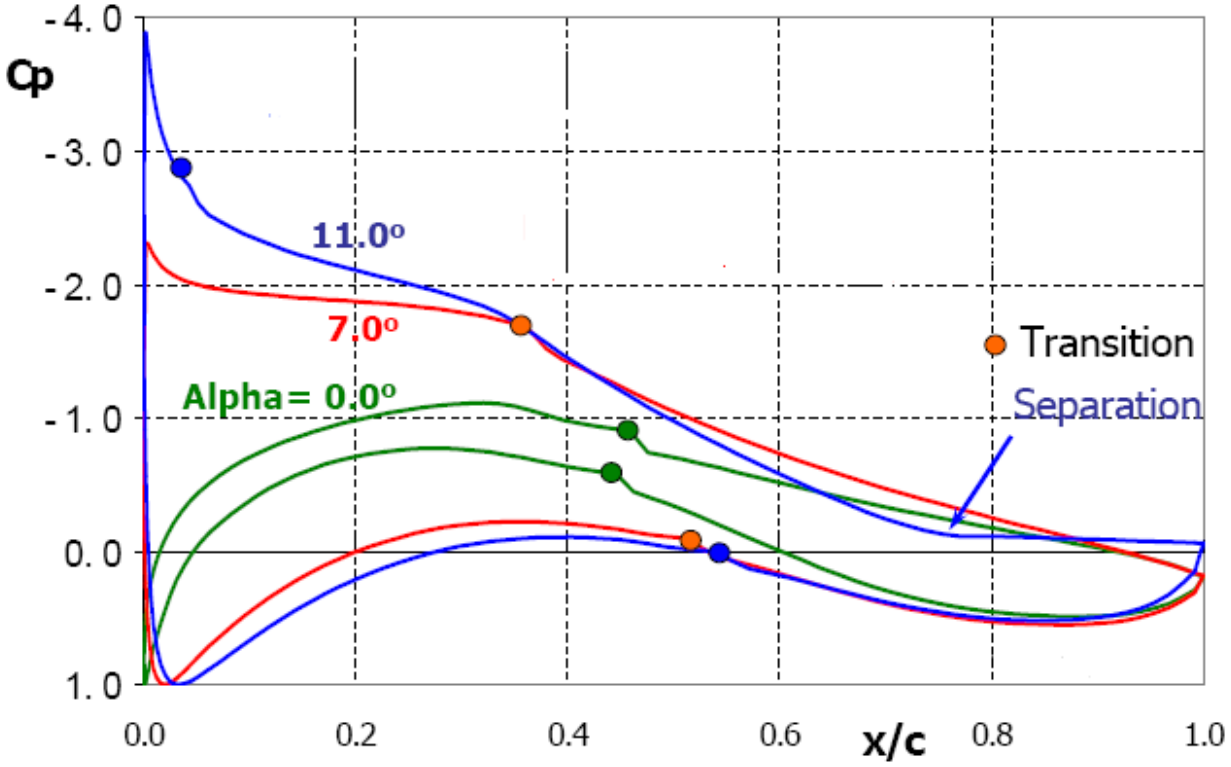

Figure 1.7 – Selected pressure distributions from experiment – Du91-W2-250 – Re = 500,00

Appendix 2

NACA 64-418 – Experimental airfoil characteristics

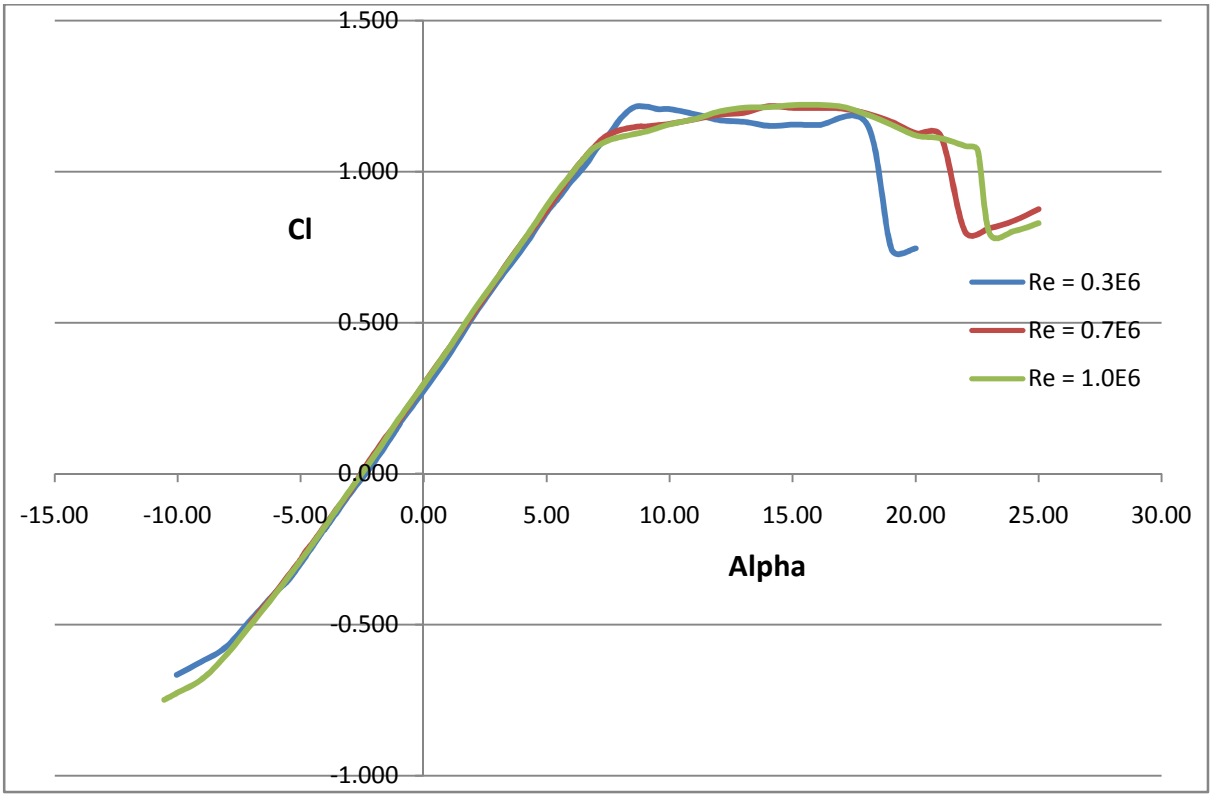

Figure 2.1 - Experimental Cl vs α - NACA 64-418

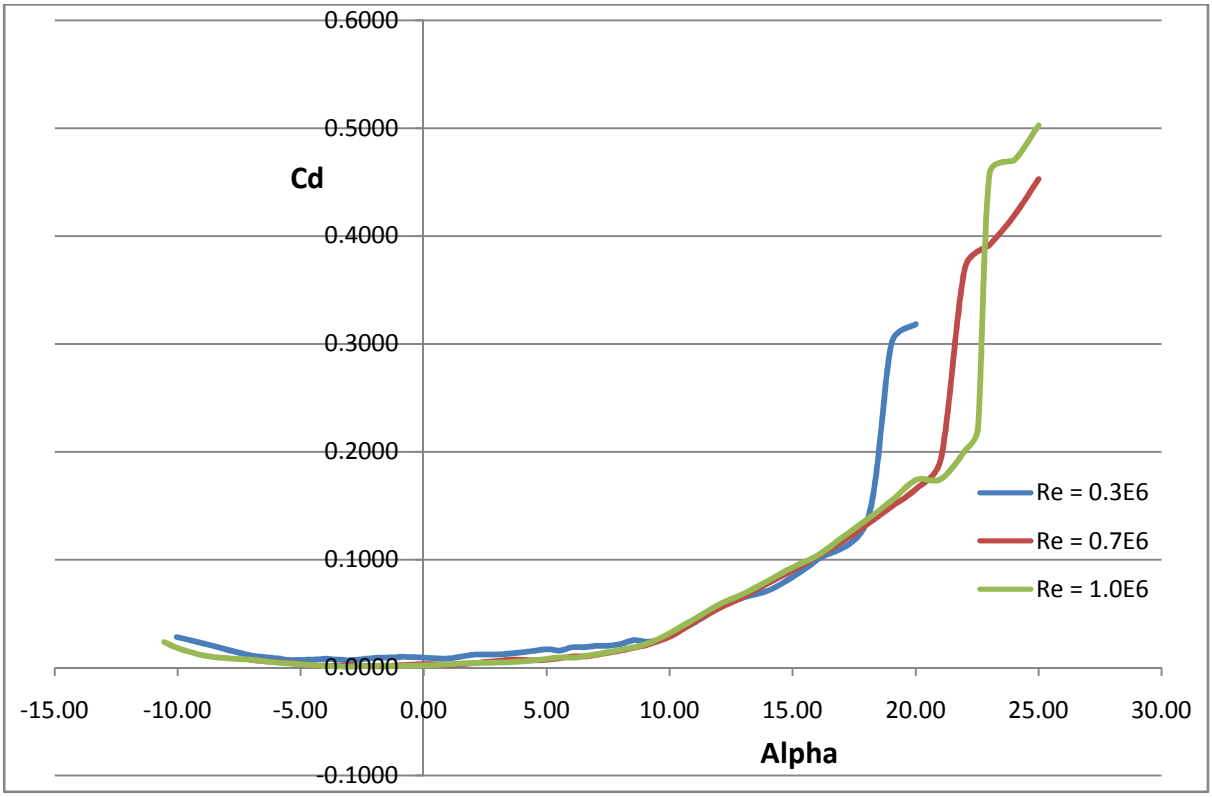

Figure 2.2 - Experimental Cd vs α - NACA 64-418

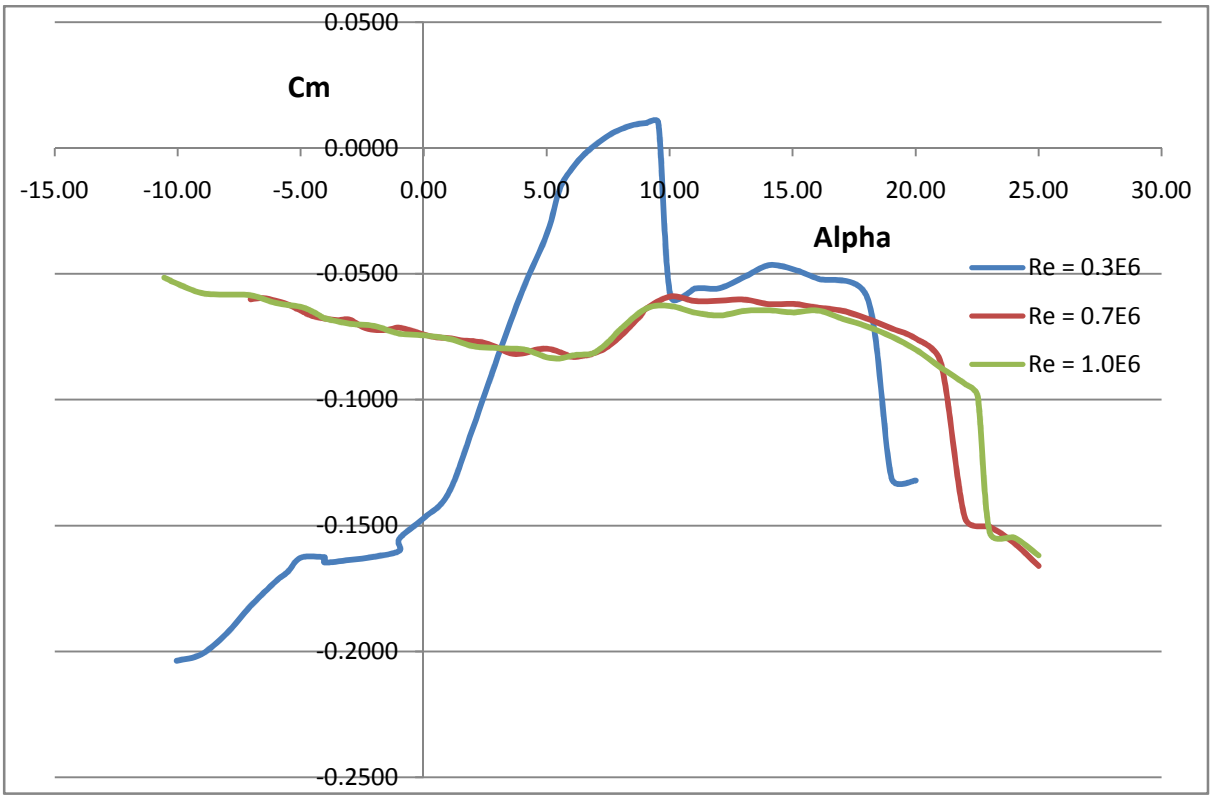

Figure .3 - Experimental Cm vs α - NACA 64-418

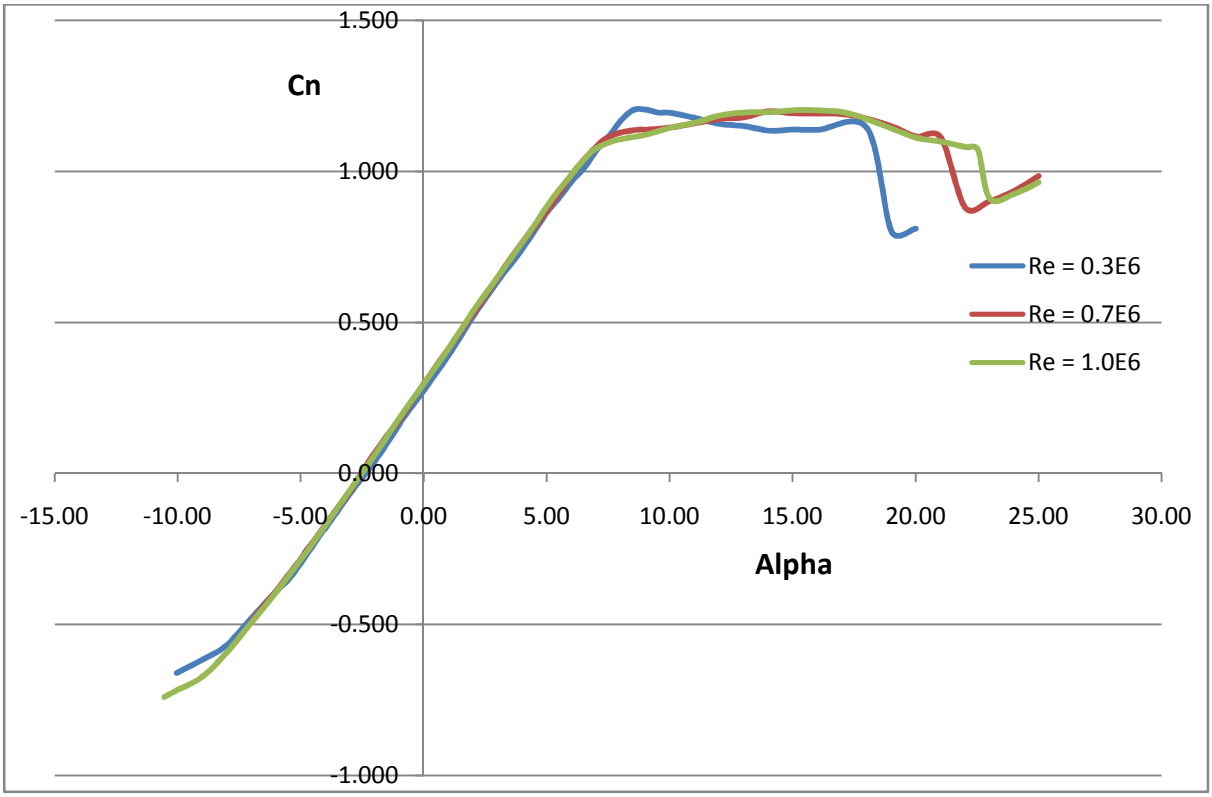

Figure 2.4 - Experimental Cd vs α - NACA 64-418

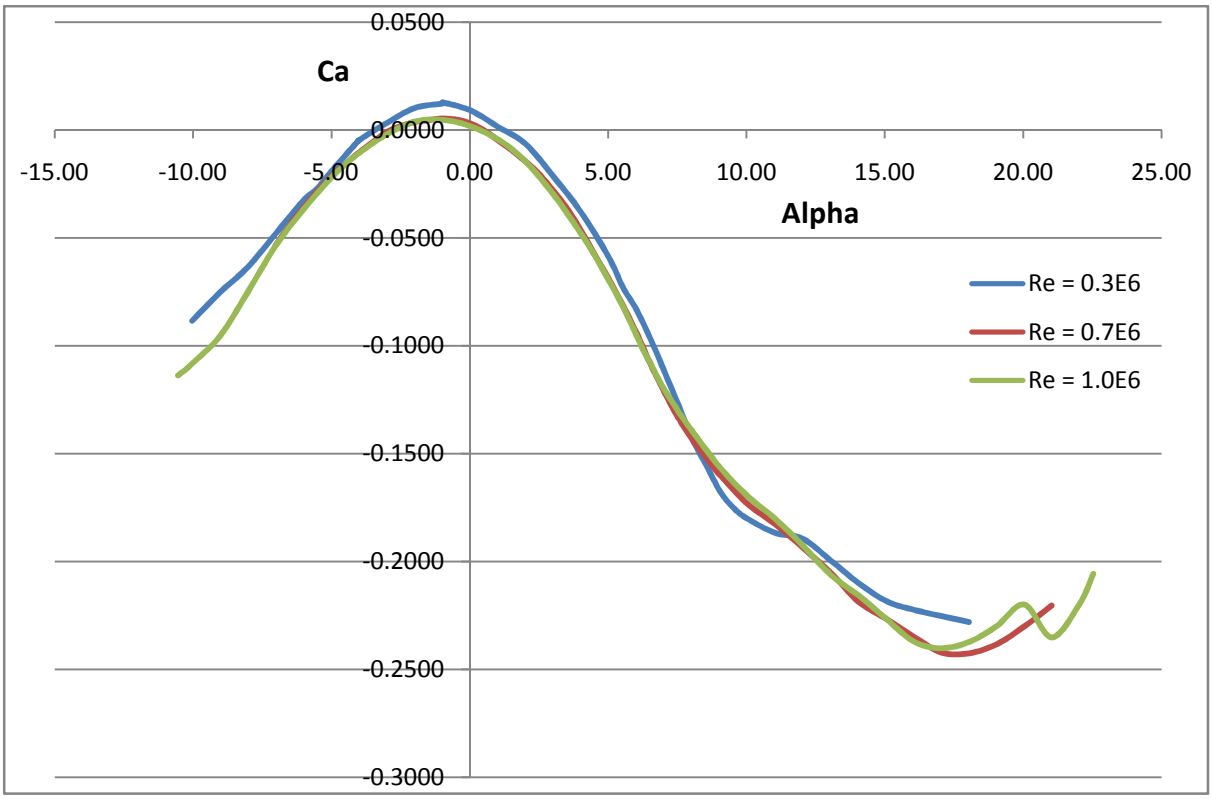

Figure 2.5 - Experimental Ct vs α - NACA 64-418

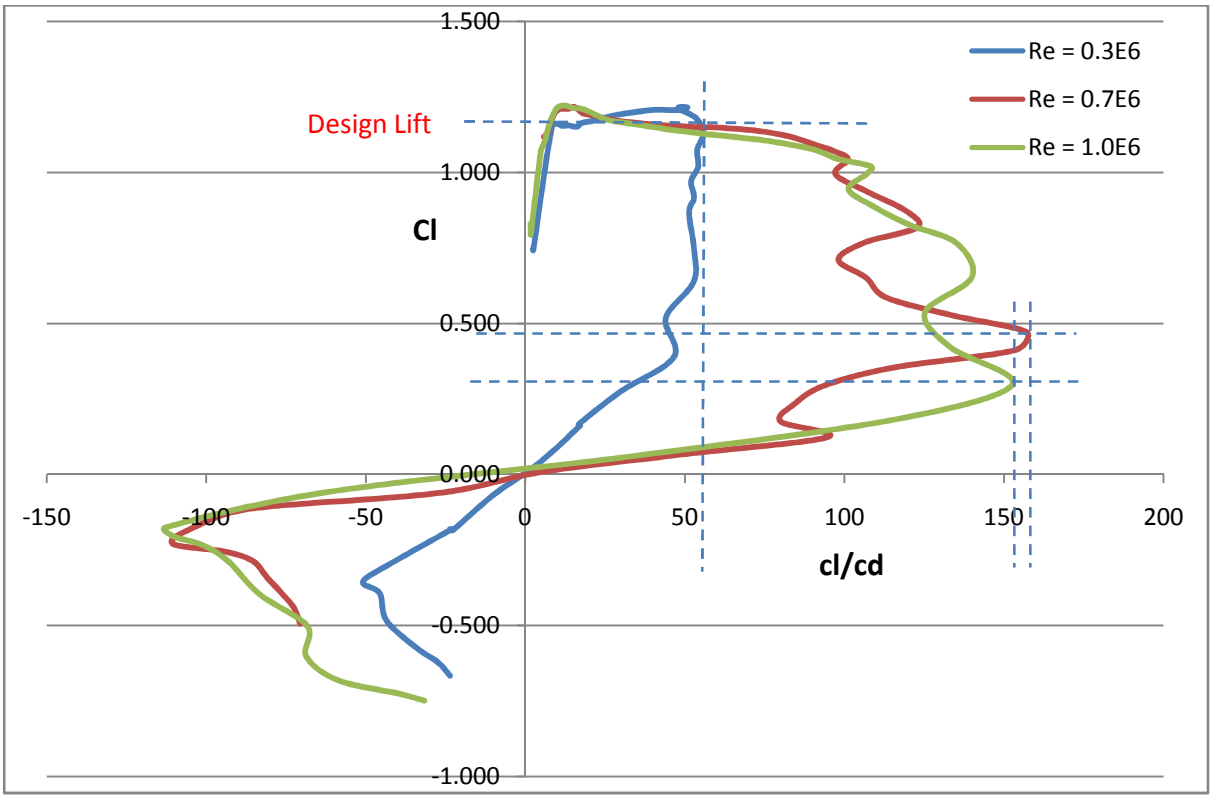

Figure 2.6 - Experimental Cl vs Cl/Cd - NACA 64-418

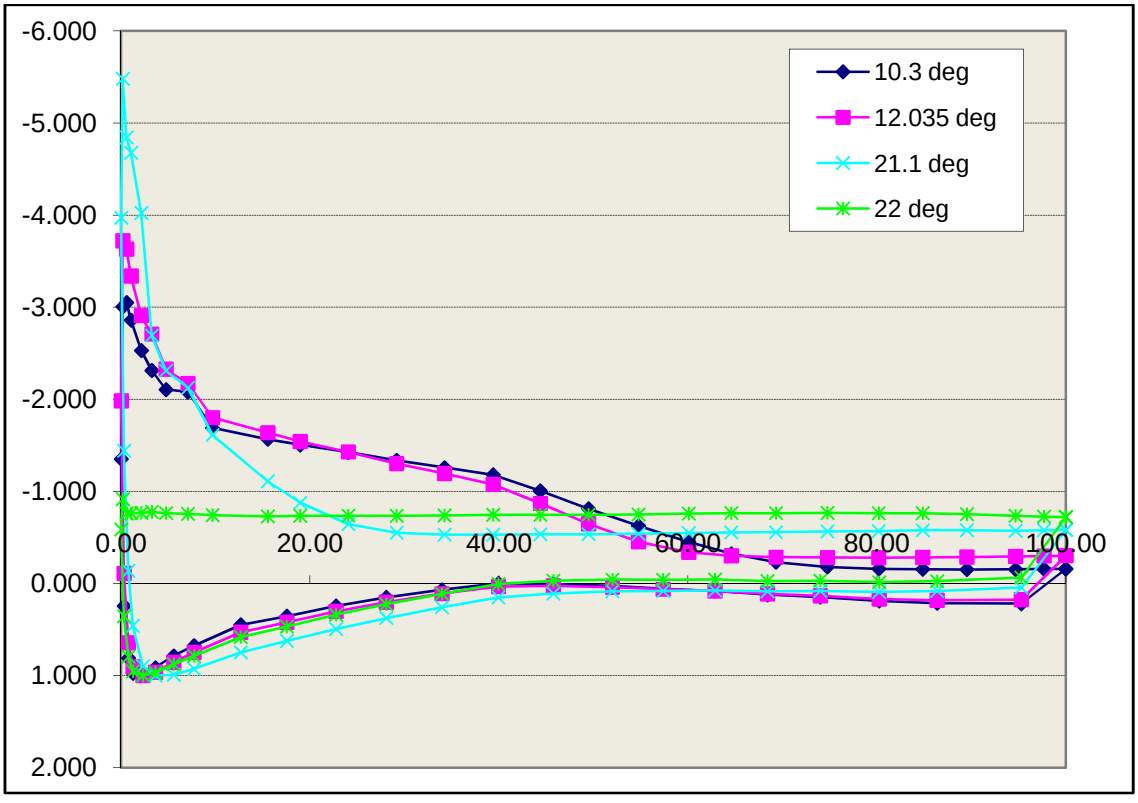

Figure 2.7 – Selected pressure distributions – NACA 64-418 – Re = 1,000,000

Appendix 3

```
%% Matlab code to generate script files over AoA range (18/08/10)

clear all;
clc;

%% Creates script file and begins loop over AoA range
outname = ['script.txt']; % Outputs Script with filename script.txt
fid_out = fopen(outname,'wt');
for alfa = -14:2:30; % User input for AoA range


%% Reads in sript lines not affected by alpha
fid_in_top = fopen('top.txt');
fid_in_mid = fopen('middle.txt');

    outdir = ['output_' num2str(alfa)]; % creates a directory for the
outputted files at each alpha
    system(['mkdir ' outdir]);

%% User inputs for wind vector magnitude
Re = 1e6;
Mu = 1.7895e-5;
Rho = 1.225;
C= 1.;
Uinf = Re*Mu/(Rho*C);


%% calculates x and y components of wind vector at each alpha
uinf = Uinf*cosd(alfa);
vinf = Uinf*sind(alfa);

%% Calculates the boundary conditions for alpha. Reports and outputs the
airfoil characteristics at each alpha
fprintf(fid_out,'%s\n%s\n%s\n%s\n','file/start-transcript',[outdir
'transcript(' num2str(alfa) ').txt']);

while 1
    tline = fgetl(fid_in_top);
    if ~ischar(tline),   break,   end
    disp(tline);
    fprintf(fid_out,'%s\n',tline);
end
fclose(fid_in_top);

fprintf(fid_out,'%s\n%s\n%s\n',num2str(uinf), 'no', num2str(vinf)); %
determines the velocity inlet conditions at each alpha
while 1
    tline = fgetl(fid_in_mid);
    if ~ischar(tline),   break,   end
    disp(tline);
    fprintf(fid_out,'%s\n',tline);
end
fclose(fid_in_mid);
```

```
fprintf(fid_out,'%s\n%s\n%s\n%s\n%s\n%s\n%s\n%s\n%s\n',
'report/forces/wall-
forces','yes','1','0','yes',[outdir 'xforces(' num2str(alfa) ').frp']);

fprintf(fid_out,'%s\n%s\n%s\n%s\n%s\n%s\n%s\n%s\n%s\n',
'report/forces/wall-
forces','yes','0','1','yes',[outdir 'yforces(' num2str(alfa) ').frp']);

fprintf(fid_out,'%s\n%s\n%s\n%s\n%s\n%s\n%s\n%s\n%s\n',
'report/forces/wall-
moments','yes','-0.25','0','yes',[outdir 'moments(' num2str(alfa)
').frp']);
fprintf(fid_out,'%s\n%s\n%s\n%s\n%s\n%s\n%s\n%s\n%s\n%s\n%s\n%s\n%s\n%s\n%s
\n','plot/plot','yes',[outdir 'Cpx(' num2str(alfa)
').txt'],'no','no','no','pressure-coefficient','yes','1','0','1','()');
fprintf(fid_out,'%s\n%s\n%s\n%s\n%s\n%s\n',['wcd "alpha(' num2str(alfa)
').cas"'],'yes','file/stop-transcript');

end
fprintf(fid_out,'%s\n','exit');
fclose all;
```

Appendix 4

Du91-W2-250 Calculated Airfoil Characteristics – Re = 500,000

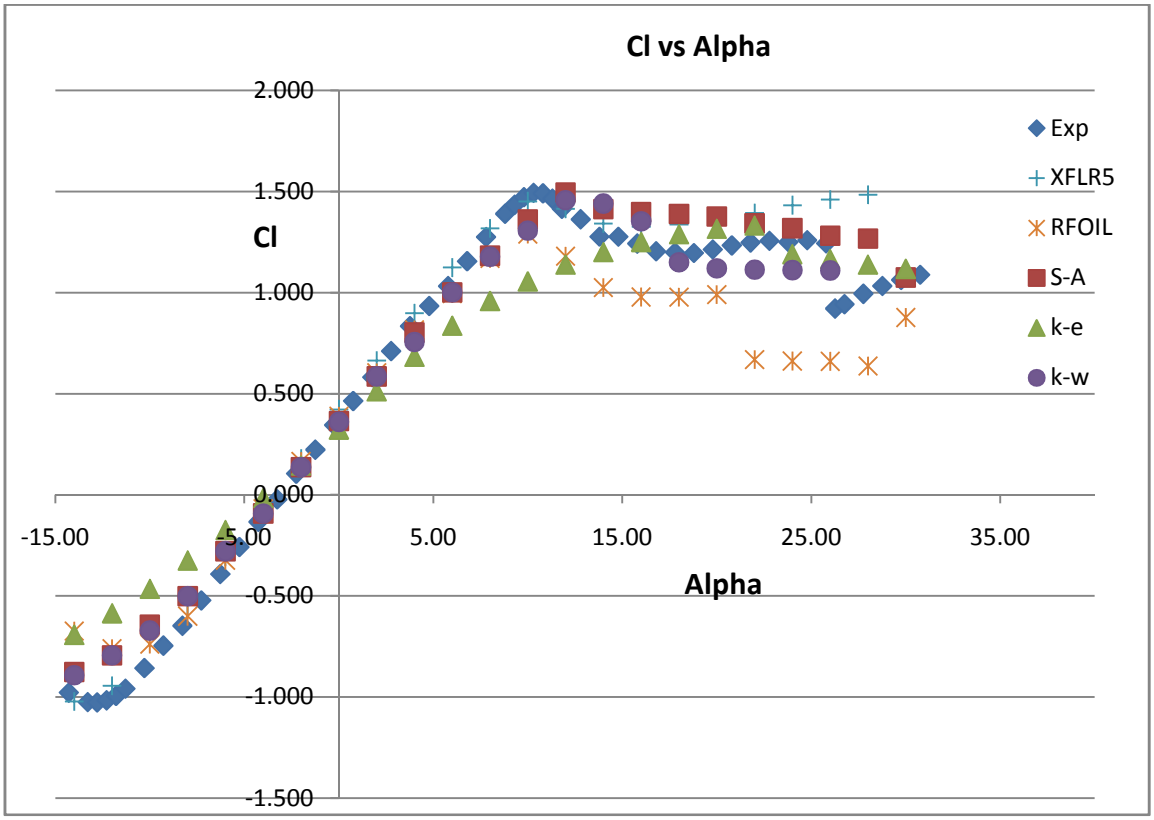

Figure 4.1 – Computed Cl vs α - Du91-W2-250 – Re = 500,000

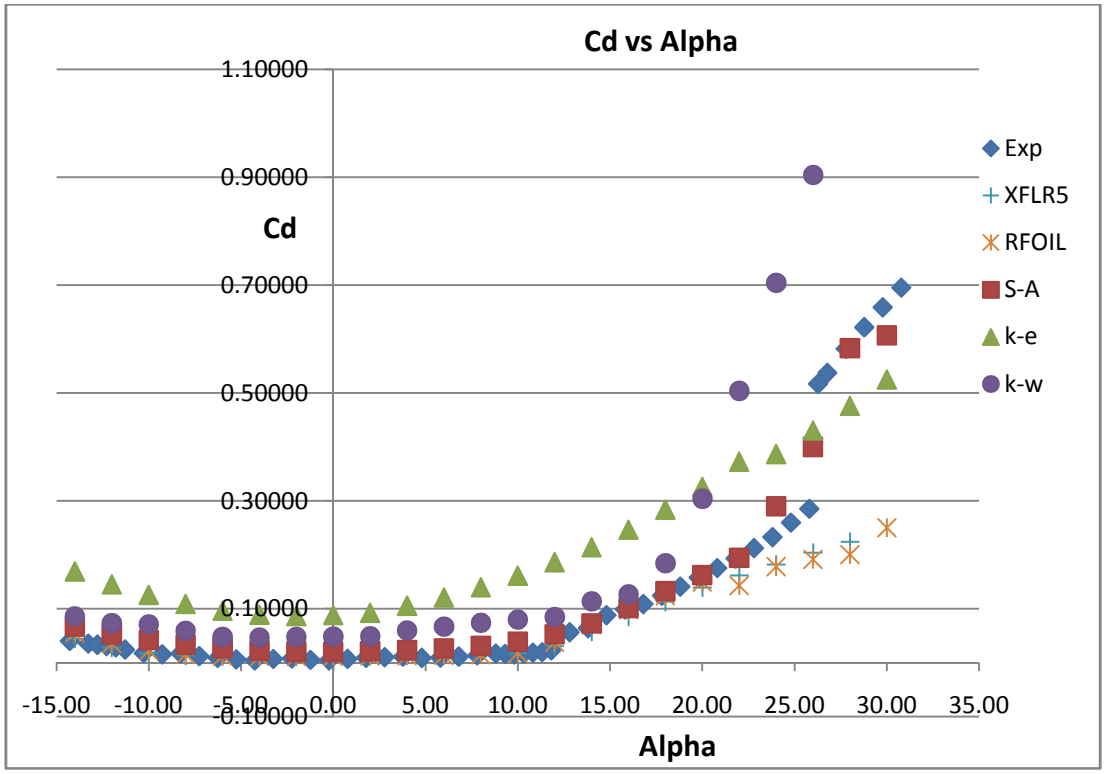

Figure 4.2 - Computed Cd vs α - Du91-W2-250 – Re = 500,000

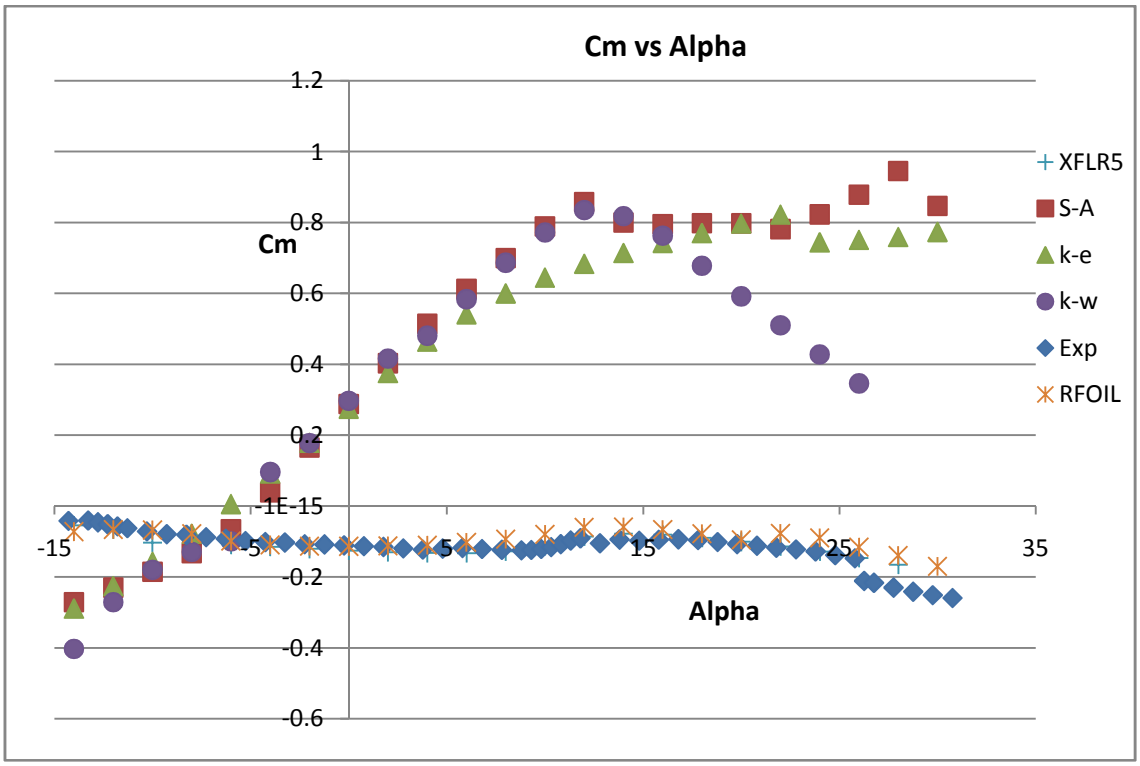

Figure 4.3 - Computed Cm vs α - Du91-W2-250 – Re = 500,000

Du91-W2-250 Calculated Airfoil Characteristics – Re = 1,000,000

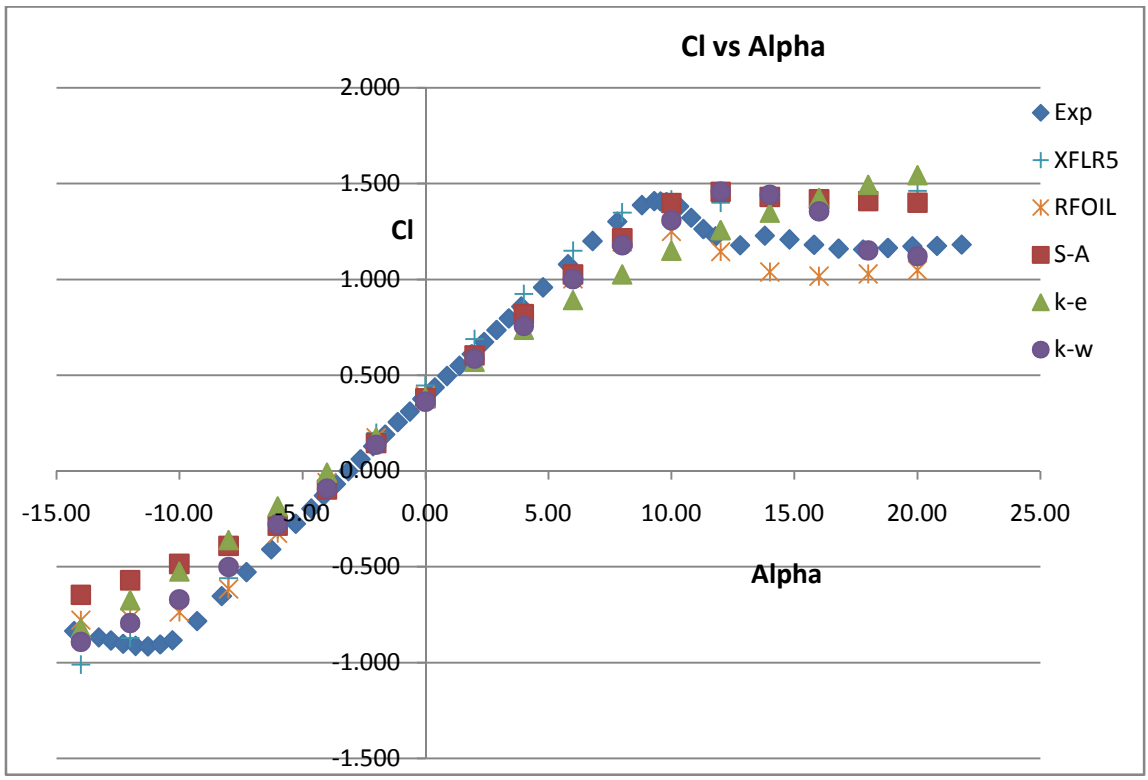

Figure 4.4 - Computed Cl vs α - Du91-W2-250 – Re = 1,000,000

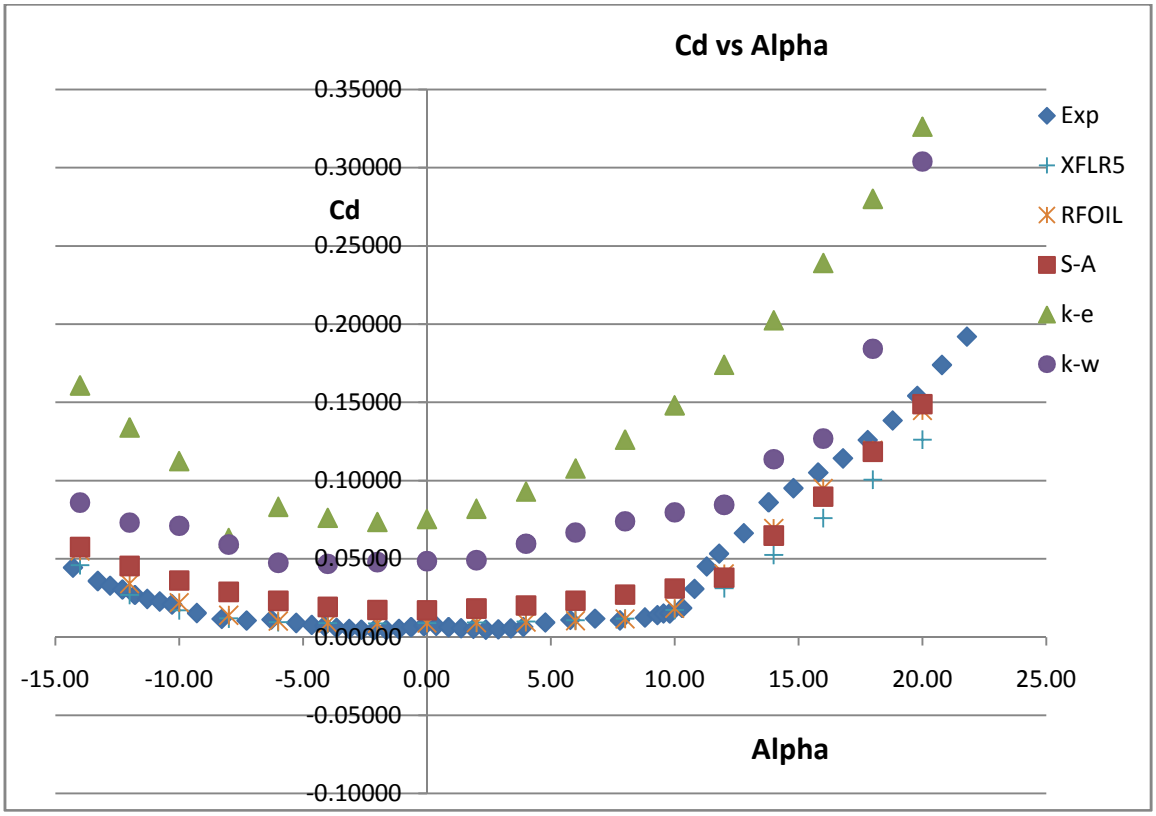

Figure 4.5 - Computed Cd vs α - Du91-W2-250 – Re = 1,000,000

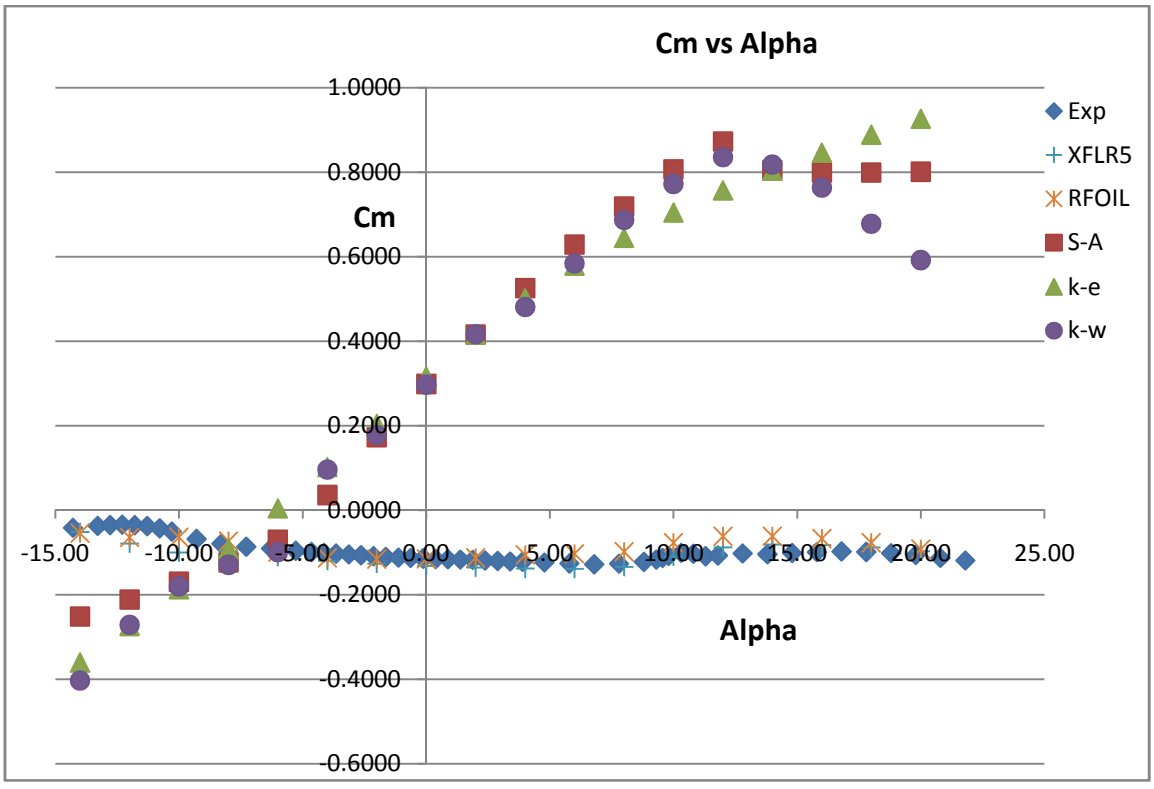

Figure 4.6 - Computed Cm vs α - Du91-W2-250 – Re = 1,000,000

NACA 64-418 Calculated Airfoil Characteristics – Re = 300,000

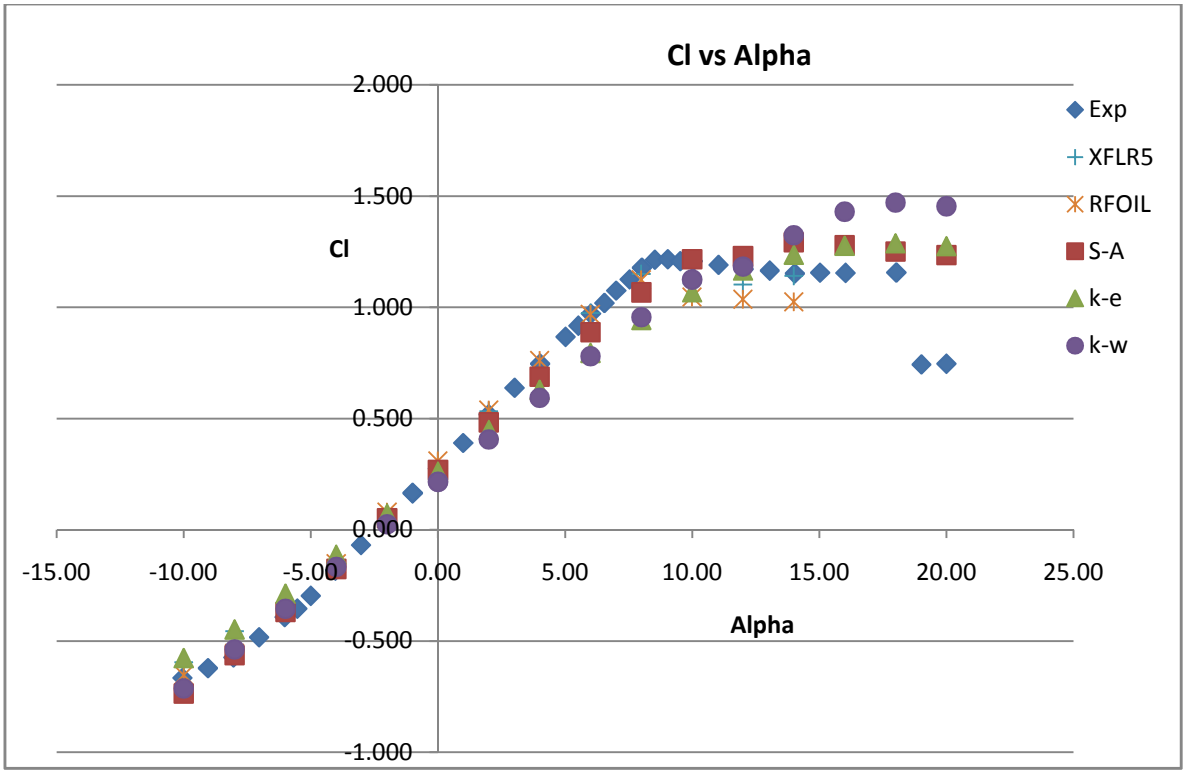

Figure 4.7 - Computed Cl vs α – NACA 64-418 – Re = 300,000

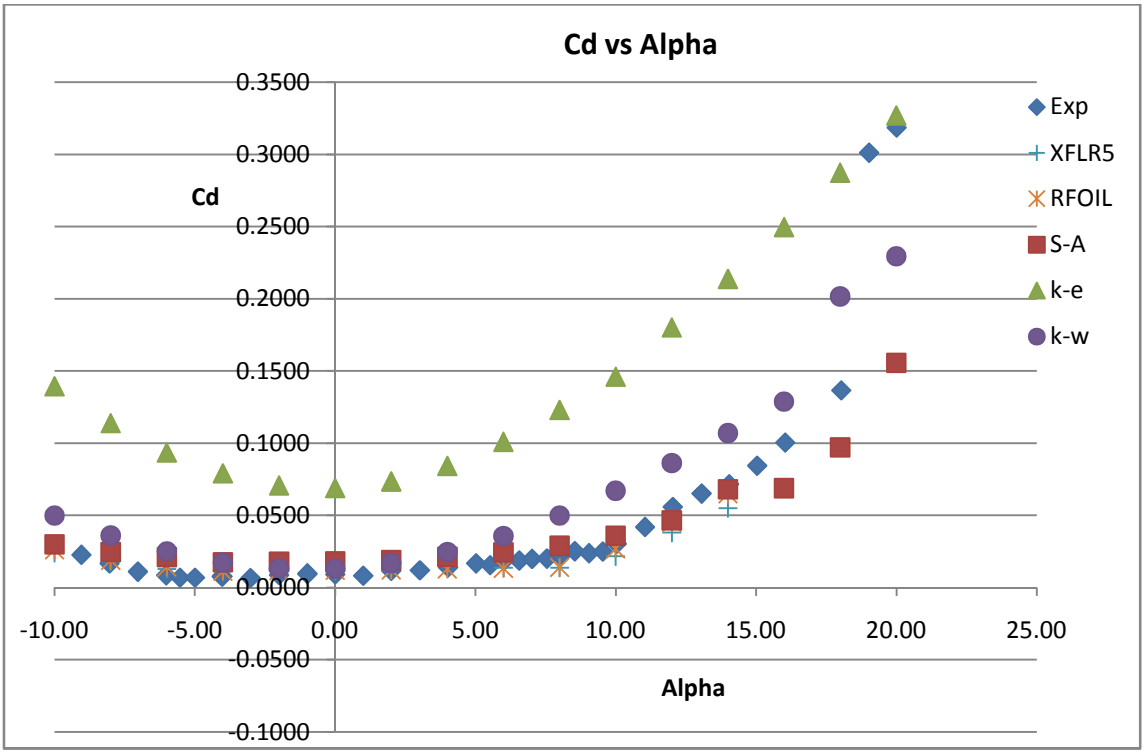

Figure 4.8 - Computed Cd vs α – NACA 64-418 – Re = 300,000

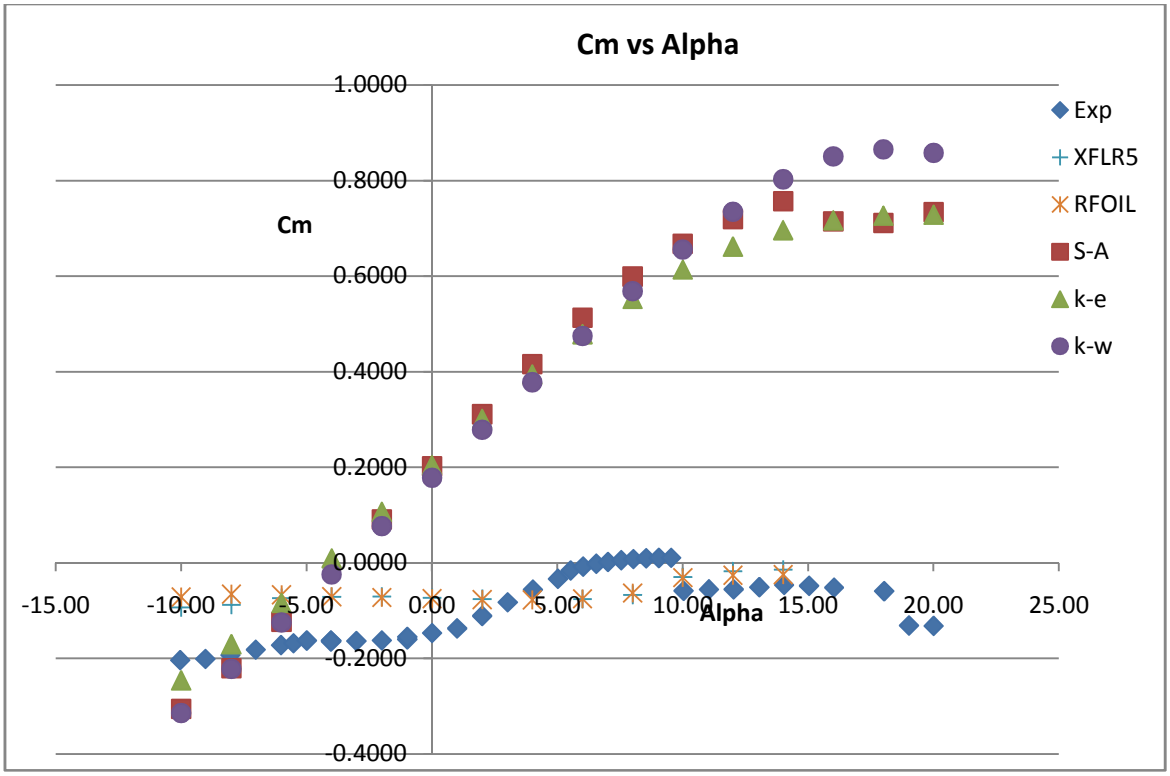

Figure 4.9 - Computed Cm vs α – NACA 64-418 – Re = 300,000

NACA 64-418 Calculated Airfoil Characteristics – Re = 1,000,000

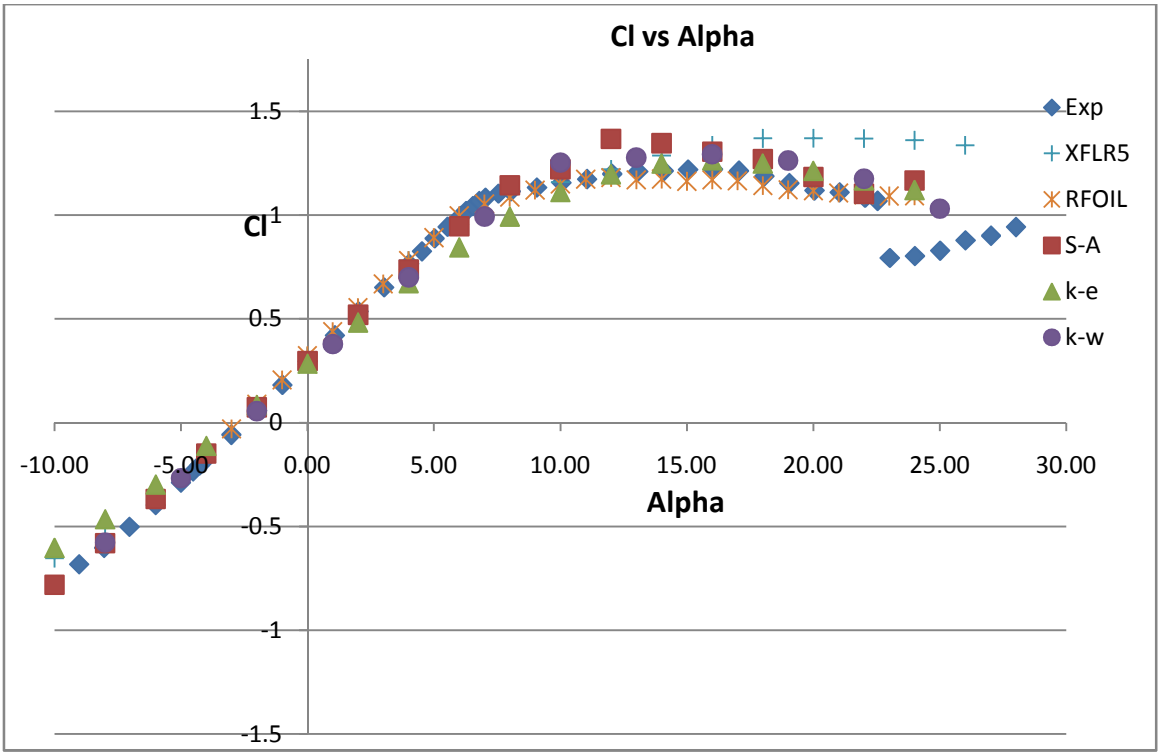

Figure 4.10 - Computed Cl vs α – NACA 64-418 – Re = 1,000,000

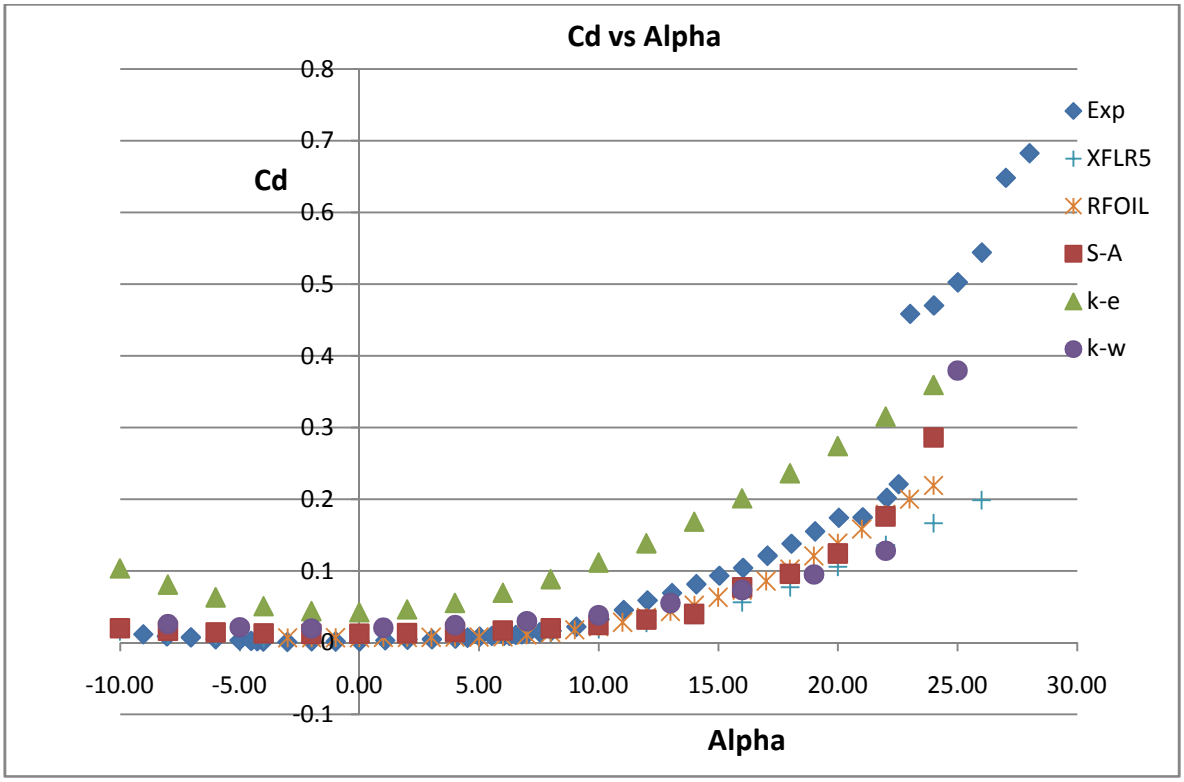

Figure 4.11 - Computed Cd vs α – NACA 64-418 – Re = 1,000,000

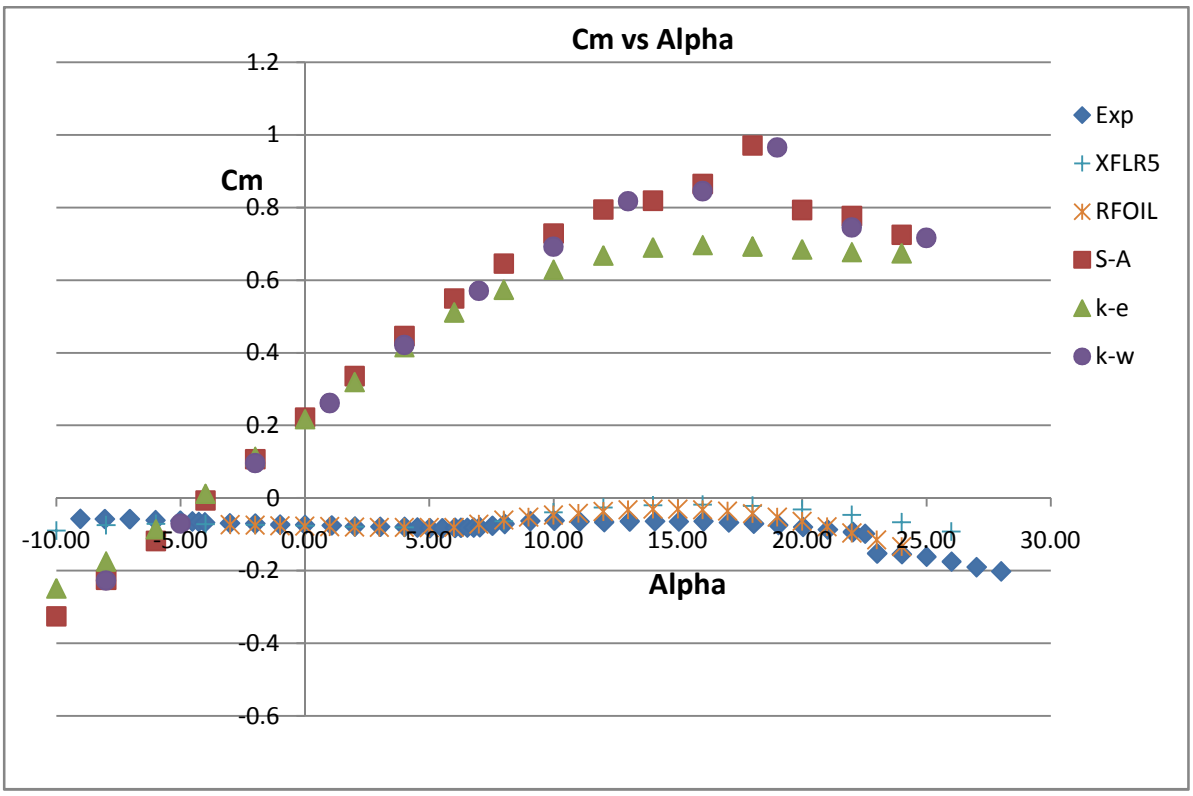

Figure 4.12 - Computed Cm vs α – NACA 64-418 – Re = 1,000,000

References

[1] Manwell, J.F., Rogers, A.L, McGowan, J.G., 2009. *Wind Energy Explained*: *Theory, Design and Application*. Second Edition. Amherst. Wiley

[2] UNFCC, 2007. *Kyoto Protocol*. [online] Available at: <http://unfccc.int/kyoto_protocol/items/2830.php> [Accessed 14 July 2010]

[3] The Parliamentary Office of Science and Technology, 2004. *The Future of UK Gas Supplies*. [online] Available at: http://www.parliament.uk/documents/post/postpn230.pdf> [Accessed 31 July 2010]

[4] Leishman, J.G., 2006. *Principals of Helicopter Aerodynamics.* Second Edition. New York. Cambridge University Press

[5] Sant, T., 2007. Improving *BEM based Aerodynamic Models in Wind Turbine Design Codes*. Delft. Delft University of Technology

[6] Renewable Energy UK, 2006. *Vertical Axis Wind Turbines*. [online] Available at: < http://www.reuk.co.uk/VAWT-Vertical-Axis-Wind-Turbine.htm> [Accessed 28 July 2010]

[7] BWEA, 2010. *Onshore Wind*. [online] Available at: < http://www.bwea.com/onshore/index.html> [Accessed 02 August 2010]

[8] Anderson, J.D., 2007. *Fundamentals of Aerodynamics*. Fourth Edition. Singapore. McGraw Hill

[9] Kay, A.W., 2008. *Investigating the Unsteady Aerodynamics Associated with a HAWT with Reference to the Recent Experimental Data gathered during the Mexico Project*. Delft. Delft University of Technology.

[10] Robinson, M. C., Simms, D., Hand, M. M., Schreck, S.J., 1999. *Horizontal Axis Wind Turbine Aerodynamics: Three Dimensional, Unsteady, and Separated Flow Influences*.

[11] NREL, 1995. *NREL Airfoil Families for HAWT*. [online] Available at < http://wind.nrel.gov/designcodes/papers/NREL%20Airfoil%20Families%20for%20HAWTs.pdf> [Accessed 02 August 2010]

[12] NREL, 1976. *Aerodynamic Performance of Wind Turbines*. [online] Available at: < http://wind.nrel.gov/designcodes/papers/WilsonLissamanWalker_AerodynamicPerformanceOfWindTurbines(1976).pdf> [Accessed 03 August 2010]

[13] Bak, C., Fugslang, P., Sorensen, C.C., Madsen, H.A., 1999. *Airfoil Characteristics for Wind Turbines.* Roskilde. RISO National Laboratory.

[14] Ingram, G., 2005. *Wind Turbine Blade Analysis Using the Blade Element Momentum Method*. University of Durham. [online] Available at: http://www.dur.ac.uk/g.l.ingram/download/wind_turbine_design.pdf [Accessed 10 August 2010]

[15] Hau, E., 2006. *Wind Turbines: Fundamentals, Technologies, Application, Economics*. Second Edition. Krailling. Springer.

[16] Sheng, W., Galbraith, R. A. McD., Cotton, F. N., 2007. *A Modified Dynamic Stall Model for Low Mach Numbers*. Journal of Solar Energy. [Accessed 11 August 2010]

[17] Walter, P.W., Stuart, S.O., 1997. *CFD Calculations of S809 Airfoil Characteristics*. [online] Available at: http://windpower.sandia.gov/asme/AIAA-97-0973.pdf [Accessed 11 August 2010]

[18] Goswami, Y.D., Kreith, F., 2007. *Energy Conversion*.

[19] Watson, B., 2002. *XFOIL*. California Polytechnic State University. [online] Available at: http://www.scribd.com/doc/22992573/XFOIL [Accessed 13 August 2010]

[20] Timmer, N. Ruud, V.R, 2004. *Design of Airfoils for Wind Turbine Blades*. Delft University of Technology. [online] Available at: http://gcep.stanford.edu/pdfs/energy_workshops_04_04/wind_van_rooij.pdf [Accessed 02 August 2010]

[21] Seto, L. Y., Galbraith, R. A. McD., 1985, *The Effect of Pitch Rate on the Dynamic Stall of a NACA 23012 Airfoil*. 11th European Rotorcraft Forum. London

[22] Hansen, A.C., Butterfield, C.P, 1993. *Aerodynamics of Horizontal Axis Wind Turbines*. Annual Review of Fluid Mechanics. Vol. 25

[23] Anderson, J.D., 2009. *Computational Fluid Dynamics: An Introduction*. Fourth Edition. Berlin. Springer

[24] Carcangiu, C.E., 2008. *CFD-RANS Study of Horizontal Axis Wind Turbines*. [online] Available at: http://veprints.unica.it/84/1/carcangiu_carlo_enrico.pdf [Accessed 18 August 2010]

[25] Sibly School of Mechanical and Aerospace Engineering. *FLUENT Tutorials – Flow Over an Airfoil Step 2 – Meshing the Geometry*. Cornel University. [online] Available at: http://courses.cit.cornell.edu/fluent/index.htm [Accessed 20 August 2010]

[26] Symscape, 2009. *Reynolds-Averaged Navier-Stokes Equations.* [online] Available at: http://www.symscape.com/reynolds-averaged-navier-stokes-equations [Accessed 19 August 2010]

[27] CFD online, 2007. *Structured mesh generation*. [online] Available at: http://www.cfd-online.com/Wiki/Structured_mesh_generation [Accessed 20 August 2010]

[28] Ansys FLUENT, 2006. *FLUENT 6.3 Users Guide*. [online] Available at: http://my.fit.edu/itresources/manuals/fluent6.3/help/html/ug/node986.htm [Accessed 20 August 2010]

[29] Drela, M., 2000. *XFOIL-Subsonic Airfoil Development System*. MIT. [online] Available at: http://web.mit.edu/drela/Public/web/xfoil/ [Accessed 01 June 2010]

[30] Drela, M., 1987. *XFOIL-Subsonic Airfoil Development System*. MIT. [online] Available at: http://web.mit.edu/drela/Public/web/xfoil/ [Accessed 01 June 2010]

[31] Symscape, 2007. *Why Use a Panel Method?* [online] Available at: http://www.symscape.com/blog/why_use_panel_method [Accessed 22 August 2010]

[32] Rooij V.R.P.J.O.M., 1996. *Modification of the Boundary Layer Formulation in RFOIL for Improved Airfoil Stall Prediction.* Delft. Delft University of Technology

[33] Sibly School of Mechanical and Aerospace Engineering. *FLUENT Tutorials – Flow Over an Airfoil*. Cornel University. [online] Available at: http://courses.cit.cornell.edu/fluent/index.htm [Accessed 02 June 2010]

[34] Innovative CFD, 2007. *Making Sense of CFD Grid Types.* [online] Available at: http://www.innovative-cfd.com/cfd-grid.html [Accessed 15 August 2010]

[35] Hinze, J.O, 1975. *Turbulence*. New York. McGraw Hill

[36] Teodorovich, E.V, 2008. *Calculation of Turbulent Viscosity*. Fluid Mechanics. Volume 22, Number 4.

[37] Garrad Hassan, 2010. *The CFD Approach*. [online] Available at: http://www.garradhassan.com/services/eds/cfdapproach.php [Accessed 31 July 2010]

[38] Salim, M., Cheah, S.C., 2009. *Wall y+ Strategy for Dealing with Wall-bounded Turbulent Flows.* Conference of Engineers and Computer Scientists 2009. Vol 2.

[39] Engineering-Tips, 2010. *CFD y+*. [online] Available at: http://www.eng-tips.com/viewthread.cfm?qid=248146&page=1 [Accessed 15 August 2010]

[40] Chilka, A., Kulkarni, A., 2006. *Modelling Turbulent Flows in Fluent*. [online] Available at: http://www.fluent.com/software/university/blog/turbulent.pdf [Accessed 01 August 2010]

[41] Campobasso, M.S., Zanon, A., Foerster, F., Fraysse. F., Bonfiglioli, A., 2009. *CFD Modelling of Wind Turbine Airfoil Aerodynamics*. Glasgow. University of Glasgow

[42] Simms, D., Schreck, S., Hand, M., Fingersh L.J., 2001. *NREL Unsteady Aerodynamics Experiment in the NASA – Ames Wind Tunnel: A Comparison of Predictions to Measurement.* Colorado. NREL

[43] GWEC, 2009. *Global Wind Report 2009*. GWEC

[44] WIKKIBOOKS, 2010. *ICEM CFD*. [online] Available at: http://www.google.co.uk/imgres?imgurl=http://upload.wikimedia.org/wikibooks [Accessed 28 August 2010]